國立臺灣大學工學院機械工程學研究所

碩士論文

Institute of Mechanical Engineering

College of Engineering

National Taiwan University

Master's Thesis

應用線掃描結構光重建表面傾斜與三維形貌之研究

Research on Accurate 3D Profile Reconstruction with Surface Orientation Using Line-scan Structured Light

曹原輔

Yuan-Fu Tsao

指導教授: 陳亮嘉 博士

Advisor: Liang-Chia Chen Ph.D.

中華民國 113 年 2 月

February, 2024

doi:10.6342/NTU202400740

國立臺灣大學碩士學位論文
口試委員會審定書
MASTER'S THESIS ACCEPTANCE CERTIFICATE
NATIONAL TAIWAN UNIVERSITY

應用線掃描結構光重建表面傾斜與三維形貌之研究

Research on Accurate 3D Profile Reconstruction with Surface Orientation Using Line-scan Structured Light

本論文係 曹原輔 (姓名) R10522728 （學號）在國立臺灣大學機械工程學系研究所 (系/所/學位學程)完成之碩士學位論文，於民國 113 年 1 月 30 日承下列考試委員審查通過及口試及格，特此證明。

The undersigned, appointed by the Department / Institute of Mechanical Engineering on 30th (date) 1 (month) 2024 (year) have examined a Master's thesis entitled above presented by Yuan-Fu Tsao (name) R10522728 (student ID) candidate and hereby certify that it is worthy of acceptance.

口試委員 Oral examination committee:

陳宏振 （指導教授 Advisor）

章明　　劉子良　　葉勝利

系主任/所長 Director: _____

誌謝

量測是量化研究的根本，精密是機械工程的核心。有幸在大三升大四的暑假以專題生的身份加入了精密量測實驗室，後來也順利的推甄成為研究生。一路以來，我要感謝老師對我的關照，不論是研究過程中的瓶頸或工程實作上的問題，都是站在公正客觀的角度給予建議。我還要感謝我的父母，謝謝你們的付出與陪伴，並給予我健康的成長環境。科學研究的路程充滿了黑暗與挫折，謝謝家人們給予我的鼓勵，讓我朝向光明前進。最後我要感謝和我同期的研究生們：翰儒、子英、維耘、承鈺、Ankit 和 Mateo，感謝你們豐富了我的碩士生涯，感謝你們讓我知道同儕的重要性，我會懷念一起打籃球的時光的。

doi:10.6342/NTU202400740

摘要

本研究提出了一種適用於線掃描三角架構的測量物體表面傾斜的方法。此方法引用了計算機圖學和投影幾何學的概念，建立表面傾斜角度與其他物理量之間的關係。核心概念是分析相機拍攝到的線條紋之線寬與光強度的變化，再透過設計適當的正向模型來解釋傾斜角和特徵變化之間的關係，進而得知表面傾斜的大小。利用三角函數和微積分的概念即可建立傾斜角度對線寬的影響的模型。傾斜角度對光強響應的模型則是引用蘭柏特餘弦定律來建立。在量測場景中，傾斜角為逆問題的解。反向模型可被重新表述為有約束條件的優化問題，因此傾斜角可以透過尋找目標函數的最小值來獲得。驗證過程分為兩大部分，正向模型與反向模型的驗證。經由驗證結果得知，線寬正向模型與實驗觀測值匹配，R^2 統計量約為 0.644。與三次元量床的量測數據相比，本研究提出的量測方法在關鍵尺寸的量測上仍然有次毫米等級的量測誤差。其誤差來源推測是三維點座標重建演算法的缺陷，以及實際觀測之光條紋與理論假設產生背離所致。

關鍵字：三角法，投影幾何，計算機圖學，相機校正，形貌量測術，表面傾斜

doi:10.6342/NTU202400740

Abstract

In this research, a methodology for measuring surface tilting angle of an object from a triangulation line scanner is proposed. The method implemented concepts from computer graphics and projective geometry. The idea is to detect the changes of linewidth and intensity in the line pattern, the surface tilting angle and the position of the surface can be reconstructed. Appropriate mathematical model explaining the relationship between tilting angles and the features are designed. The rationale behind the concept is also proven theoretically. The model for tilting angle to linewidth can be established using trigonometry and calculus, while the model for tilting angle to intensity is modeled by Lambert's cosine law. In measuring scenario, the tilting angles are the solution to the inverse problem. A reformulation of the inverse problem yields a more convenient way for finding the solution. Finding the tilting angles are thought of as a constrained optimization problem. The validation of the methodology is separated into two parts, one is the validation of forward models and the second is the validation of the inverse problem, i.e. the over-

doi:10.6342/NTU202400740

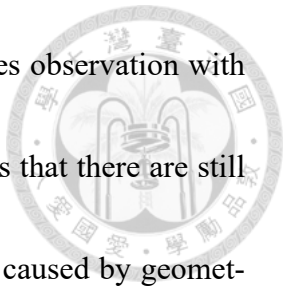

all performance. It is found that the linewidth forward model matches observation with R^2 value around 0.644. The validation of overall methodology shows that there are still rooms for improvements. It is speculated that sub-millimeter bias is caused by geometrical constraint of the measuring system, failure of presumed condition and inappropriate reconstruction algorithm for the 3D coordinates.

Keywords: Triangulation, Projective Geometry, Computer Graphics, Camera Calibration, Profilometry, Surface Orientation

doi:10.6342/NTU202400740

Contents

doi:10.6342/NTU202400740

doi:10.6342/NTU202400740

doi:10.6342/NTU202400740

List of Figures

doi:10.6342/NTU202400740

doi:10.6342/NTU202400740

doi:10.6342/NTU202400740

doi:10.6342/NTU202400740

doi:10.6342/NTU202400740

List of Tables

doi:10.6342/NTU202400740

Nomenclature

Acronyms

CAD Computer Aided Design

CCS Camera coordinate system

CMM Coordinate measuring machine

COP Constrained optimization problem

DoF Degree of freedom

e.g. exempli gratia (Latin for ”for example”)

FWHM Full width at half maximum

i.e. id est (Latin for ”that is”)

LED Light emitting diode

LSF Line spread function

MSE Mean squared error

PSF Point spread function

ROI Region of interest

s.t. such that

w.r.t. with respect to

doi:10.6342/NTU202400740

WCS World coordinate system

Greek symbols

α The Euler angle rotated w.r.t. z-axis

β The Euler angle rotated w.r.t. x'-axis

δ_c Dummy variable in planar equation

γ The Euler angle rotated w.r.t. z''-axis

λ Coefficient of dummy-variable term in planar equation

μ_x Mean of a random variable x in a bivariate normal distribution

μ_y Mean of a random variable y in a bivariate normal distribution

ϕ Zenith angle of the normal vector of a local area

ρ Correlation coefficient of a bivariate normal distribution

σ_x Standard deviation of a random variable x in a bivariate normal distribution

σ_y Standard deviation of a random variable y in a bivariate normal distribution

θ Azimuth angle of the normal vector of a local area

Other symbols

$\intercal$ Transpose operator on matrices

$\mathbf{I}$ Identity matrix

$\mathbf{K}$ Camera intrinsic matrix

$\mathbf{P}_{3\times4}$ Projection matrix

$\mathbf{R}$ Rotational matrix

$\mathcal{N}(\mu, \sigma)$ Normal distribution with mean μ and standard devaition σ

sim Cosine similarity

doi:10.6342/NTU202400740

$\vec{\mathbf{T}}$	Translational vector
a	Coefficient of x_c term in planar equation
b	Coefficient of y_c term in planar equation
c	Coefficient of constant term in planar equation
C_{HM}	Contour at half maximum
$f_1(\cdot)$	Forward model for linewidth
$f_2(\cdot)$	Forward model for intensity
$f_3(\cdot)$	Inverse model for tilting angles
f_x	Focal length on x-axis in camera intrinsic matrix
f_y	Focal length on y-axis in camera intrinsic matrix
I	Representative intensity of a light spot
I_{amp}	Amplitude of the intensity
I_{bg}	Background intensity
L	Linewidth of a light spot
l_x	Translated distance in x_w-direction from o_w to o_c
l_y	Translated distance in y_w-direction from o_w to o_c
l_z	Translated distance in z_w-direction from o_w to o_c
o_c	Origin of CCS
o_w	Origin of WCS
o_x	Offset of image center on x_c-axis in camera intrinsic matrix
o_y	Offset of image center on y_c-axis in camera intrinsic matrix
s	Skew factor in camera intrinsic matrix

doi:10.6342/NTU202400740

t Parameter for constructing an ellipse (de La Hire's ellipse)

$u(t)$ Horizontal coordinate in image coordinate system as a function of t

u Horizontal axis in image coordinate system

v Vertical axis in image coordinate system

x_c x coordinate in CCS

x_w x coordinate in WCS

y_c y coordinate in CCS

y_w y coordinate in WCS

z_c z coordinate in CCS

z_w z coordinate in WCS

doi:10.6342/NTU202400740

Chapter 1 Introduction

1.1 Background

In the manufacturing industry, ensuring product quality is of paramount importance. One critical aspect that determines the quality of a product is its shape and dimensions. To create intricate shapes and components that precisely fit together, mechanical engineers employ a system known as geometric dimensioning and tolerancing (GD&T). GD&T serves as a precise language for specifying the shapes of components and defining allowable deviations in dimensions. This technique finds applications in various areas, from the rotating parts in machine tools to the airfoils on aircraft. Without proper control of the product's geometry, components may not fit together correctly, leading to system malfunctions.

To ensure the product adhere to specification, the manufacturing industry often employs statistical quality control (SQC) or statistical process control (SPC) methodologies. The approaches are instrumental in monitoring and enhancing the production line's yield. However, the effectiveness of these methods depends on the accuracy, reliability, and efficiency of the monitoring system. This is where automatic optical inspection (AOI) becomes crucial in ensuring that the quality control process is thorough and effective.

doi:10.6342/NTU202400740

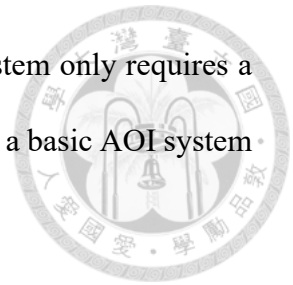

The simplest form of an automatic optical inspection (AOI) system only requires a light source and a camera. There are several advantages to using such a basic AOI system for quality control.

Firstly, it employs optical methods, which means that during the measurement process, the measuring device does not physically touch the product. This reduces the risk of product damage, which is a significant advantage.

Secondly, AOI systems are highly efficient. In these systems, each pixel on the camera sensor can function as a measuring point. This is in contrast to most tactile-measuring systems, which measure objects point by point. AOI systems have the capability to measure multiple points simultaneously, greatly improving efficiency and contributing to increased yield in manufacturing processes. Therefore, implementing an AOI system can significantly enhance the quality of manufactured products.

1.2 Motivation and purpose of this research

Fundamentally, AOI systems consist of two main components: an illuminating subsystem and an imaging subsystem. The imaging subsystem is relatively straightforward, typically involving the use of a camera equipped with either a charge-coupled device (CCD) or complementary metal‐oxide‐semiconductor (CMOS) sensor. However, the illuminating subsystem can vary significantly depending on its intended purpose, and the techniques for extracting valuable information can also differ.

For instance, when measuring the 3D profile of an object, the illuminating subsystem often employs a digital micromirror device (DMD) in conjunction with LED lights as the light source. In some cases, laser projectors are utilized as the light source, with diffractive

doi:10.6342/NTU202400740

optical elements (DOE) serving as devices to generate patterned light. On the other hand, when measuring the surface normal of an object, the illuminating subsystem may require multiple sets of light sources, projecting from various angles to capture the necessary data accurately.

There is currently no established method for simultaneously measuring a 3D profile (3D point cloud) and surface normals within a single system. While it is possible to use post-processing techniques to derive surface normals from the 3D point cloud, the accuracy of these normals is inherently linked to the precision of the acquired points.

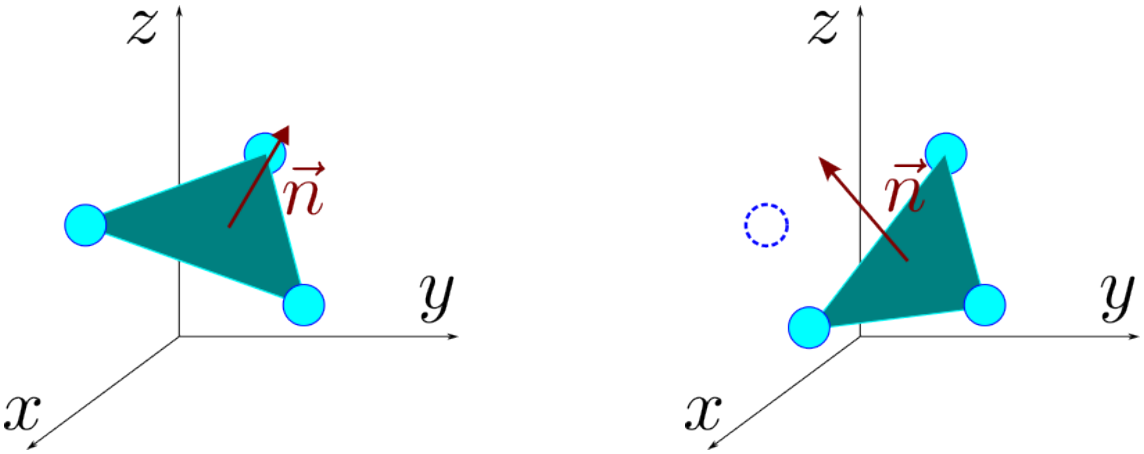

(a) Surface normal reconstructed from neighboring points is marked in red.

(b) One of the points deviated from its original position

Figure 1.1 Changes in the orientation of surface normal when points are deviated.

Furthermore, the relationship between the 3D point cloud and surface normals is inter-dependent. The precision of the measured 3D point cloud can be influenced by factors such as the tilt angle of the object's surface [1–5]. Therefore, it is essential that the measurement of 3D shape and surface normals remain independent of each other. This independence is crucial to prevent the introduction of measurement uncertainty when calculating surface normals from the 3D point cloud.

Indeed, the simultaneous measurement of a 3D profile and surface normals presents

doi:10.6342/NTU202400740

a valuable avenue for research. By combining these data, it is possible to construct a comprehensive 5-dimensional map of an object. This means that following the measurement, not only are the x, y, and z coordinates of each point known, but also the orientation or surface normal at that specific point can be determined without the need for additional post-processing.

This advancement has the potential to greatly benefit various fields and applications, including manufacturing, quality control, robotics, and computer vision. It allows for a more detailed and complete understanding of object geometry, making it a promising area for further exploration and development in the realm of measurement and imaging technologies.

1.3 Problem statement

As previously mentioned, the primary objective of this research is to develop a methodology for accurately measuring the surface normal for each point within a 3D point cloud. The representation of the object's profile involves a 5D array $(x_i, y_i, z_i, \theta_i, \phi_i)$, where each element in this array corresponds to the x-coordinate, y-coordinate, z-coordinate, azimuth angle of the surface normal, and zenith angle of the surface normal for the i-th point in the point cloud.

In essence, the challenge at hand is to establish a mapping that takes into account "a 2D raw image of the measured object, illuminated with an appropriate light source" and "system parameters," and transforms this input into the desired 5D array $(x_i, y_i, z_i, \theta_i, \phi_i)$.

While there have been numerous approaches proposed by various researchers for reconstructing the x, y, and z coordinates from captured images, the methods for simul-

doi:10.6342/NTU202400740

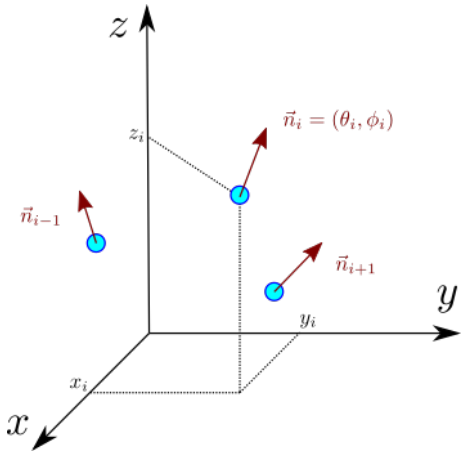

Figure 1.2 Surface normal vector and 3D coordinates are simultaneously obtained without post-processing.

taneously extracting the azimuth and zenith angles (θ and ϕ) from the same raw image have not been as extensively explored. Consequently, this research aims to propose a novel method capable of reconstructing 3D coordinates as well as the tilting angles (surface normals) of the measured object's profile, thereby advancing the field in a previously underexplored direction.

1.4 Structure of this thesis

This thesis comprises 6 chapters and 2 appendices for theoretical rationale, structured as follows:

- Chapter 1 outlines the motivation and problem statement.
- Chapter 2 presents an overview of the literature, discussing commonly used techniques in addressing the problem and highlighting the limitations of conventional methods.
- Chapter 3 provides a concise review of the preliminary knowledge necessary for the development of the proposed model.

doi:10.6342/NTU202400740

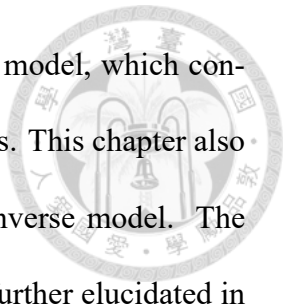

- Chapter 4 offers a comprehensive explanation of the proposed model, which consists of two distinct forward models detailed in separate sections. This chapter also discusses the integration of these models and introduces an inverse model. The theoretical foundation for the model presented in Chapter 4 is further elucidated in appendices A and B.
- Chapter 5 describes the experimental setup and procedure used to validate the significance of the proposed model.
- Chapter 6 concludes with final remarks and a summary of findings.

doi:10.6342/NTU202400740

Chapter 2 Literature Review

2.1 Preface

Surface profilometry techniques can be broadly categorized into two main groups: contact and non-contact methods. Contact methods involve the physical interaction of a stylus with the object's surface, with displacement data recorded as the stylus moves along the surface. Prominent examples include Coordinate Measuring Machines (CMMs). Typical CMM can reach micrometer scale precision. While these methods offer high precision, they also come with drawbacks such as the potential risk of damaging sensitive surfaces and relatively slower measuring efficiency, particularly for complex or large objects.

In contrast, non-contact methods provide significant advantages, including enhanced measuring efficiency and a reduced risk of harm to the object being measured. These tech-

Figure 2.1 A coordinate measuring machine produced by Mitutoyo [6].

doi:10.6342/NTU202400740

niques employ various technologies to capture surface information without direct contact. Non-contact methods encompass a range of approaches such as interferometry, structured light projection, and focus variation. Notably, the effectiveness of these techniques varies with the measurement scale. For instance, interferometry excels at capturing nanometer-scale details, while structured light methods are particularly well-suited for millimeter-scale applications.

In this literature review, we emphasize various non-contact 3D profiling methods that are specifically applied at the millimeter scale. In the subsequent section of the review, we delve into current techniques utilized for the measurement and estimation of surface normals.

2.2 Reconstruction of 3D coordinates

To reconstruct 3D coordinates at the millimeter scale, several common techniques are employed, including structured light, time-of-flight, and stereo vision methods. In this review, we will place a particular emphasis on the structured light method, given its widespread use in commercial 3D scanners. The structured light technique involves projecting a distinct light pattern onto the object's surface to facilitate the reconstruction of 3D information. The concept behind 3D reconstruction can be visualized as follows.

The interaction of the projected light pattern with the object's surface results in pattern variations, with different topographical features yielding unique patterns. These variations allow us to observe and subsequently measure the object's profile.

It's essential to note that actual measurements cannot be obtained until we calculate the 3D coordinates of each point. Consider fringe pattern profilometry as an example: The

doi:10.6342/NTU202400740

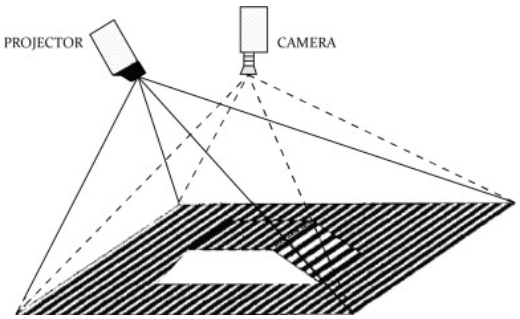

Figure 2.2 Structured light is projected onto the surface. The pattern is distorted by the surface topography [7].

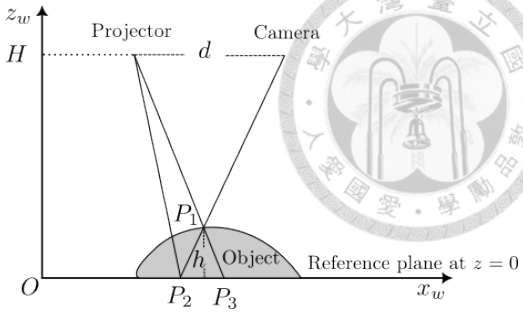

Figure 2.3 The triangulation scheme of a typical structured light projecting system.

extraction of 3D coordinates can be divided into two main steps. The first step involves determining the height value (phase difference relative to the reference) at each point, while the second step entails placing the 3D points into a proper coordinate system.

Multiple approaches exist for height value determination. One such method employs multi-frequency temporal phase unwrapping [8, 9]. This approach projects a series of phase-shifting fringe patterns onto the object, enabling the calculation of the phase value at each camera pixel. Subsequently, by comparing the resulting phase map with the phase map obtained from a reference plane, the height value at each point can be determined using a specific formula [10]

$$h = \frac{H}{1 + \dfrac{2\pi d}{p_0 \Delta P}} \tag{2.1}$$

where h is the object height at point P_1, p_0 is the period of the fringe pattern on reference plane and ΔP is the difference of unwrapped phase between point P_2 and point P_3 (Fig. 2.3).

Another technique for calculating 3D coordinates from distorted fringe patterns is Fourier Transform Profilometry (FTP) [11]. This method requires just one image of the object with a fringe pattern projected onto its surface. Additionally, a recent approach called deep-learning-based phase unwrapping (DLPU) has garnered attention [12–14],

doi:10.6342/NTU202400740

aligning with the increasing trend of artificial intelligence and the widespread application of phase unwrapping techniques, including interferometric measurements and synthetic aperture radar (SAR) [15].

It's crucial to emphasize that these approaches rely heavily on accurate phase-to-height transformations to achieve precise height values at each point [16]. Consequently, the accuracy of the reconstructed 3D coordinates is contingent on the precision of phase value determination. The phase value within each pixel constitutes one of the contributing factors to potential errors in the calculated 3D coordinates.

Laser triangulation offers a straightforward alternative for calculating 3D coordinates from structured light [17, 18]. The simplest form of laser triangulation finds widespread use in laser displacement sensors, which are essential for distance measurement. The fundamental principle behind laser displacement sensors lies in the lateral movement of the laser spot on the camera sensor as the object's height changes.

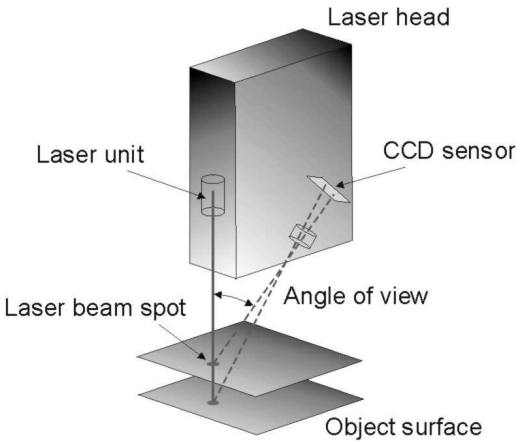

Figure 2.4 Schematic of 1D laser triangulation sensor, i.e. laser displacement sensor [19].

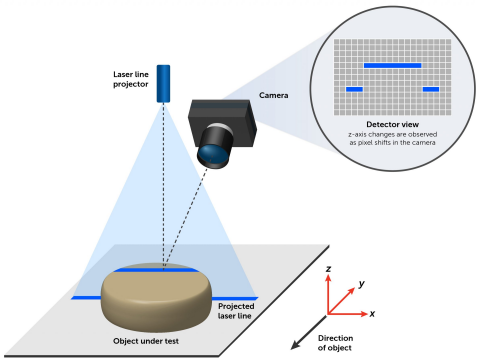

Figure 2.5 Schematic of 2D laser triangulation sensor [20].

The operation of a laser displacement sensor is grounded in the following concept: by calculating the lateral displacement of the laser spot on the sensor, it becomes possible to measure the distance between the object and the sensor. This measurement is carried out

doi:10.6342/NTU202400740

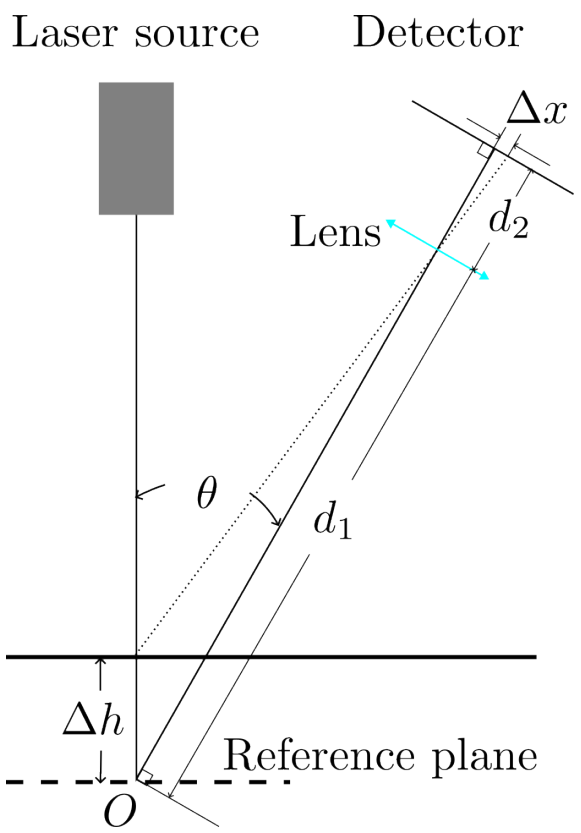

Figure 2.6 Height values are obtained from the position of the light spot on the camera sensor.

using a specific formula [18], with the key requirement being the precise determination of the center position of the laser spot on the camera sensor. The formula used is as follows:

$$\Delta h = \frac{d_1 \Delta x}{\Delta x \cos\theta + d_2 \sin\theta} \tag{2.2}$$

Notably, unlike fringe pattern profilometry, laser triangulation obviates the need for phase value determination. Instead, it directly calculates the positional difference of the laser light pattern relative to the reference. Consequently, the accuracy of the reconstructed 3D coordinate hinges on the precision of determining the center position of the laser spot.

In summary, structured light-based methods offer a potent means of capturing 3D coordinates at the millimeter scale, employing various techniques and approaches to optimize accuracy and efficiency.

doi:10.6342/NTU202400740

2.3 Reconstruction of surface normals

Surface normal reconstruction is often accomplished using a technique known as photometric stereo [21]. In this method, a stationary camera captures an object while light sources project illumination from various directions. By analyzing the shading distribution in multiple images, the surface normal can be calculated. However, a drawback of this approach is its reliance on capturing multiple images, each under distinct lighting conditions. This can significantly reduce efficiency in practical applications, particularly in the context of Automatic Optical Inspection (AOI).

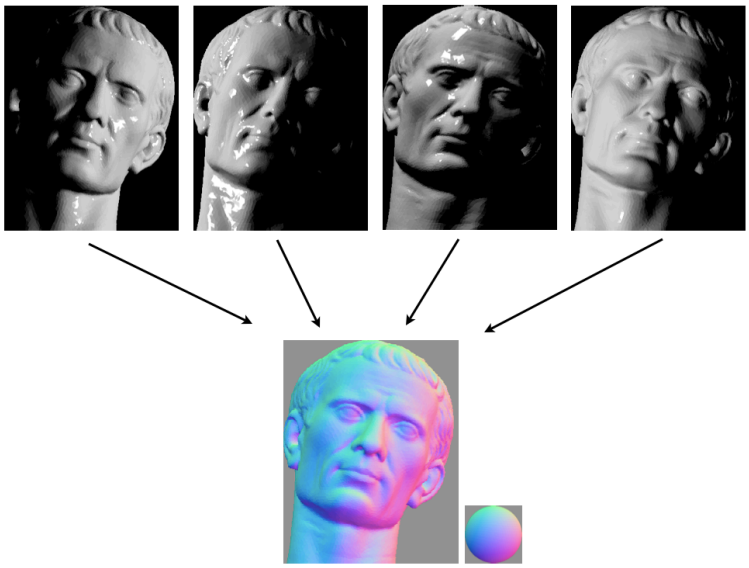

Figure 2.7 Surface normal can be reconstructed by photometric stereo method, but it requires multiple pictures of different shading [22].

An alternative method for surface normal reconstruction involves leveraging deep learning techniques [23–25]. Specifically, this technique employs a convolutional neural network-based surface normal estimator. It operates by analyzing a single image of the scene and predicting the corresponding surface normal map. However, it's important to note that deep learning methods are essentially black box models, meaning that the underlying relationship between image features and surface normals remains unknown.

doi:10.6342/NTU202400740

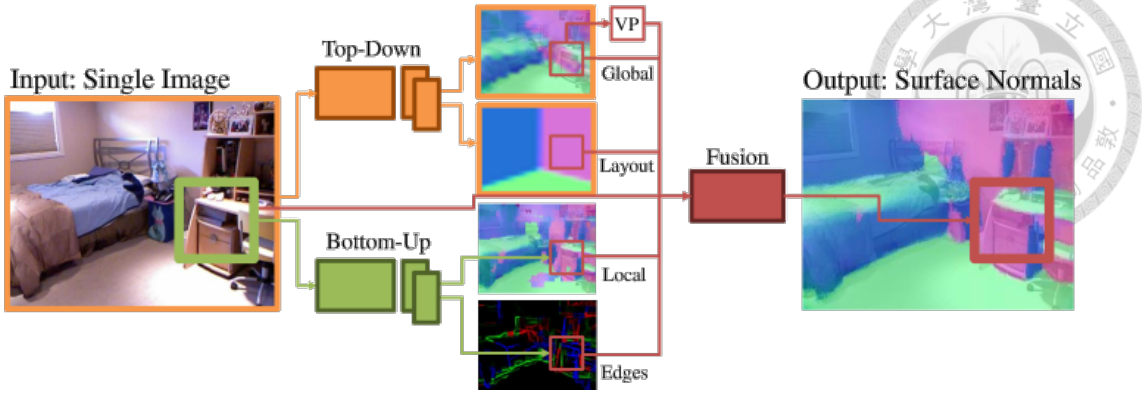

Figure 2.8 An overview of estimating surface normal using deep learning models (VP: vanishing points) [23].

Consequently, the applicability of such models in a generalized context can be somewhat uncertain. The effectiveness of the model relies heavily on the relationship between the testing data and the training data, limiting its performance when applied to objects substantially different from those in the training dataset. Furthermore, the creation of a genuinely useful deep learning model requires a large and representative dataset for the training process.

2.4 Summary

Table 2.1 Summary table of current techniques for 3D coordinate and surface normal reconstruction.

Techniques	Objective	Characteristic feature	Remark
Multi-frequency phase-shifting profilometry	3D coordinate	Phase, intensity of the fringe patterns	-
Fourier transform profilometry	3D coordinate	Frequencies of the fringe patterns	-
Deep learning based profilometry	3D coordinate	Overall fringe pattern	Data-driven method
Laser triangulation	3D coordinate	Position of the light	-
Photometric stereo	surface normal	Distribution of the shadow	-
Deep learning based surface normal estimation	surface normal	Edges and planes in the image	Data-driven method

After a thorough review of existing methods for 3D coordinate reconstruction and

doi:10.6342/NTU202400740

surface normal reconstruction, it becomes evident that there is a notable absence of emphasis on simultaneously reconstructing both aspects using a single integrated system. One of the primary impediments to this integration lies in the fact that surface normal reconstruction typically necessitates light projection from various angles. Such a system setup typically involves multiple light sources, potentially resulting in a larger system compared to those used exclusively for 3D coordinate reconstruction. Moreover, due to hardware disparities, the images used for 3D coordinate reconstruction differ from those employed for surface normal reconstruction. Merging these two functionalities directly into a single system, without altering the reconstruction approach, not only leads to unnecessary system size but also incurs a substantial increase in reconstruction time.

Efficient integration holds the promise of more streamlined measurements. Additionally, it's crucial to recognize that the accuracy of 3D coordinate reconstruction can be influenced by the tilting angle of the object's surface [1–5]. Achieving precise 3D coordinates relies on obtaining accurate surface normals. Consequently, the determination of surface normals is just as pivotal as the determination of 3D coordinates in the overall measurement process.

doi:10.6342/NTU202400740

Chapter 3 Theoretical Background

3.1 Preface

In this research, a single-line pattern laser triangulation scanner is employed due to its simplicity in setup and the availability of well-established 3D reconstruction algorithms. As mentioned in previous chapter, various methods exist for reconstructing 3D coordinates from 2D images, but they generally share a common procedure: applying projective transformation, also known as homography, to map 2D images back to the 3D world coordinate system (WCS). This concept is fundamental not only in this research but also in fields like computer graphics and photogrammetry.

To gain a solid understanding of how 3D reconstruction works and how it can be extended to surface normal reconstruction, it is essential to grasp the fundamentals first. This chapter is divided into three sections to achieve this:

1. The Pin-Hole Model: The first section introduces the prerequisite for projective transformation, which is the pin-hole model. It forms the geometrical basis for mapping the object plane to the image plane.

2. Camera Matrix: The second section explains how the camera matrix can be established based on the pin-hole model. The camera matrix is a key element in the transfor-

doi:10.6342/NTU202400740

mation process and plays a central role in accurate 3D reconstruction.

3. Coordinate Transformation and Rotation in 3D Euclidean Space: To fully grasp how to reconstruct 3D points in the WCS, the third section introduces the concept of the coordinate transformation, which is the underlying concept of extrinsic matrix in camera matrix. Additionally, it briefly delves into the concept of the rotation and Euler angles.

These fundamental concepts laid out in this chapter not only aid in understanding the inner workings of 3D reconstruction but also provide a solid foundation for the development of models discussed in the subsequent chapter. This highlights the generality and significance of these foundational ideas across various applications.

doi:10.6342/NTU202400740

3.2 Pin-hole camera model

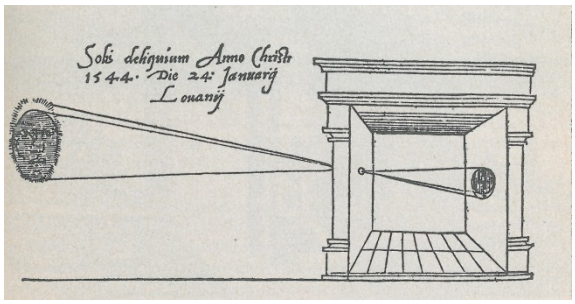

Figure 3.1 An illustration of camera obscura [26].

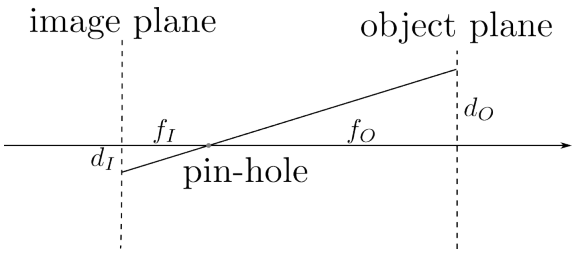

Figure 3.2 Geometrical relationship between image size and object size can be viewed as similarity triangles.

Pin-hole model is originated from camera obscura, a latin word for dark chamber. It is a image-capturing method consist of a dark room and a small hole on a wall. The image of the object world is projected onto the wall through the pin-hole. The geometrical relationship between the image and real world is given by the similarity triangles. The ratio of the image size to the real object size (d_I/d_O) is identical to the ratio of the distance between pin-hole and the wall to the distance between pin-hole and the real object (f_I/f_O). I.e. the image szie is in propoertion to the object size. This model is fundamental to camera photogrammetry, since the real object size can be reconstructed from image size using simple formula (3.1).

$$d_I = \frac{f_I}{f_O} d_O \tag{3.1}$$

doi:10.6342/NTU202400740

3.3 Camera matrix

Pin-hole camera model plays an essential role in camera matrix. It's assumed that the camera works similar to a camera obscura. Based on the geometrical relationship in Eq. (3.1), slightly more complex geometrical-relation between object and image can be established, and the camera coordinate system (CCS) can be defined. In the context of this model:

1. **Camera center is the pin-hole**: The pin-hole represents the camera center. It's the point where all light rays pass through. In reality, the exact position of camera center is typically unknown or even non-existent. However, there are some spots such as center of entrance pupil where all light rays approximately intersect can be viewed as a pin-hole. In the CCS, it serves as the origin (0,0,0).

2. **Camera sensor is the image plane**: The camera sensor is composed of a 2 dimensional array of photo-detectors. The x-axis and y-axis of the image plane is usually denoted as u and v axes. u-axis (horizontal axis) is pointing toward the right edge of the image, and v-axis (vertical axis) is pointing toward the bottom edge of the image. This is the conventional notation for image coordinate system. For CCS, the x and y axes are parallel to the u and v axes respectively, with origin being the camera center.

3. **Optical axis is defined by the light ray passes through the pin-hole and perpendicular to image plane**: Given the fact that pin-hole is the origin, the line that passes through the origin and perpendicular to the xy-plane (i.e. perpendicular to the image plane) is z-axis. Thus, the optical axis is also the z-axis of the CCS.

Understanding these premises is fundamental for comprehending the physical mean-

doi:10.6342/NTU202400740

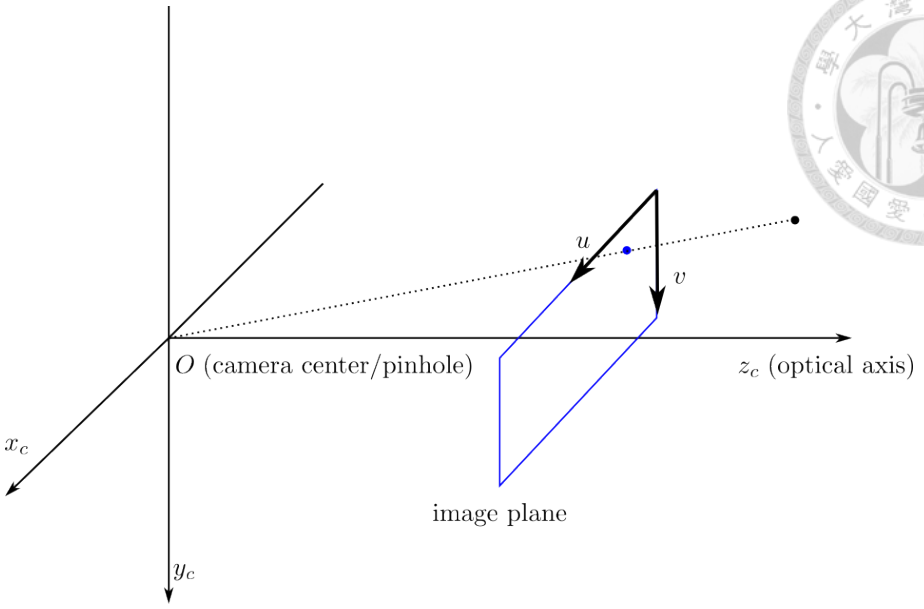

Figure 3.3 Illustration of CCS and the image-formulation scheme.

ing behind camera matrix, which is the essential principle behind how 2D images are generated from 3D scenes. According to (add reference), the transformation from 3D coordinates to 2D coordinates is done by a 3-by-4 matrix

$$\begin{bmatrix} u \\ v \\ 1 \end{bmatrix} = \mathbf{P}_{3\times4} \begin{bmatrix} x \\ y \\ z \\ 1 \end{bmatrix} \tag{3.2}$$

where 2D coordinates, more specifically image coordinates, $[u\ v\ 1]^\intercal$, and 3D coordinates $[x\ y\ z\ 1]^\intercal$ are represented in homogeneous coordinates. The camera matrix, a.k.a. transformation matrix $\mathbf{P}_{3\times4}$, is composed of camera intrinsic parameters and camera extrinsic parameters. In a complete form, $\mathbf{P}_{3\times4}$ can be decomposed into

$$\mathbf{P}_{3\times4} = \mathbf{K}\mathbf{R}\left[\mathbf{I}\middle|-\vec{\mathbf{T}}\right] \tag{3.3}$$

where matrix $\mathbf{K}$ is the camera intrinsic matrix, matrix $\mathbf{R}$ and vector $\vec{\mathbf{T}}$ are the rotation matrix and translation vector respectively. The elements in matrix $\mathbf{R}$ and vector $\vec{\mathbf{T}}$ are called camera extrinsic parameters. The transformation can then be written in a more

doi:10.6342/NTU202400740

explicit manner.

$$\begin{bmatrix} u \\ v \\ 1 \end{bmatrix} = \mathbf{K} \begin{bmatrix} x_c \\ y_c \\ z_c \end{bmatrix} = \mathbf{KR} \left[\mathbf{I} \middle| -\vec{\mathbf{T}} \right] \begin{bmatrix} x_w \\ y_w \\ z_w \\ 1 \end{bmatrix} \tag{3.4}$$

$[x_c\ y_c\ z_c]^\intercal$ and $[x_w\ y_w\ z_w\ 1]^\intercal$ represent object points in camera coordinates and homogeneous world coordinates respectively. The camera intrinsic matrix is defined as follows

$$\mathbf{K} = \begin{bmatrix} f_x & s & o_x \\ 0 & f_y & o_y \\ 0 & 0 & 1 \end{bmatrix} \tag{3.5}$$

where f_x and f_y represent focal length in x-direction and focal length in y-direction respectively. s represent skew factor of the camera pixels. s is 0 if the camera pixels are arranged orthogonally without skewness. The offset values, denoted as o_x in the x-direction and o_y in the y-direction, represent the deviation of the origin of the image coordinate system from the z-axis of the CCS. These offset values are used to describe the translation or displacement of the image's origin, the top-left corner of the image, from the camera's optical axis.

It's essential to ensure that all units in this matrix **K**, except for the skew factor s, are consistent. In particular, when dealing with the focal length and offset in a camera system, they should be expressed in the same units to maintain consistency. For instance, if the focal length is specified in millimeters, the offset should also be provided in millimeters to ensure that all measurements are in the same unit. To facilitate this, it's necessary to know the pixel size of the camera. Knowing the pixel size allows you to convert the offset from pixel coordinates to a physical unit, such as millimeters.

doi:10.6342/NTU202400740

3.4 Coordinate transformation and rotation in 3D Euclidean space

As mentioned in Eq. (3.3) in previous section, the projection from 3D WCS to 2D image coordinate system is related to camera intrinsic and extrinsic parameters. The intrinsic parameters are

1. focal length: f_x, f_y
2. offset of image center: o_x, o_y
3. skew factor: s

These parameters directly affect how 3D objects are projected onto the 2D plane, and they are dependent to the camera specifications. On the other hand, the extrinsic parameters are the parameters regarding the transformation from WCS to CCS and can be decomposed into rotation and translation. This portion of camera matrix do nothing more than describing where the object is located and how it is oriented relative to the camera center and camera sensor. Particularly, the extrinsic parameters are

1. Rotated angles: α, β, γ
2. Translated distances: l_x, l_y, l_z

In essence, the extrinsic parameters dictate how the resulting image would appear when the object is positioned or oriented differently, as if the camera were capturing the same object from varied angles. Importantly, the extrinsic parameters are independent of

doi:10.6342/NTU202400740

the camera's technical specifications. Instead, they are tied to the definition of the x, y, and z axes in the WCS.

The definition of translation vector in the camera matrix is straight-forward. It is the vector pointing from the origin of WCS to the origin of the CCS. The translation vector $\vec{\mathbf{T}}$ is expressed as $[l_x,\ l_y,\ l_z]^\intercal$, where the components are the translated distances on each axes in WCS. The latter part of Eq. (3.4) can be rewritten as

$$\left[\mathbf{I}\middle|-\vec{\mathbf{T}}\right]\begin{bmatrix}x_w\\y_w\\z_w\\1\end{bmatrix}=\begin{bmatrix}1&0&0&-l_x\\0&1&0&-l_y\\0&0&1&-l_z\end{bmatrix}\begin{bmatrix}x_w\\y_w\\z_w\\1\end{bmatrix}=\begin{bmatrix}x_w-l_x\\y_w-l_y\\z_w-l_z\end{bmatrix} \tag{3.6}$$

This calculation can be interpreted as moving the point from homogeneous WCS to another coordinate system with the same origin as the CCS.

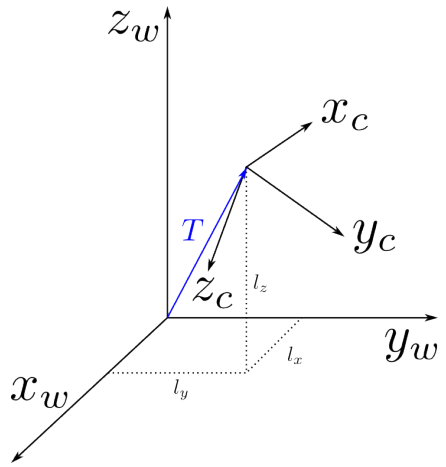

(a) Before translation, a point in the WCS has a different coordinates when represented in CCS.

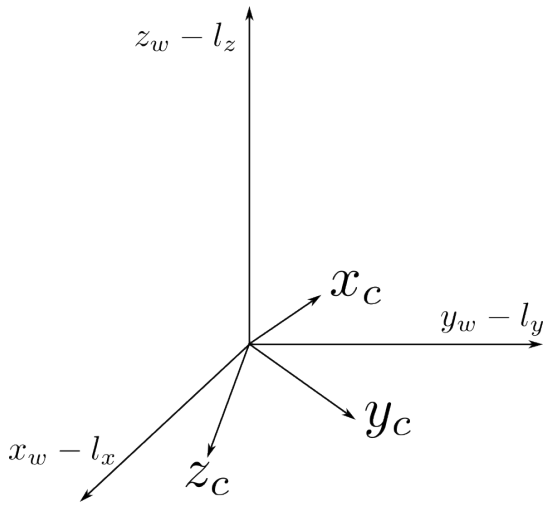

(b) After translation, points are represented in CCS with correct rotation matrix applied.

Figure 3.4 Interpretation of the calculation in (3.6).

As for rotated angles, it is not so straight-forward when dealing with consecutive rotations w.r.t. different axis. Every rotation is performed w.r.t. an axis, and the position of the axis changes when intrinsic rotation is considered (See Fig. 3.5b). There are many ways to define rotated angles. One of the most common way is by the convention of Euler

doi:10.6342/NTU202400740

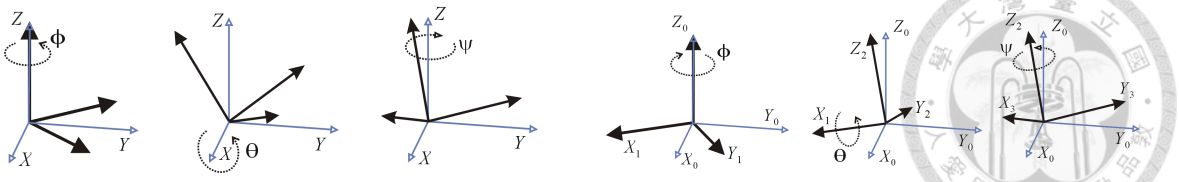

(a) Illustration of extrinsic rotation. The rotation axex are not on the object.

(b) Illustration of intrinsic rotation. The rotation axes move with the object.

Figure 3.5 Differences between extrinsic rotation and intrinsic rotation [27, 28].

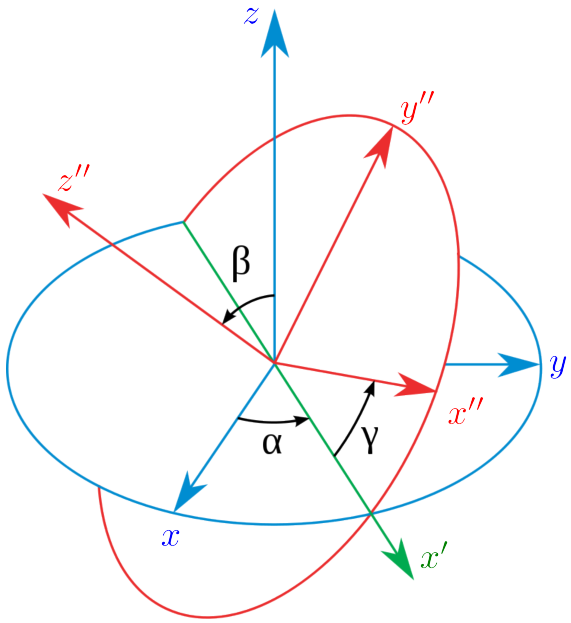

Figure 3.6 Classic Euler angles geometrical definition (z-x'-z'' convention, intrinsic rotation) [29].

angles. As illustrated in Fig. 3.6, the rotated angles α, β and γ are defined by the rotation w.r.t. z-axis, x'-axis and z''-axis respectively. x'-axis is the new x-axis after the first rotation, and z''-axis is the new z-axis after the second rotation. The overall transformation after 3 consecutive rotations following z-x'-z'' convention can be represented by a rotation matrix $\mathbf{R}$.

$$\mathbf{R} = \mathbf{R}_{zx'z''} = \begin{bmatrix} c_\alpha c_\gamma - c_\beta s_\alpha s_\gamma & -c_\alpha s_\gamma - c_\beta c_\gamma s_\alpha & s_\alpha s_\beta \\ c_\gamma s_\alpha + c_\alpha c_\beta s_\gamma & c_\alpha c_\beta c_\gamma - s_\alpha s_\gamma & -c_\alpha s_\beta \\ s_\beta s_\gamma & c_\gamma s_\beta & c_\beta \end{bmatrix} \tag{3.7}$$

The matrix in Eq. (3.7) can be used to describe any orientation in 3D Euclidean space. The elements are written in simplified form, where c indicates cosine and s indicates sine

doi:10.6342/NTU202400740

(e.g. $c_\alpha = \cos\alpha$). The minimum range of cover for Euler angles are defined in Table 3.1.

Table 3.1 Ranges of Euler angles defined in z-x'-z'' convention.

Euler angle	**Range**
α	$[0, 2\pi)$
β	$[0, \pi]$
γ	$[0, 2\pi)$

After defining the matrix operation for rotation in 3D Euclidean space, definition of surface tilting can be established using similar manner. Tilting of a surface can be viewed as the orientation of the local surface w.r.t. WCS. The default position of the surface is laying on the $x_w y_w$ plane, and the normal vector is aligned with z_w-axis, the z-axis of WCS. To distinguish from the z-x'-z'' convention used for describing camera extrinsic parameters, the z-y'-z'' convention is used for describing tilting angles. The orientation of the normal vector w.r.t. WCS can then be defined by Euler angles α and β. Since the rotated object is planar, the orientation remains the same for any γ angle. Therefore, the Euler angle γ is omitted when describing surface tilting.

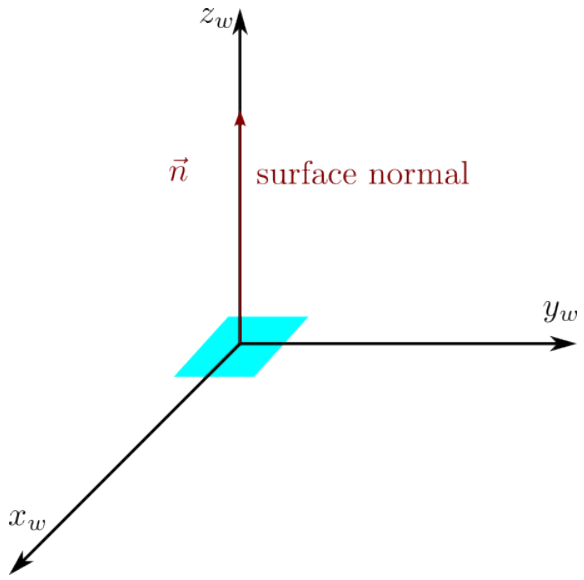

Figure 3.7 Default position of the local surface. The surface normal is aligned with z_w-axis.

doi:10.6342/NTU202400740

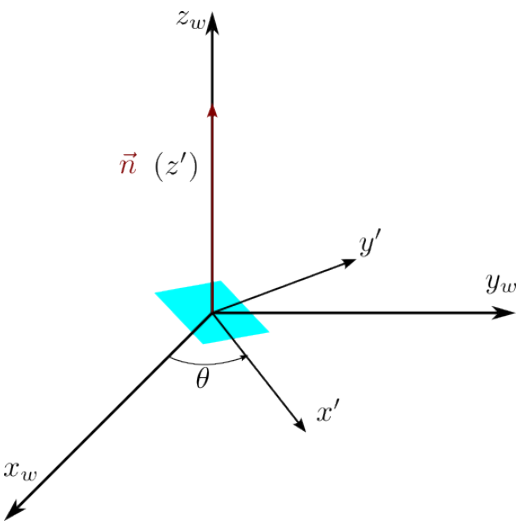

Figure 3.8 The surface is rotated w.r.t. the z axis of WCS.

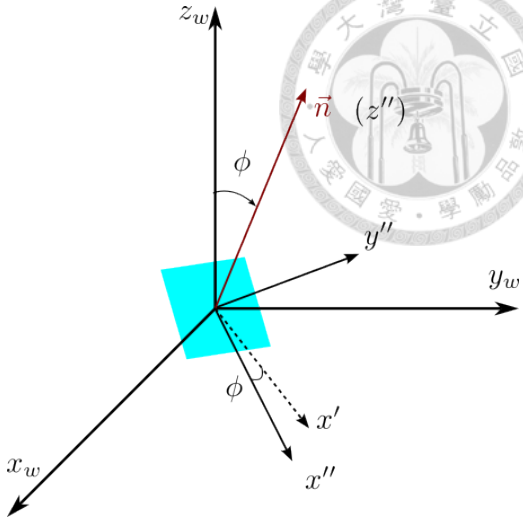

Figure 3.9 The surface is rotated w.r.t. the y axis of the coordinate system after first rotation, i.e. y' axis.

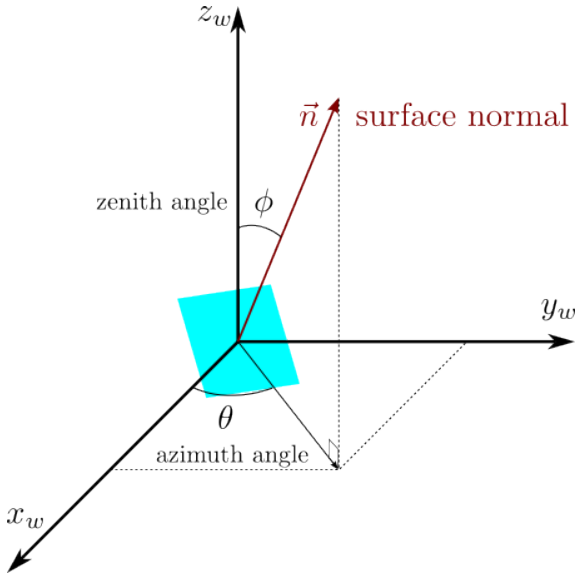

Figure 3.10 Illustration of azimuth angle and zenith angle of a tilted surface.

doi:10.6342/NTU202400740

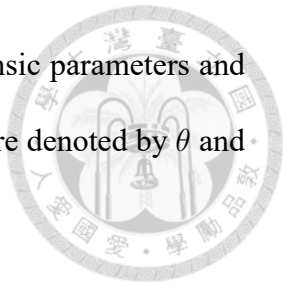

To avoid confusion between Euler angles used for camera extrinsic parameters and Euler angles used for surface tilting angle, the surface tilting angles are denoted by θ and ϕ, where α and β are replaced by θ and ϕ respectively.

Table 3.2 Ranges of surface tilting angles.

Tilting angle	**Alias**	**Range**
θ	Azimuth angle	$[0, 2\pi)$
ϕ	Zenith angle	$[0, \pi/2]$

In fact, the surface tilting angle ϕ has a shorter range, $\phi \in [0, \pi/2]$, because tilting angle ϕ in $(\pi/2, \pi]$ implies that the surface normal is pointing downward, which means the surface is facing to the ground. Based on typical triangulation setups, the light source and the camera are typically placed above the object, i.e. where $z_w > 0$, so the downward-facing surfaces are not observable.

Tilting angles θ, ϕ can also be interpreted in another sense. Solar altitude angles, azimuth and zenith angles, are used to describe the relative angles between the earth's horizon and the sun. This idea can be used to describe the rotation of surface normal vector. The WCS has to be considered in the definition of azimuth angle and zenith angle. The azimuth angle of the surface normal vector is the angle between x_w axis and the projection of normal vector on $x_w y_w$ plane. The zenith angle is the angle between z_w axis and the normal vector. In this way, θ and ϕ are equivalent to azimuth and zenith angle respectively. The concept is also similar to the azimuthal angle and polar angle in spherical coordinate systems.

doi:10.6342/NTU202400740

Chapter 4 System Setup and Methodology

4.1 Preface

In this chapter, the setup of the measuring system is introduced, followed by a thorough description of the principle behind the reconstruction algorithm. The purpose of bringing up the hardware description is to provide readers with an understanding of the types of measuring instruments which this algorithm can be applied to. It is crucial to understand some system specifications and properties in order to develop a general solution. The algorithm is not necessarily restricted to this particular hardware; instead, the algorithm can be generalized to any triangulation line scanner that projects a line light pattern and captures images from an angle.

4.2 System setup

The system is basically a LED line light scanner based on triangulation. The system setup in this research consists of one light-projecting module and one imaging module, and it is based on previous work by Huang [30]. The imaging module is composed of a

doi:10.6342/NTU202400740

camera and an objective lens, while the light-projecting module projects a single line pattern into the field of view of the camera. The scanning mechanism is achieved by placing a galvanometer mirror in-between two f-θ lenses. The line light pattern is generated by the light passing through the lenticular lens.

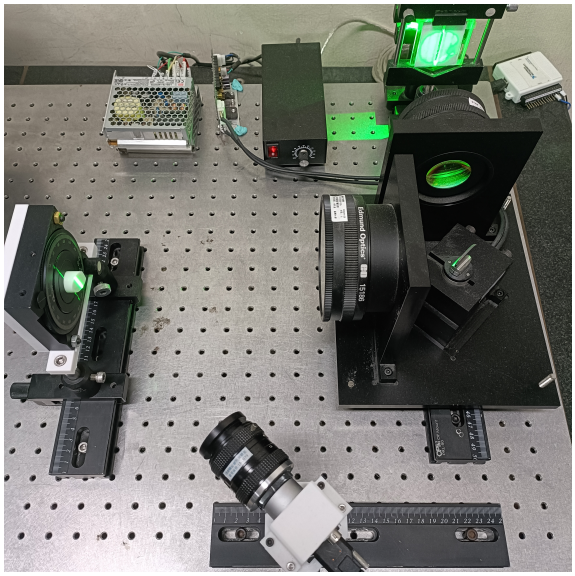

Figure 4.1 Schematic diagram of the system setup.

The methodology proposed in the following section can be applied to other systems using similar setup. As long as the system utilizes triangulation and projects line-patterned light, the methodology can be applied.

doi:10.6342/NTU202400740

4.3 Measurement of 3D coordinates

In this section, we present a 3D reconstruction method inspired by the work outlined in the paper by Chen [31]. The referenced paper proposes an algorithm to reconstruct the 3D coordinates from a laser triangulation system without the need of camera calibration. However, the system in this research is required to have the ability to measure tilting angle of a surface. The proposed model for tilting angle measurement relies on precise intrinsic parameters, making a conventional camera calibration procedure still necessary.

The concept behind the 3D coordinate reconstruction can be visually explained by the graph below.

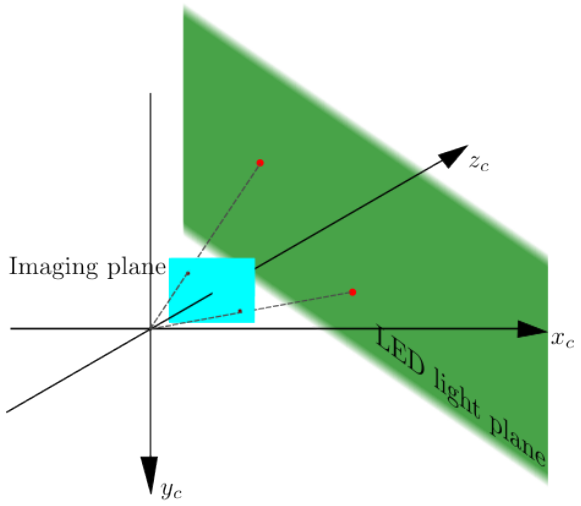

Figure 4.2 The intersection of the reprojection light ray and the light sheet is the position of the object.

When considering the reprojection of a point from a 2D image to 3D world, there are infinitely many points of possible outcome. Since a point in a 2D image represent a ray of light in a 3D coordinate, any point on the same light ray will be captured by the camera on the same position of camera sensor. On the other hand, the projected light plane from the light source acts a constraint. For any objects, only the segment that is intersected with

doi:10.6342/NTU202400740

the light plane is illuminated. Any other part that is out of the light plane would be dark. Hence, the reprojection of a point only has one outcome in this setup.

4.3.1 Calibration of camera

The calibration of the system in section 4.2 only consists of 2 main steps, first the calibration of the camera and second the calibration of the light plane in the camera coordinate system. In this research, the conventional Zhang's method [32] is used for calibrating the camera. The procedure of camera calibration is briefly introduced here. Before performing Zhang's calibration, adjustment of the measuring system should be done, so that the calibrated result matches actual measuring scenario. First, the working distance of the system should be specified, and place a flat object at the working distance from the light projector module. Next, zero the galvanometer mirror, so the light sheet is projected from the center of the f-θ lens. Fix the camera in place, and adjust the viewing angle such that the line pattern on the flat object appears to be in the middle of the FOV. Next, adjust the focal length of the objective lens so that it is focusing on the line pattern. Finally, the aperture of the lens, ISO, gain and shutter speed should be adjusted so that the noise is minimal and the light patterns are not over-exposed nor under-exposed with the background being dark.

At this point, Zhang's calibration can be carried out. The tool involved is a flat plate with checkerboard pattern (see Fig. 4.3). The arrangement of grid points is 7×7, with grid size $3\ mm \times 3\ mm$. First, illuminate the field of view with white light source. Next, place the checkerboard, the calibrating object, at the middle of the FOV while all the grids are not only visible, but also sharp and clear. Capture and save the first image. Next, move the checkerboard around inside the FOV and capture the images until there are 20 to 30

doi:10.6342/NTU202400740

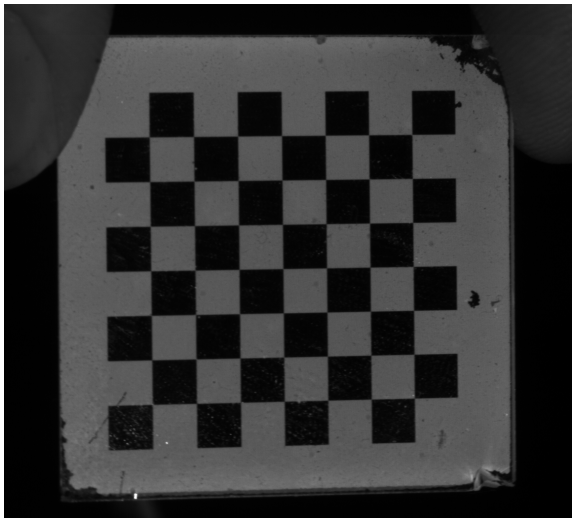

Figure 4.3 Checkerboard is used as a medium for camera calibration.

captured images of checkerboard.

The grid points of the checkerboard serve as the reference points for calibration. Using OpenCV open source, one can extract the position of the grids automatically. In fact, there is a developed function in OpenCV to perform the Zhang's calibration. Users need to provide the captured images of checkerboard and the actual dimension of the grid. The function would calculate the intrinsic parameters of the camera. Details of the algorithm is not a content to be discussed here. In essence, one just need to know that the function is essentially a fitting process. It takes the actual distance between grid points provided by user as ground truth, and takes the pixel position of the grid points from every image to fit the camera matrix through least square method.

4.3.2 Calibration of LED light plane

After camera calibration is done, one needs to calibrate the light sheet. The goal of this procedure is to extract the position of the light sheet in the camera coordinate system. Namely, by calibrating the light sheet, the planar equation of the light sheet in CCS can be obtained.

doi:10.6342/NTU202400740

The procedure to obtain planar equation is similar to the method proposed by Chen [31]. However, since there is a scanning mechanism in the setup (section 4.2), the procedure is slightly different from the one proposed in the original paper. There are totally 250 images in the scanning sequence. For each scanning position, the planar equation for the light sheet has to be calibrated in order to reconstruct the accurate scanning profile. Although the calibration of 250 light sheets is doable, it is not a practical method. Given the property of the scan lens (f-θ lens in Fig. 4.4) and the control scheme of the galvanometer mirror (moving at a constant angular velocity, i.e. identical rotated angle each step), it is known that the light sheet moves forward a fixed distance in every consecutive image. Hence, the calibration of 250 light sheets can be reformulated as a calibration of a single light sheet and the moving distance of the light sheet in one step.

It is assumed that the telecentric error of the f-θ lens is neglectable, s.t. the light planes at every position are parallel to each other.

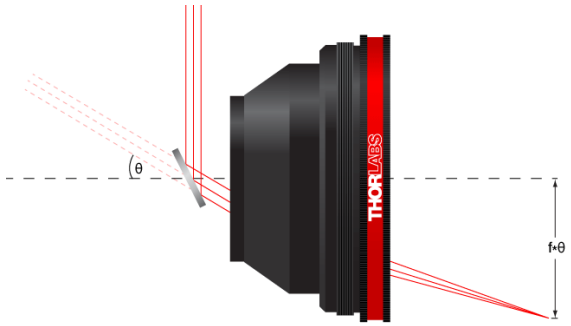

Figure 4.4 The f-θ lens projects the light beam on $f\theta$ unit away from the optical axis when the galvanometer mirror is rotated at θ radian angle.

The calibrating target is a 3D printed strip as shown in Fig. 4.5. At the center of the strip, there is a hole with diameter $2\ mm$. The curved edges of the strip are actually two sections of a larger circle with diameter $30\ mm$. When calibrating, it is required that the light sheet creates a line pattern on the strip while the line pattern crosses both of the curved edges and the hole at the center. This way, three feature points are created, the edge

doi:10.6342/NTU202400740

points and the middle point. The ground truth distance between 2 edge points is 30 mm, and the distance between middle point to any one of the edge points is 15 mm.

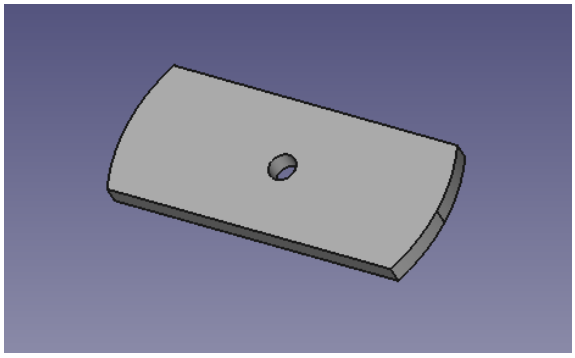

Figure 4.5 The calibration object for light sheet.

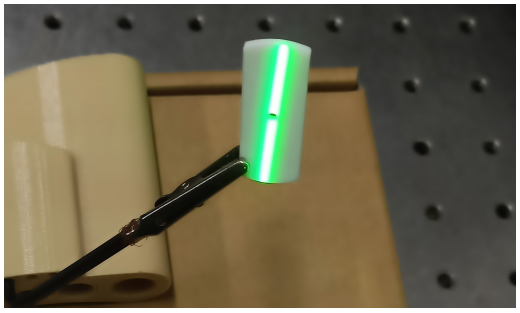

Figure 4.6 Calibration target intersected with light sheet.

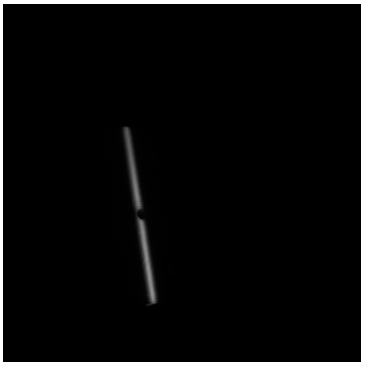

Figure 4.7 Each image of calibration target has 3 feature points to be extracted.

Given these referencing dimension and the observed distances in pixel coordinates, the actual position of these feature points can be calculated and represented in CCS (refer to [31] for explicit formulae). These feature points serve as sampling points of the light sheet. Totally 24 sampling points are obtained by capturing the images of the calibrating strips at different positions in the light plane. Planar equation of the light sheet in the CCS can be obtained by performing a plane fitting on the sampling points.

The procedure described previously can be applied to calibration of fixed light sheet. However, there is a scanning motion of the light sheet in the setup of this research. Step size of the light sheet also needs to be calibrated. To obtain the step size of the light sheet, the light sheet is moved to the initial position, middle position and the final position. There

doi:10.6342/NTU202400740

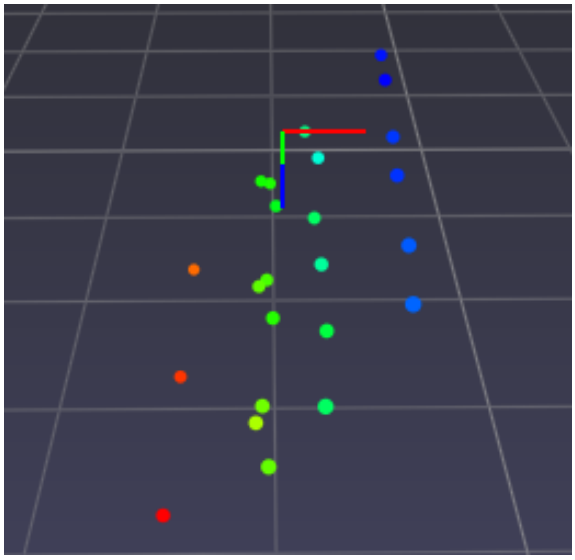

Figure 4.8 Positions of the calibrating feature points (initial plane) in CCS shown in point cloud format.

are 24 sampling points for the light sheet in each position, that is 72 sampling points in total for calibrating the step size.

A modified linear regression is applied on these 72 sampling points to extract the step size. Similar to the case for single light sheet, 3 light sheets, 1 for each position, are fitted simultaneously. Different from ordinary linear fitting technique, a dummy variable is introduced here to represent the position of the sampling point. This method is widely used in regression analysis for categorical data.

In ordinary plane fitting, the following linear model is used

$$Y = \beta_0 + \beta_1 X_1 + \beta_2 X_2 \tag{4.1}$$

the ultimate goal is to find the planar equation representing the light sheet in CCS, which is

$$Ax_c + By_c + Cz_c + D = 0 \tag{4.2}$$

doi:10.6342/NTU202400740

By re-scaling the equation, one variable can be reduced, so (4.2) becomes

$$\frac{A}{C}x_c + \frac{B}{C}y_c + z_c + \frac{D}{C} = 0 \tag{4.3}$$

$$ax_c + by_c + z_c + c = 0 \tag{4.4}$$

Re-arranging (4.4) we get

$$-z_c = c + ax_c + by_c \tag{4.5}$$

which has the same form as the linear regression model stated in (4.1). By assigning the 3D coordinates of the sampling points in CCS, the values of a, b and c can be fitted. Thus, the planar equation can be obtained.

To extract step size of the light sheet, the following linear model is used

$$Y = \beta_0 + \beta_1 X_1 + \beta_2 X_2 + \beta_3 X_3 \tag{4.6}$$

$$-z_c = c + ax_c + by_c + \lambda\delta_c \tag{4.7}$$

Eq. (4.7) is the modified version of Eq. (4.5), where the third variable δ_c is a dummy variable. It is assigned -1 for sampling points in initial light plane, assigned 0 for sampling points in middle plane, and assigned 1 for sampling points in final plane. This way, the sampling points are shifted fixed distance λ in z_c-direction, so that all the sampling points are one the same plane as the light plane in middle position. After fitting all the points, not only can the planar coefficients, a b and c, be known, but also the distance in z_c-direction between middle plane and initial plane, λ, can be obtained. Since there are 250 images in the sequence, dividing the fitted value of λ by 125, the step size of the light plane in z_c-direction can be obtained.

After computing the planar equation, defining the WCS becomes straightforward.

doi:10.6342/NTU202400740

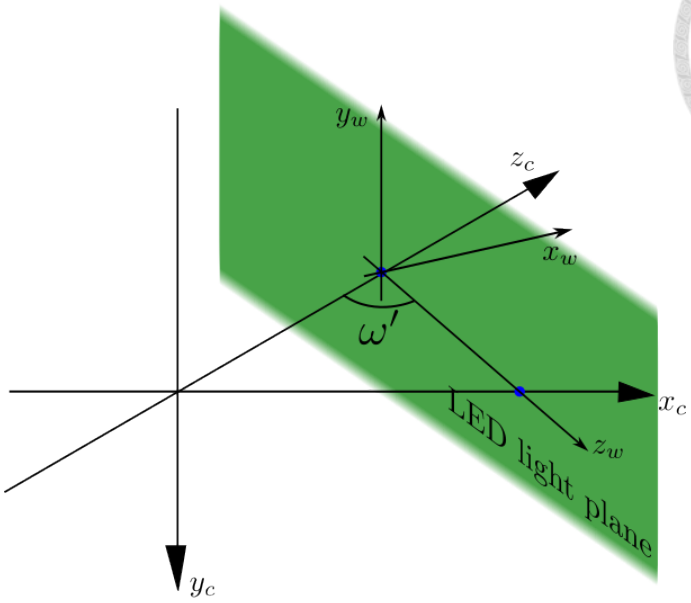

Figure 4.9 Spatial relationship between CCS and WCS. Blue dots are the intercepts of the plane on the axes.

Instead of referencing the calibration checkerboard, the light plane serves as the reference for the WCS. The light plane is set at the central position within the scanning range, i.e. $\delta_c = 0$. As illustrated in Fig. 4.9, the z_c-intercept is designated as the origin of the WCS. The line connecting the z_c and x_c intercepts of the light plane forms the z_w-axis. Subsequently, y_w-axis is defined to be the axis crossing z_c-intercept, parallel to y_c-axis and perpendicular to z_w-axis. x_w-axis can be defined accordingly, and it is laying on x_c-z_c plane.

It can be observed from the relative position of WCS and CCS that there is a right triangle formed by z_w-axis, z_c-axis and x_c-axis. The sharp angle between z_w-axis and z_c-axis is ω'

$$\omega' = \arctan\frac{1}{a} \tag{4.8}$$

The derivation for this equation is given in later chapter. Given this information, the rotation matrix and the translational vector can be calculated. As stated in chapter 3, the

doi:10.6342/NTU202400740

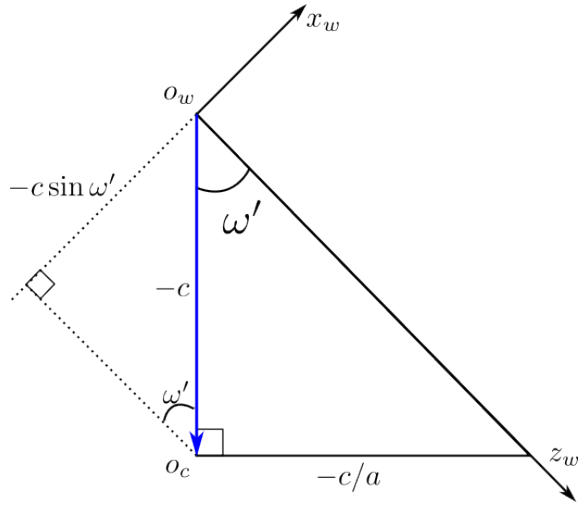

Figure 4.10 The geometric relationship between WCS and CCS. Blue vector indicates the translational vector $\vec{\mathbf{T}}$.

rotation matrix can be calculated using (3.7) by plugging the corresponding Euler angles. The Euler angles α, β and γ are calculated as below. The illustrative explanation are provided in Fig. 4.11 to Fig. 4.14.

$$\alpha = \pi/2 \tag{4.9}$$

$$\beta = \pi + \omega' = \pi + \arctan\frac{1}{a} \tag{4.10}$$

$$\gamma = \pi/2 \tag{4.11}$$

The translational vector from the origin of WCS to the origin of CCS can be calculated using fundamental trigonometry. From Fig. 4.10 above, the translation vector can be easily calculated

$$\vec{\mathbf{T}} = \begin{bmatrix} c\sin\omega' & 0 & -c\cos\omega' \end{bmatrix}^\intercal = \begin{bmatrix} c\sin(\arctan\frac{1}{a}) & 0 & -c\cos(\arctan\frac{1}{a}) \end{bmatrix}^\intercal \tag{4.12}$$

doi:10.6342/NTU202400740

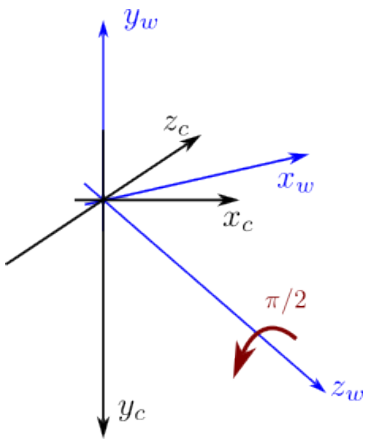

Figure 4.11 The initial orientation of WCS and CCS are mismatched. Rotate WCS w.r.t. z_w-axis at $\pi/2$ radian to get Fig. 4.12.

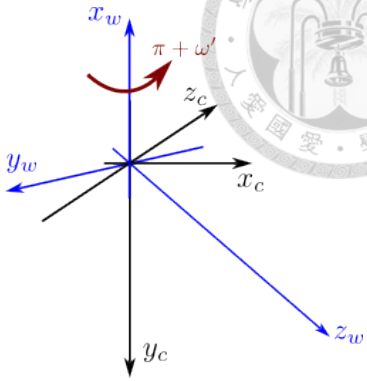

Figure 4.12 Rotate WCS w.r.t. x_w-axis at $\pi + \omega'$ radian to get Fig. 4.13.

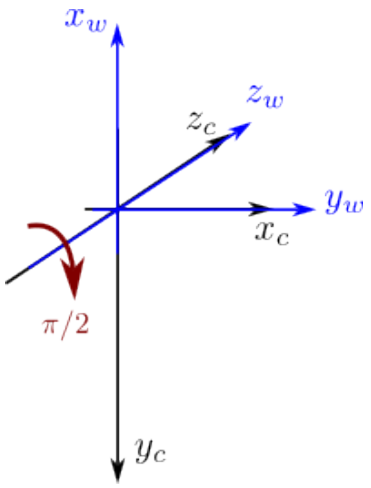

Figure 4.13 Rotate WCS w.r.t. z_w-axis at $\pi/2$ radian to get Fig. 4.14.

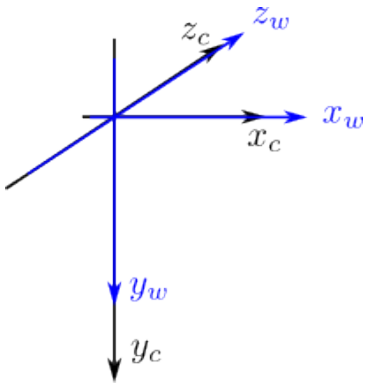

Figure 4.14 WCS and CCS are now aligned.

doi:10.6342/NTU202400740

4.3.3 Profile reconstruction

In practice, the light sheet is not an ideal plane. The light sheet possesses finite thickness, causing the ambiguity of determining the precise position of the plane. When projected onto a surface, it forms a line pattern with non-infinitesimal width. This makes the precise determination of intersection between the light plane and the surface become complicated. This inherent characteristic constitutes a fundamental source of uncertainty in 3D coordinate reconstruction.

Given a grayscale image of the line pattern, the intersection of the light plane and the object can be determined/estimated using ridge detection, e.g. gray-gravity method, Steger algorithm. The fundamental concept behind ridge detection is to find the zero-crossing point in the first-derivative of the intensity profile, which corresponds to the peak of the original intensity profile. However, the first-derivative can be heavily influenced by the noise existing in the raw image. Therefore, pre-processing techniques such as Gaussian blurring is often applied to smoothen the intensity profile, and reducing the effect from high frequency noise.

In this research, row-wise Gaussian fitting is utilized for determining the intersection line. In comparison with ridge detection, this method does not require any pre-porcessing on the raw image. Instead, one-dimensional Gaussian profile is fitted on every row in the raw image. The mean of the Gaussian distribution is then taken to be the intersection of the light plane and the object.

doi:10.6342/NTU202400740

4.4 Measurement of surface tilting angles θ and ϕ

This section proposes a novel method of reconstructing surface tilting angle using single raw image of line-patterned light in a triangulation system. The principle behind the model of tilting angle reconstruction stems from the observation of the line patterns at different surface tilting. As can be seen in the example pictures below (Fig. 4.15), the width and the intensity of the line changes as the surface tilting angle changes. The changes in appearance of the pattern show that changes of tilting angles can be observed. Thus, these 2 features can be the key indicators of the orientation of the surface. As mentioned in chapter 3, tilting angles can be represented in 2 variables, azimuth angle θ, and zenith angle ϕ. The azimuth and zenith angles simultaneously affect the appearance of the pattern. In order to reconstruct tilting angles from single image of line-patterned light, theoretical relationship between tilting angles, width and intensity should be elaborated.

The upcoming sections present two forward models: one mapping tilting angles to linewidth and the other mapping tilting angles to intensity. The concluding section introduces the solution for the inverse of these 2 models. Reconstruction of tilting angles from the outputs of two forward models can be seen as an inverse problem. The inverse model takes the linewidth and intensity as inputs and infers corresponding tilting angles as outputs. Note that linewidth and intensity of the line patterns are the only observable information in a given image, and these features exactly conveys the information about the tilting angle of the local surface.

doi:10.6342/NTU202400740

4.4.1 Linewidth as a function of tilting angles

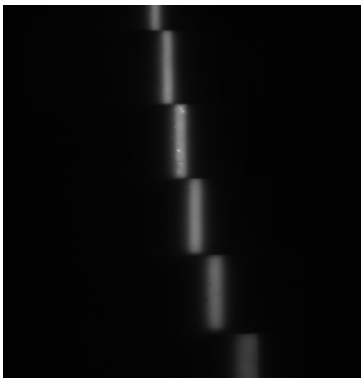

Figure 4.15 The shape and the brightness of projected line pattern changes according to different tilting angles at the local area.

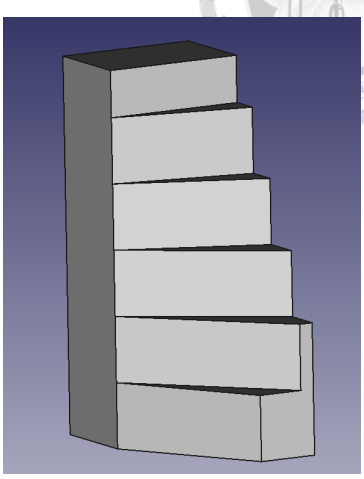

Figure 4.16 3D CAD model of the scanned object in Fig. 4.15.

As evident from the images acquired by the system (refer to section 4.2 for the system setup), the linewidth of the line pattern varies with alterations in the surface tilting angle. To accurately describe these changes, it is crucial to provide a clear definition of linewidth. Given the absence of distinct boundaries in actual images, the linewidth is defined as the full width at half maximum (FWHM) of the row-wise intensity profile.

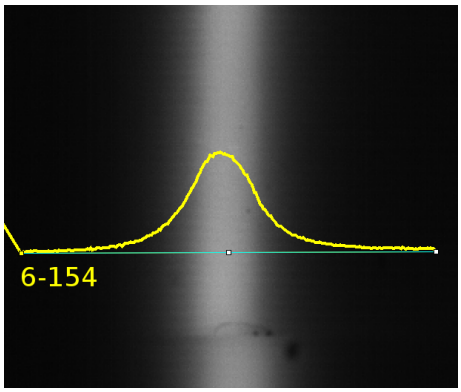

Figure 4.17 Cross-sectional intensity profile (yellow curve) can be fitted by a Gaussian distribution. The curve is plotted through ImageJ.

Furthermore, the intensity profile is modeled by a Gaussian distribution. Note that

doi:10.6342/NTU202400740

the FWHM of a Gaussian distribution is given by the equation below

$$\text{FWHM} = 2\sqrt{2\ln 2}\sigma \tag{4.13}$$

where σ is the standard deviation of the Gaussian distribution. Hence, the linewidth of the light pattern is expressed in terms of the standard deviation of the intensity distribution.

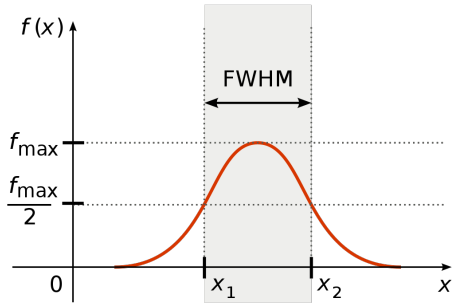

Figure 4.18 Illustration of full width at half maximum (FWHM) of a curve [33].

The relationship between FWHM of the line pattern and the tilting angles can be expressed by the formula below

$$\text{FWHM} = |u(t_1) - u(t_2)| \tag{4.14}$$

where t_1 and t_2 are defined as

$$t_1 = \delta + 0.5\arccos(\frac{2D^2}{E^2} - 1) + \pi \tag{4.15}$$

$$t_2 = \delta - 0.5\arccos(\frac{2D^2}{E^2} - 1) + \pi \tag{4.16}$$

Note that δ, D and E are all functions of surface tilting angles (ϕ and θ), along with camera intrinsic parameters and extrinsic parameters. The function u is the parametric form of the u coordinate of the ellipse representing the light spot. The details for the explicit form of these symbols are covered in Appendix A.

The derivation details are omitted in this chapter; however, the idea can be briefly

doi:10.6342/NTU202400740

described as follows: To explore the correlation between tilting angles and linewidth, we conceptualize line patterns as an aggregation of individual light spots, and the spots are modeled by bivariate Gaussian distribution (see Fig. 4.19 for illustration). Also, the surface tilting is assumed to be uniform with in a small neighborhood of the light spot.

This reformulation enables us to examine the relationship between tilting angles and the lateral spot size, which is defined as the distance between the leftmost and rightmost edges of a light spot.

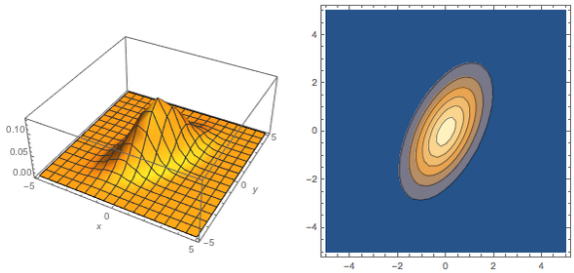

Figure 4.19 Illustration of a bivariate Gaussian distribution. Left: 3D surface; Right: color-coded map [34].

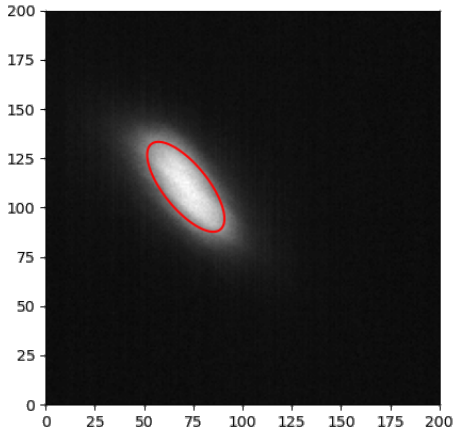

Figure 4.20 An image of a light spot. The red ellipse shows the contour of half maximum of the fitted bivariate Gaussian distribution.

The consideration of the lateral spot size is crucial as, when these light spots overlap, the information related to the major and minor axes becomes indistinguishable. Illustrative explanation is shown in Fig. 4.21. Focusing on the lateral size ensures that key information

doi:10.6342/NTU202400740

is retained even in cases of spot overlap.

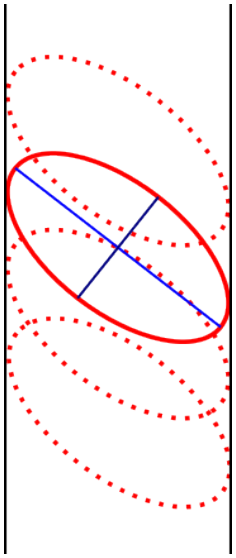

Figure 4.21 A line pattern can be seen as superposition of neighboring spots. The axes (blue lines) of original spots would be undetectable when these spots overlap.

It can also be rigorously demonstrated that the lateral spot size is precisely equivalent to the FWHM of the Gaussian cross-sectional intensity profile when the spot is modeled by a bivariate Gaussian distribution. Further details regarding this rationale are covered in Appendix B.

This concludes the brief introduction of the linewidth model as a function of tilting angles. The intent of this chapter is to offer a comprehensive overview of the entire methodology; hence, the rigorous proofs of the concept will be delayed to the appendix.

4.4.2 Intensity as a function of tilting angles

At different surface tilting angles, not only the shape but also the brightness of the projected pattern would change. Therefore, the second key feature need to be observed is the intensity of the pattern. By assuming the surface of the object is diffused, the relationship between the intensity of the reflected light and the tilting angles can be modeled by Lambert's cosine law.

doi:10.6342/NTU202400740

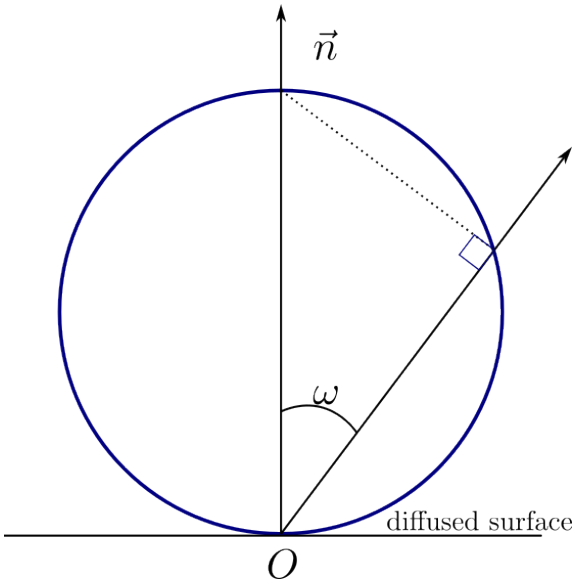

Figure 4.22 Illustration of Lambert's cosine law.

The Lambert's cosine law states that the radiant intensity is proportional to the cosine angle ω between the observer's line of sight and the surface normal vector, and it can be expressed as the formula below

$$I = I_0 \cos\omega \tag{4.17}$$

where I_0 is the intensity perceived on the surface normal vector. Or the normalized form,

$$\frac{I}{I_0} = \cos\omega \tag{4.18}$$

The value ranges from 0 to 1. To deduce the appropriate formula for the system setup, some modification must be made on the equation above. First, the normalized Lambert's cosine law can be viewed as the inner product of the surface normal vector (a unit vector) and the vector representing the observer's line of sight (also a unit vector).

With surface tilting angle already known, the surface normal vector is given by

$$\vec{n} = [\sin\phi\cos\theta,\ \sin\phi\sin\theta,\ \cos\phi]^T \tag{4.19}$$

doi:10.6342/NTU202400740

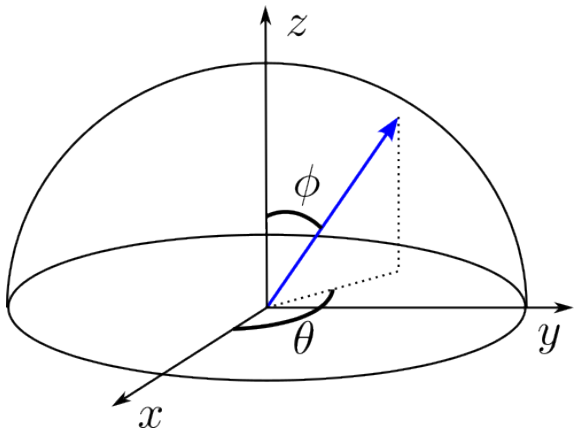

Figure 4.23 Illustrative relationship between tilting angles and surface normal vector.

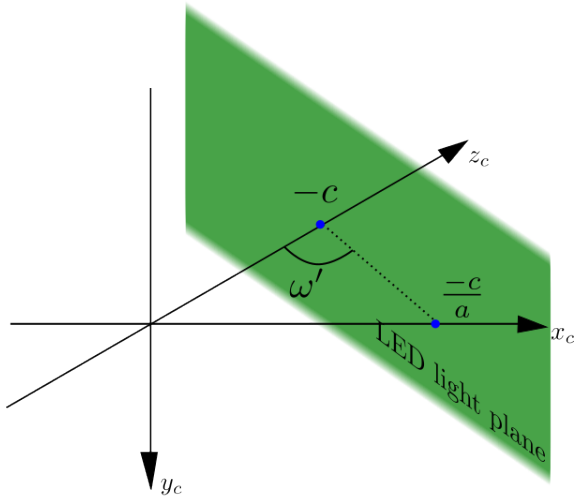

Figure 4.24 The viewing angle ω' can be calculated from the intercepts (blue dots) of the light plane on the CCS axes.

To obtain the vector of observer's line of sight, the relationship between the light plane and the optical axis of the camera must be analyzed. Recall the definition of WCS in subsection 4.3.2, the z_w-axis is the line between the z_c-intercept and x_c-intercept of the light plane. Also, recall the equation of the light sheet at middle position of the scanning range ($\delta_c = 0$)

$$-z_c = c + ax_c + by_c \tag{4.20}$$

doi:10.6342/NTU202400740

the intercept on z_c-axis can be calculated by plugging in $x_c = y_c = 0$, and the intercept on x_c-axis can be calculated by plugging in $z_c = y_c = 0$, Thus, the viewing angle ω' as shown in Fig. 4.24 can be calculated by arctangent of x_c-intercept over z_c-intercept

$$\omega' = \arctan\frac{-c/a}{-c} = \arctan\frac{1}{a} \tag{4.21}$$

Thus, the vector representing the line of sight can be written in terms of the coefficients of the planar equation of the light sheet

$$\vec{n} = [\sin(\arctan\frac{1}{a}),\ 0,\ \cos(\arctan\frac{1}{a})]^T \tag{4.22}$$

where a is the coefficient of x_c in (4.5). Thus, the normalized intensity I_n can be calculated as

$$I_n = \sin\phi\cos\theta\sin(\arctan\frac{1}{a}) + \cos\phi\cos(\arctan\frac{1}{a}) \tag{4.23}$$

4.4.3 Tilting angle reconstruction

Currently, both forward models have been established (Equation 4.14 and Equation 4.23). In measuring scenario, the inverse model is what we need to solve, i.e. given linewidth and intensity, reconstruct the tilting angles.

Mathematically speaking, the inverse problem can be described as below: "Given 2 functions $f_1(\theta, \phi)$ linewidth model, $f_2(\theta, \phi)$ intensity model, and the output values from each function L_0 and I_0 respectively, find the underlying tilting angles θ_0, ϕ_0 s.t. $f_1(\theta_0, \phi_0) = L_0$ and $f_2(\theta_0, \phi_0) = I_0$." The inverse model can be roughly thought of as a function

$$f_3 : (L, I) \to (\theta, \phi) \tag{4.24}$$

doi:10.6342/NTU202400740

To solve this, one can resort to modern methods such as deep learning models. It requires one to prepare ample amount of training dataset. The training process will eventually find the mapping from linewidth and intensity data to accurate tilting angles. However, given that we have already established the forward models explaining the direct relationship between tilting angles and linewidth/intensity, there's no need for a black-box model. The unexplainability is one of the reasons why we don't use deep learning method in the first place.

To overcome this, deeper analysis on these two forward models should be done. One can first analyze whether the inverse problem is an ill-posed problem or not. Is f_3 well-defined? One could start by analyzing the uniqueness of the range of f_3. Below are some preliminary simulated results of the forward models.

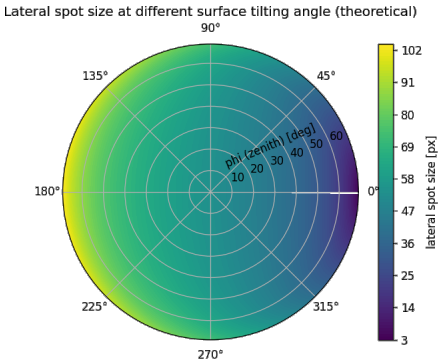

Figure 4.25 Linewidth model in color-coded map.

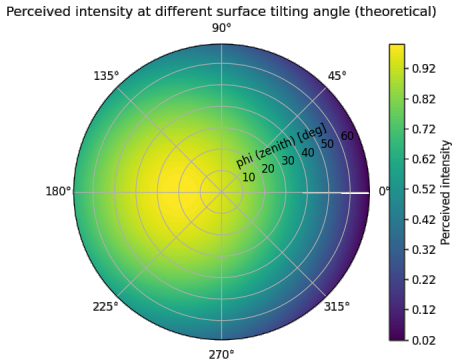

Figure 4.26 Intensity model in color-coded map.

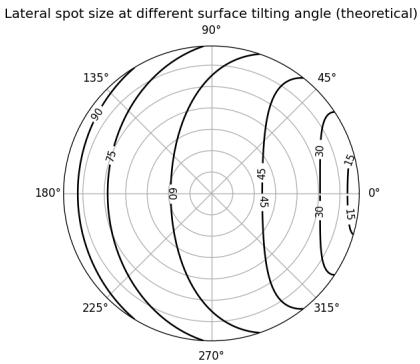

Figure 4.27 Linewidth model in contour map.

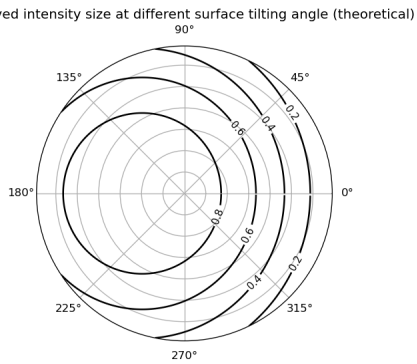

Figure 4.28 Intensity model in contour map.

doi:10.6342/NTU202400740

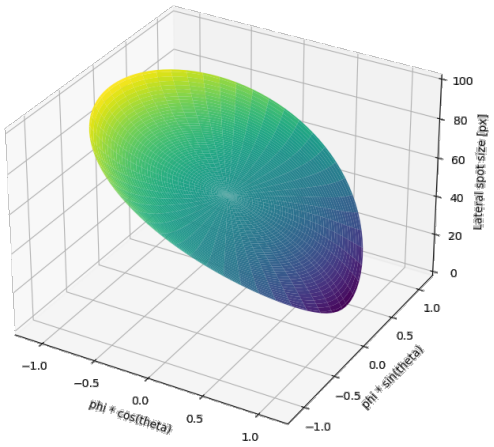

Figure 4.29 Linewidth model in 3D topographic map.

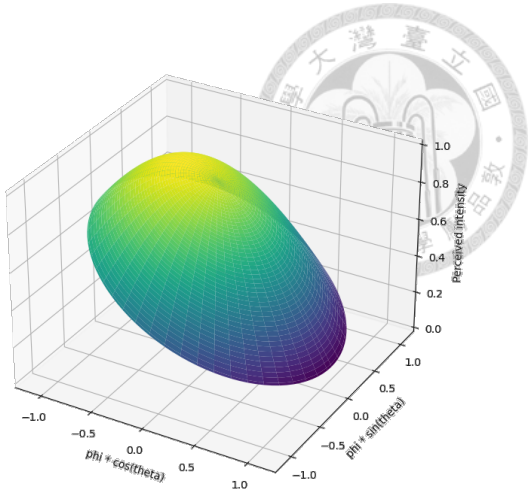

Figure 4.30 Intensity model in 3D topographic map.

The 3D topographic maps and contour maps of the forward models are plotted. They show how the values of linewidth and intensity change while the tilting angles are varying. When considering these 2 models simultaneously, one can overlap the contour maps together by matching the tilting angles and observe the pattern it creates (Fig. 4.31). Note that all the possible pairs of tilting angles on the same contour line map to the same value. Therefore, the intersection points between contour line of linewidth and contour line of normalized intensity indicate the solutions to the inverse problem. In other words, given linewidth and normalized intensity, the position of the intersection tells us what is the corresponding surface tilting angles. Hence, the inverse problem can be viewed as finding the coordinate of the intersection point of the contours.

One thing to note here is that there is actually ambiguity in the solution to the inverse problem, i.e. the inverse model does not have unique output. As can be seen in the figure, there are 2 intersecting points between the contours.

To further resolve this issue, the reconstructed 3D profile of the measured object has to be utilized. Note that the 3D profile is reconstructed row-by-row in an image, the tilting angle is also done the same way simultaneously. The ambiguity can be resolved by

doi:10.6342/NTU202400740

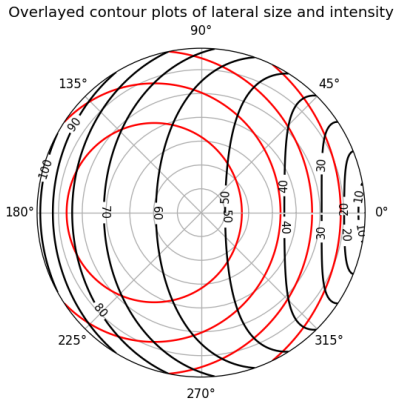

Figure 4.31 By overlapping contour maps, a grid-like pattern is produced. The coordinates of the intersection points is the answer to the inverse problem. (Red contour: intensity model; Black contour: linewidth model).

comparing the 3D coordinate of the points reconstructed from previous row and current row. The local slope tells us the approximate tilting orientation. However, the ambiguity of the tilting angle in first row cannot be resolved by this method.

Finding the coordinate of the intersection is not an computationally easy task. The problem lies in the nonlinearity of the contour lines. In this research, the proposed solution to this problem utilizes constrained optimization. Constrained optimization problems (COP) are the problems for which an objective function $f(x)$ is to be minimized or maximized subject to constraints $g(x)$. The constraints can be any combination of arbitrarily many equality constraints, $g(x) = 0$, and inequality constraints, $g(x) > 0$. One simple solution to COP for equality constraint is through the method of Lagrange multiplier.

To reformulate the inverse model as constrained optimization problem, we can write the objective function as the squared difference between the observed value of intensity I_0 and the output of the intensity forward model $f_2(\theta, \phi)$

$$f(\theta, \phi) = (I_0 - f_2(\theta, \phi))^2 \tag{4.25}$$

doi:10.6342/NTU202400740

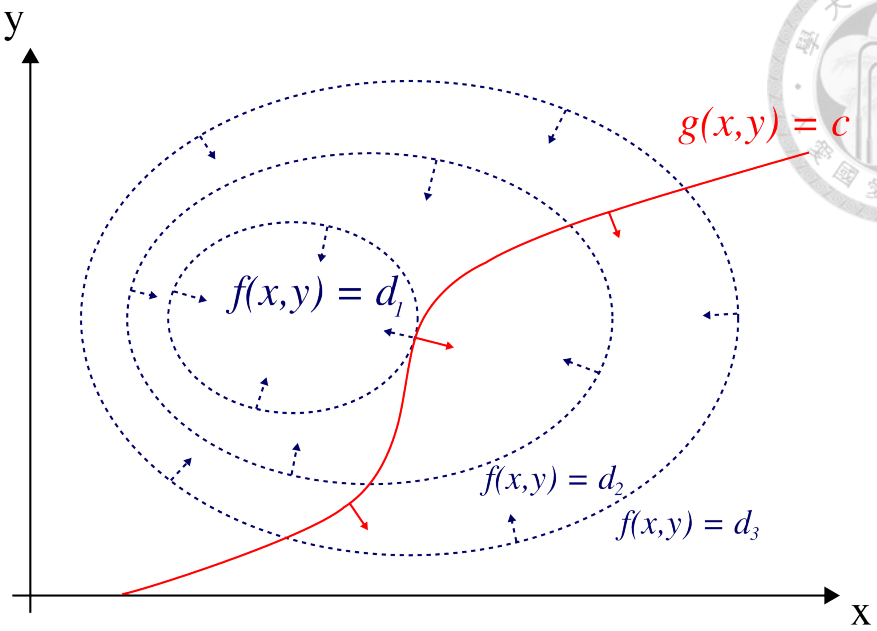

Figure 4.32 COP is a problem where the optimized value of the objective function (blue contours) must be found along the constraint (red curve) [35].

The equality constraint is the difference between the observed value of linewidth L_0 and the output of linewidth forward model $f_1(\theta, \phi)$

$$g(\theta, \phi) = L_0 - f_1(\theta, \phi) = 0 \tag{4.26}$$

In other words, the minimal value of the objective function occurs when $f_2(\theta, \phi) = I_0$ and $f_1(\theta, \phi) = L_0$. The corresponding values of tilting angles (θ^* and ϕ^*) indicate the exact value that yields the linewidth L_0 and intensity I_0.

$$[\theta^*, \phi^*]^\intercal = \arg\min_{[\theta,\phi]^\intercal} (I_0 - f_2(\theta, \phi))^2, \quad L_0 - f_1(\theta^*, \phi^*) = 0 \tag{4.27}$$

By interpreting inverse problem as constraint optimization problem, the tilting angles can be solved computationally. In practice, we implemented sequential least squares programming (SLSQP) in scipy to solve this problem. One just need to provide initial guesses for θ, ϕ and the forward models $f_1(\theta, \phi)$ and $f_2(\theta, \phi)$. Optionally, one can also

doi:10.6342/NTU202400740

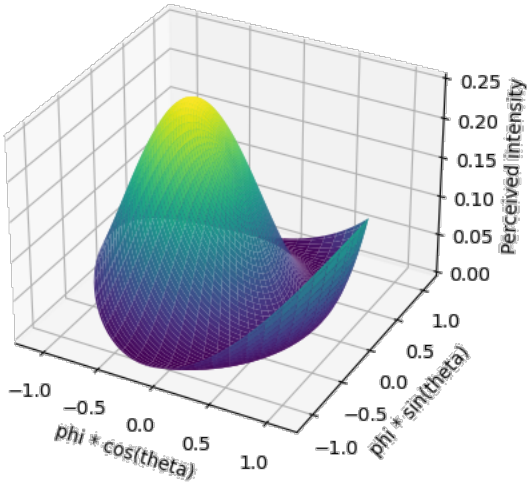

Figure 4.33 The 3D topography of the objective function resembles a terrain, with the minimum value situated in the valley of this landscape.

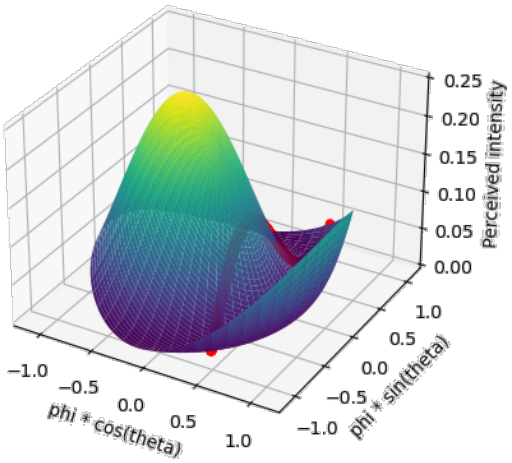

Figure 4.34 The 3D topography of the objective function with the constraint plotted in dots, showing the possible solution to the COP.

provide the first derivatives of the objective function and constraint, i.e. $\frac{\partial f}{\partial \theta}$, $\frac{\partial f}{\partial \phi}$, $\frac{\partial g}{\partial \theta}$ and $\frac{\partial g}{\partial \phi}$, s.t. the gradient at each evaluated step can be known and increase the efficiency of solving COPs.

doi:10.6342/NTU202400740

Chapter 5 Experiments and Discussions

This research encompasses two primary experiments: the validation of the forward model and the validation of the overall methodology. To assess the appropriateness of the forward models, an experiment must be devised. This experiment is done by taking sampling points in (θ, ϕ). The corresponding light intensity and spot size are measured and recorded. The obtained results are then compared with the 3D topography predicted by the forward models.

In demonstrating the overall effectiveness of the methodology, 3D printed objects are scanned, presenting the results in a point cloud. For quantitative results, angle blocks are scanned to compare predicted tilting angles with the ground truth, allowing for error evaluation.

5.1 Apparatus and procedure

The experiment validating the forward models involves measuring the linewidth and intensity of the light spot on objects at different tilting angles. To ensure the experiment's rigor, angle standard blocks are created and affixed to a rotational stage. These blocks fea-

doi:10.6342/NTU202400740

ture slanted faces resembling the cross-section of a cylinder and are produced through 3D printing. To eliminate layer lines on the slanted surface, the initial layer is printed on the slanted face, and the entire block is printed diagonally as shown in Fig. 5.1. Subsequently, the slanted face is sanded with 100-grit sandpaper to achieve a matte surface, aligning it more closely with the assumed conditions for Lambert's cosine law.

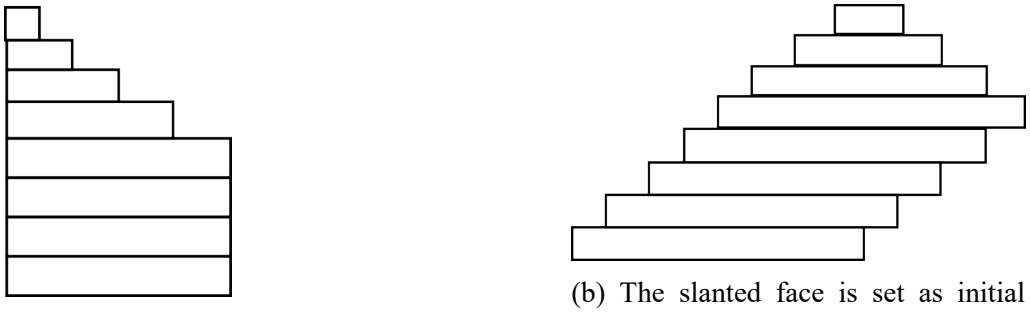

(a) original printing scheme.

(b) The slanted face is set as initial layer.

Figure 5.1 The surface of the slanted face becomes smoother using printing scheme (b).

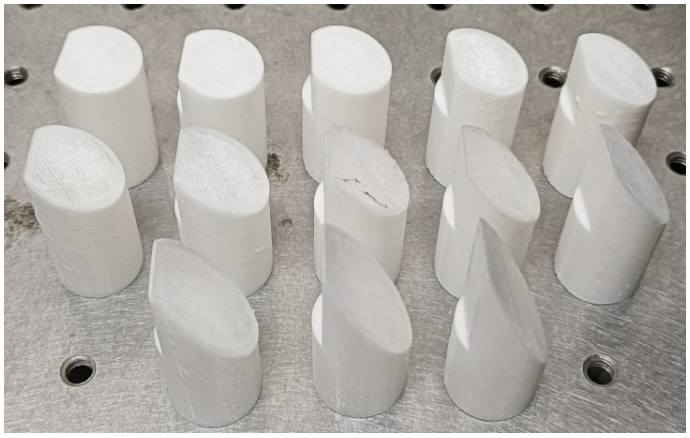

Figure 5.2 3D printed standard blocks.

Different angle standard blocks represent different zenith angles. Only the angles which are multiple of $5°$ are considered. Maximum zenith angle is $65°$. In total, there are 13 distinct standard blocks, and a $0°$ cylindrical block. Subsequently, these angle standard blocks are securely mounted on a rotary stage, governing the azimuth angle of their slanted faces. The azimuth angle is adjusted in increments of 5 degrees, ranging from $0°$ to $360°$.

For each tilting angle, an image is captured, featuring a light spot projected from the projecting subsystem. Originally designed for projecting line patterns, the subsystem is

doi:10.6342/NTU202400740

Figure 5.3 A 25° standard block mounted on the rotary stage.

adapted to project a light spot by covering the slit with opaque tape, leaving only the central portion exposed. A total of 937 images ($13 \times 72 + 1 = 937$) are captured, representing 937 sampled data points on the (θ, ϕ) space. These images are instrumental in verifying the accuracy of the forward models $f_1(\theta, \phi)$ and $f_2(\theta, \phi)$.

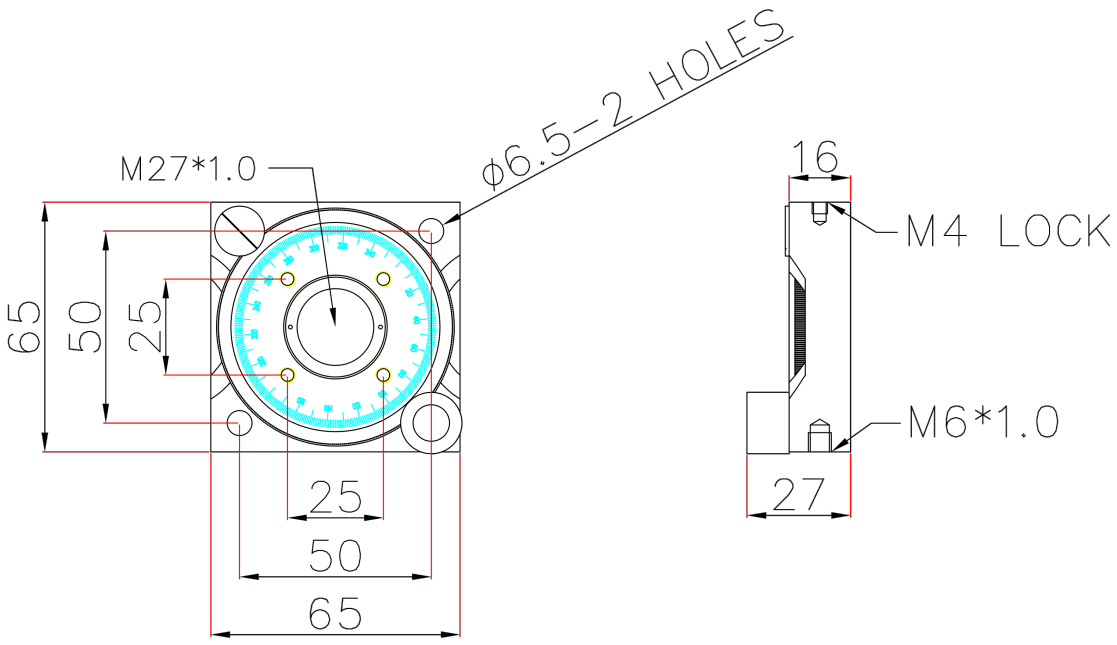

Figure 5.4 CAD drawing of the rotary stage [36].

The angular dimension tolerance is determined by the printing quality of the 3D printer. The 3D printer used to print the standard block is PING linkin Factory P300+.

doi:10.6342/NTU202400740

The main source of form error is caused by layer shifting, which is an error resulted from positional error of the nozzle. According to the specification provided in [37], the accuracy of the 3D printer is $0.05\ mm$. The printing layer height was chosen to be $0.4\ mm$. The angular dimension tolerance can be computed by considering the possible tilting of the 3D printed rod when the rod is fixed in the rotary stage Fig. 5.5. The red dashed line shows the limit position of the centerline caused by the printing error in worst case scenario. Note that the printing error is assumed independent for each layer, so there is no accumulated error.

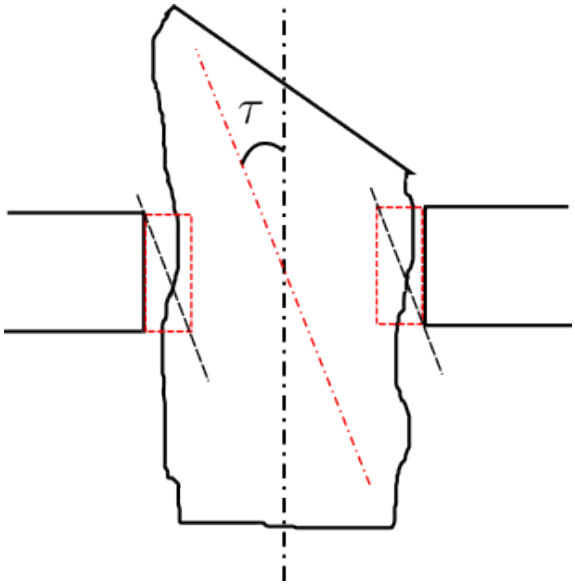

Figure 5.5 Illustrative plot for calculating angular tolerance of ϕ.

Note that the standard block is fixed inside the hole at the center of rotary stage. Thus, the orientation of the slanted surface can be affected by fitness between the standard block and the ring. As shown in the CAD plot Fig. 5.4, the depth of the hole is $16\ mm$. The accuracy of 3D printed rod is $0.05\ mm$. Thus, the tolerance is calculated as

$$\tau = \arctan\frac{0.05}{16} \approx 0.0031\ (rad) \approx 0.18\ (deg) \tag{5.1}$$

The value computed above only explains the tolerance of zenith angle. The tolerance of

doi:10.6342/NTU202400740

azimuth angle is larger since the minimum scale of the rotary stage is 1°. The tolerances for azimuth angle and zenith angle are provided in table below.

Table 5.1 Angular dimension tolerances.

	Zenith (ϕ)	**Azimuth** (θ)
Tolerance	$\pm 0.18\ (deg)$	$\pm 1\ (deg)$

5.2 Extraction of size and intensity

As discussed in chapter 4, the light spots are characterized by a bivariate normal distribution. Within a brief time interval, the incident photon flux reaching the camera sensor approximately follows bivariate normal distribution. This characteristic can be confirmed through the χ^2 goodness-of-fit test applied to each image. Consequently, a bivariate normal model is employed for fitting on each image to discern and extract both the size and intensity of the light spot.

In practice, to fit bivariate normal distribution onto the grayscale image, some modification on the distribution function should be done. The actual function being fitted is below:

$$f(x,y) = I_{bg} + \frac{I_{amp}}{2\pi\sigma_x\sigma_y\sqrt{1-\rho^2}} e^{-\frac{z}{2(1-\rho^2)}} \tag{5.2}$$

where z is defined as below

$$z \equiv \frac{(x-\mu_x)^2}{\sigma_x^2} - \frac{2\rho(x-\mu_x)(y-\mu_y)}{\sigma_x\sigma_y} + \frac{(y-\mu_y)^2}{\sigma_y^2} \tag{5.3}$$

I_{bg} is the background intensity or offset value of the distribution, and I_{amp} is the amplitude or the scale factor of the distribution. This way the value for $f(x,y)$ does not restricted in $[0,1]$.

doi:10.6342/NTU202400740

This is a parametric model with seven parameters that can be fitted to grayscale images using an optimization algorithm. Specifically, a non-linear least squares method is employed within a defined trusted-region in this research.

The optimal parameters $(I_{bg}, I_{amp}, \mu_x, \mu_y, \sigma_x, \sigma_y, \rho)$ extracted for each image encapsulate the characteristics of the light spot. The size of the light (L) spot can be determined from σ_x, where the horizontal standard deviation σ_x serves as an indicator of lateral size. Plugging σ_x into the FWHM formula (refer to (4.13) in chapter 4) allows us to extract the linewidth at that specific tilting angle.

$$L = 2\sqrt{2\ln 2}\sigma_x \tag{5.4}$$

On the other hand, the intensity of the light spot (I) is represented by the intensity value at (μ_x, μ_y), corresponding to the peak value of the function. It can be directly computed by the following formula

$$I = I_{bg} + \frac{I_{amp}}{2\pi\sigma_x\sigma_y\sqrt{1-\rho^2}} \tag{5.5}$$

The following images demonstrate some of the fitting results. These images are cropped since only the area around the light spot is considered. As can be seen in the fitted results, the contours of the bivariate normal function align with intensity distribution pretty well.

After bivariate normal function is fitted on every single image (937 images in total), the intensity and linewidth can be extracted for every tilting angle. The extracted linewidth and intensity results are visually presented below, following a similar format as depicted in Fig. 4.25 and Fig. 4.26. It is essential to note that for large zenith tilting angles, occlusion effects may arise, rendering the light spot unobservable. Consequently, the corresponding

doi:10.6342/NTU202400740

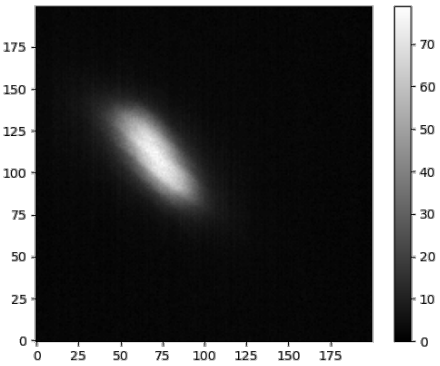

(a) Original image.

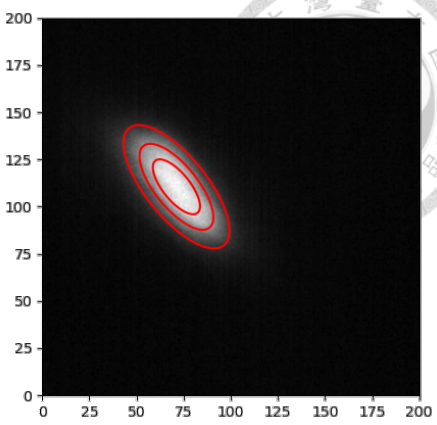

(b) Contours of fitted bivariate normal.

Figure 5.6 Light spot image and the fitted contours at $(\theta, \phi) = (280°, 45°)$.

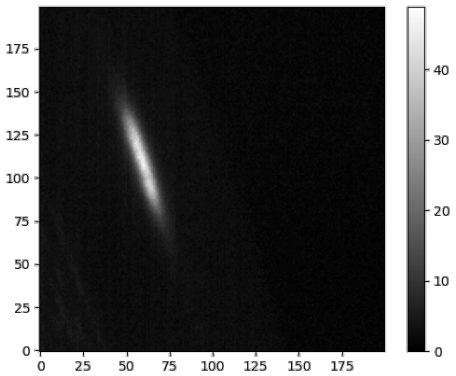

(a) Original image.

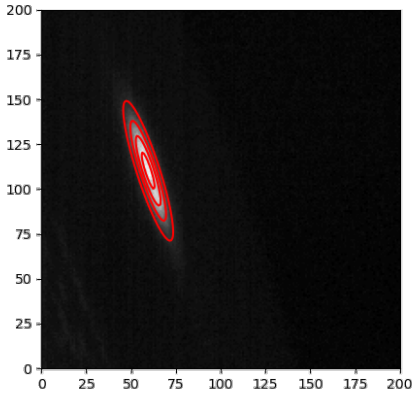

(b) Contours of fitted bivariate normal.

Figure 5.7 Light spot image and the fitted contours at $(\theta, \phi) = (335°, 55°)$.

data points for such instances are intentionally left blank in the visual representation.

As for images captured in scanning sequences, the linewidth and intensity are extracted in similar manner. However, since the images contains line patterns instead of spots, 1 dimensional Gaussian function is fitted on every row. The linewidth and intensity at every point on the line pattern are extracted by fitting a parametric model on the row-wise grayscale value. The Gaussian function being fitted is described below:

$$f(x) = I_{bg} + \frac{I_{amp}}{\sqrt{2\pi}\sigma_x} e^{-\frac{(x-\mu_x)^2}{2\sigma_x^2}} \tag{5.6}$$

doi:10.6342/NTU202400740

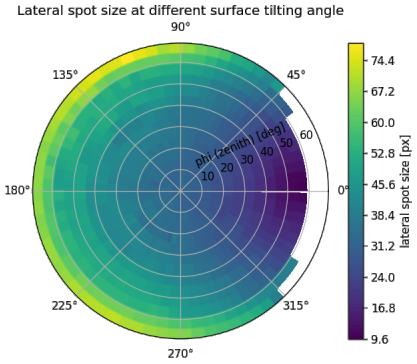

Figure 5.8 Extracted linewidth in color-coded map.

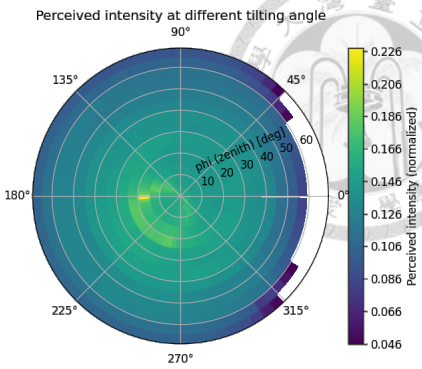

Figure 5.9 Extracted intensity in color-coded map.

The linewidth is again calculated by the formula

$$L = 2\sqrt{2\ln 2}\sigma_x \tag{5.7}$$

and the intensity is calculated by

$$I = I_{bg} + \frac{I_{amp}}{\sqrt{2\pi}\sigma_x} \tag{5.8}$$

Note that the value of μ_x here is also taken to be the position of the intersecting point of the projected light sheet and the object. Here are some fitted result for images of line pattern. Fig. 5.10 illustrates that the intensity profile within a row can be effectively represented by a normal distribution.

5.3 Validation and analysis

The experiments can be categorized into two main aspects. Firstly, the validation of forward models involves verifying the validity of assumptions made in the theoretical model. A thorough examination of every detail in the model is essential to draw the most reasonable and reliable conclusions. Statistical methods are employed to analyze the

doi:10.6342/NTU202400740

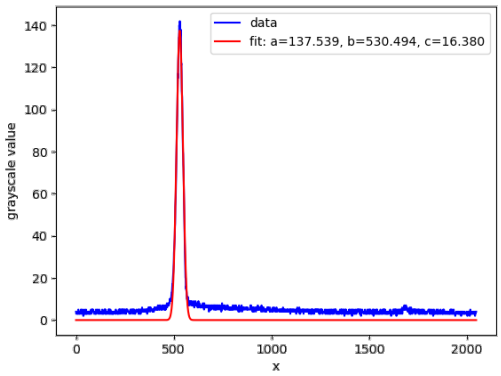

Figure 5.10 Fitting result of the grayscale value of a single row extracted from the line-pattern image. The symbols in the legend:a) amplitude I_{amp}, b) mean μ_x and c) standard deviation σ_x.

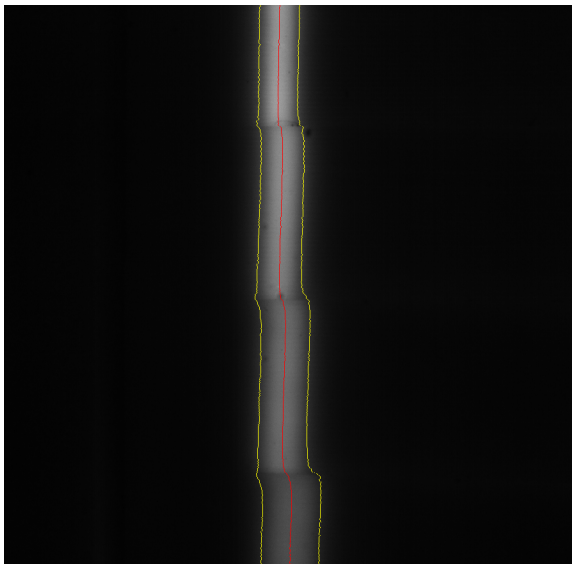

Figure 5.11 Fitting result of the grayscale value of every row in the line-pattern image. Red dots: position of the mean; Yellow dots: position of half maximum.

experimental data acquired in this phase.

The second experiment is centered around the validation of the overall methodology by means of scanning 3D printed objects. The analysis in this phase is more qualitative than quantitative; nonetheless, the error of the estimated tilting angles is evaluated.

doi:10.6342/NTU202400740

5.3.1 Validation of forward models

The derivation of the theoretical model relies on a fundamental assumption: "the light spot follows a bivariate normal distribution." To empirically verify if the captured image of a light spot adheres to a bivariate normal distribution, a χ^2 goodness-of-fit test is employed on the grayscale image. The statement, "the light spot follows a bivariate normal", is the null hypothesis. The χ^2 statistics is calculated as follows [38]:

$$\chi^2 = \sum_{i=1}^{N} \frac{(O_i - E_i)^2}{E_i} \tag{5.9}$$

Here, O_i represents the observed count for bin i, corresponding to the grayscale value of the i-th pixel in the rearranged 1D array of the original image. E_i is the expected grayscale value at the i-th pixel.

The image size is originally 2048×2048, which is too large for data fitting. Therefore, only the area around the light spot is taken to be the region of interest (ROI). The ROI is 200×200 in size. The pixels are rearranged that such that the original image is transformed into a 1D array. Recall that degree of freedom (DoF) for this test is calculated by the total number of bins minus the number of estimated parameters. The total number of pixels within the ROI minus 7 is the degree of freedom (DoF) for this test given that there are 7 parameters $(I_{bg}, I_{amp}, \mu_x, \mu_y, \sigma_x, \sigma_y, \rho)$ to be determined.

$$\text{DoF} = 200^2 - 7 = 39993 \tag{5.10}$$

By plugging in the degree of freedom and the predetermined p-value into a calculator such as Excel, the critical value for the test can be computed. The p-value is chosen to be

doi:10.6342/NTU202400740

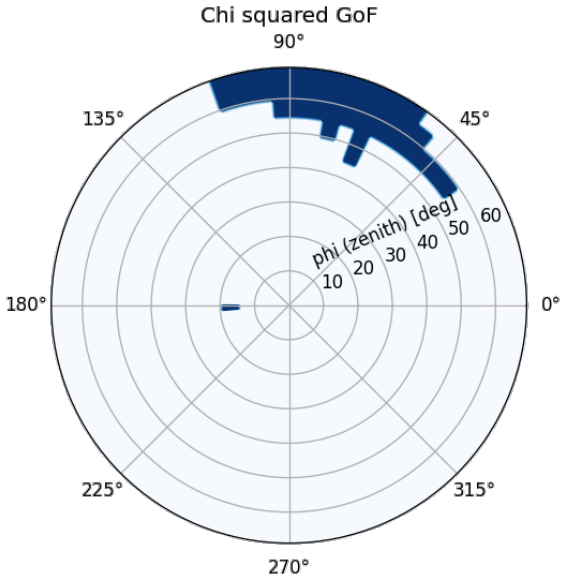

Figure 5.12 χ^2 goodness-of-fit test, rejected sample data. Null hypothesis is rejected in blue regions.

0.05.

$$\chi^2_{1-0.05,39993} \approx 40459.3284 \tag{5.11}$$

If the χ^2 value is higher than this critical value, it can be concluded that the light spot does not follow bivariate normal distribution well, and the null hypothesis is rejected. In Fig. 5.12, each of the 937 light spots is subjected to the χ^2 goodness-of-fit test, where the critical value of the test is 40459.3284. The outcomes of these tests reveal whether the light spots conform to the assumed distribution, namely, a bivariate normal distribution. The blue regions highlight instances where the null hypothesis is rejected, signifying that the light spot at a particular tilting angle deviates from the bivariate normal distribution assumption. This results in approximately 96.13% of the data being considered reliable.

The result presented in Fig. 5.8 and Fig. 5.9 demonstrate noticeable similarities between the observations and the model. The overall trends in the distributions align closely. However, for a more quantitative assessment of the agreement between the results and the model, statistical indicators should be employed.

doi:10.6342/NTU202400740

For both forward models, the R^2 statistics is utilized as an indicator of goodness-of-fit. The sampled data points for each selected (θ, ϕ) pair are utilized as bins. Recall that R^2 is calculated as below

$$R^2 = 1 - \frac{SS_{\text{res}}}{SS_{\text{tot}}} \tag{5.12}$$

where SS_{res} is called residual sum of squares, and SS_{tot} is called total sum of squares

$$SS_{\text{res}} = \sum_{i=1}^{n} (y_i - \hat{y}_i)^2 \tag{5.13}$$

$$SS_{\text{tot}} = \sum_{i=1}^{n} (y_i - \bar{y})^2 \tag{5.14}$$

$$\bar{y} = \frac{1}{n} \sum_{i=1}^{n} y_i \tag{5.15}$$

Here y_i represents observed light spot size or intensity. $\hat{y}_i$ is the output value of the forward model at the corresponding position. In ANOVA and regression analysis, total sum of squares and residual sum of squares are related by the following eqaution

$$SS_{\text{tot}} = SS_{\text{res}} + SS_{\text{reg}} \tag{5.16}$$

where SS_{reg} is called regression sum of squares or explained sum of squares. Since sum of squares must be larger than 0, $SS_{\text{res}} < SS_{\text{tot}}$. Thus, R^2 statistics can only be a real number between 0 and 1. For R^2 implying that the model is perfectly fitted with the data points. However, it can also imply that the model is overfitted with the data. The R^2 statistics for the linewidth model and intensity model are provided in the table below.

Table 5.2 R^2 statistics of forward models.

	Linewidth forward model	**Intensity forward model**
R^2	0.644	0.016

The R^2 analysis indicates a robust performance of the linewidth forward model, cap-

doi:10.6342/NTU202400740

turing a significant portion of the data variation, despite some residual errors. Conversely, the intensity model exhibits a lower R^2 value, suggesting a less accurate alignment with the observed data variation. The value of R^2 being in the proximity of 0 implies that the intensity model performs only marginally better than predicting the sample mean value.

5.3.2 Validation of overall methodology

Figure 5.13 Sample object (Material: SUS304).

This section shows the overall result of the methodology. It can be divided into measurement of 3D coordinates and measurements of tilting angles. Point cloud of the scanning results are shown below. The position of the points indicates their relative location in CCS. The result of tilting angle measurement is also provided in the format of point cloud but with a different color scheme.

The result of tilting angles measurement are also provided in the figure below. The sample in this scanning sequence is the angle standard block $(\theta, \phi) = (140°, 20°)$

To quantitatively analyze the performance of angle reconstruction, cosine similarity is introduced here. The cosine similarity (sim) is a metric that evaluates the difference

doi:10.6342/NTU202400740

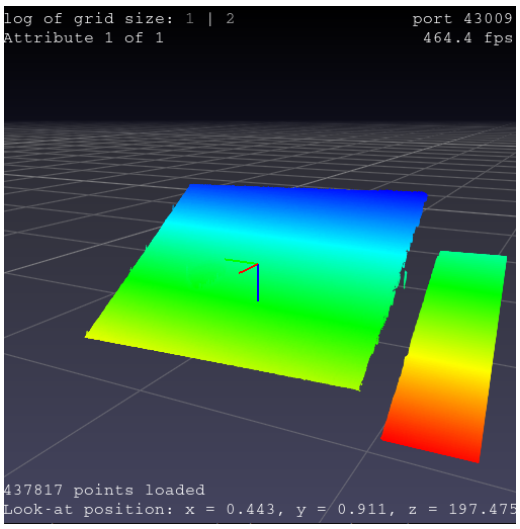

Figure 5.14 Scanned point cloud of Fig. 5.13, color-coded by z_c value.

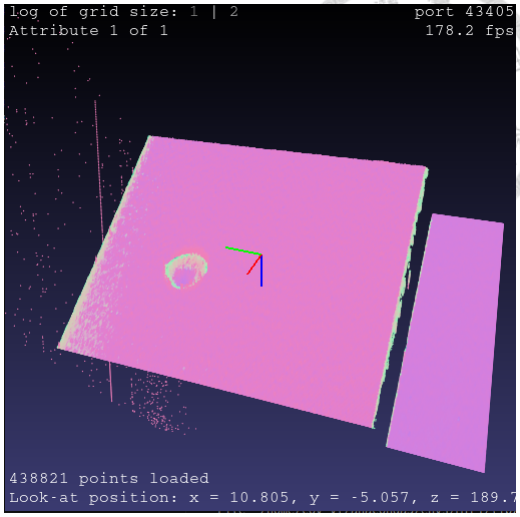

Figure 5.15 Scanned point cloud of Fig. 5.13, color-coded by tilting angle.

between 2 vectors, $\mathbf{n}_1$ and $\mathbf{n}_2$. In fact, it calculates the angle η between 2 vectors, $\mathbf{n}_1$ and $\mathbf{n}_2$. It can be calculated by the formula below.

$$\text{sim} = \cos\eta = \frac{\mathbf{n}_1 \cdot \mathbf{n}_2}{||\mathbf{n}_1||\ ||\mathbf{n}_2||} \tag{5.17}$$

Notice that the value for cosine similarity is the range of $\cos(\cdot)$, which is $[-1, 1]$. If the predicted surface normal vector is perfectly aligned with ground truth normal vector, and the vectors are pointing the same direction, the cosine similarity would be 1.

The angles of the standard block are viewed as ground truth. Using (4.19), the normal vector of the slanted surface can be calculated. There are about 65k points in the point cloud of the slanted surface in Fig. 5.17. Each point carries information about the tilting angle. To evaluate the accuracy of the point cloud, cosine similarity is implemented. The evaluation is shown in the table below.

Table 5.3 Cosine similarity between measured and ground truth surface normals.

	Maximum	Average
sim	0.533	0.345

doi:10.6342/NTU202400740

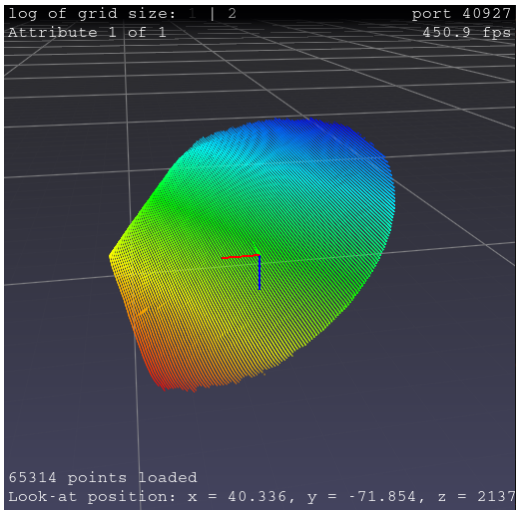

Figure 5.16 Scanned point cloud of $\theta = 140°$, $\phi = 20°$ standard block, color-coded by z_c value.

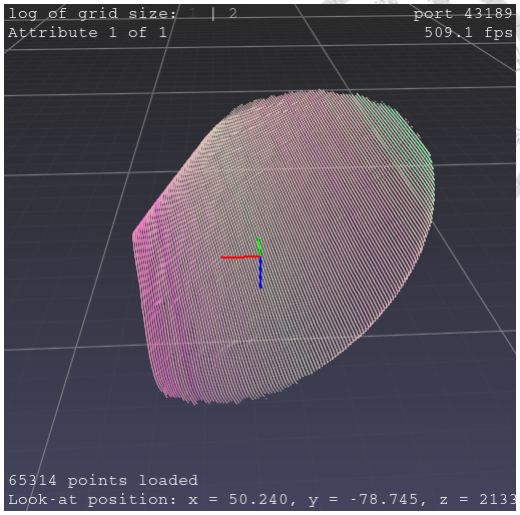

Figure 5.17 Scanned point cloud of $\theta = 140°$, $\phi = 20°$ standard block, color-coded by tilting angle.

The findings suggest that there is potential for enhancement in the precision of angle measurements. The most accurate match for the surface normal demonstrates a cosine similarity of 0.533, indicating that the normal vector is approximately 60 degrees divergent from the ground truth.

It is speculated that the substantial deviation may stem from the limited accuracy of the forward model. The R^2 value for the intensity forward model indicates that the observed light spots deviate significantly from Lambert's cosine law. To enhance the accuracy of angle measurements, adjustments to the intensity forward model are anticipated. By refining the model to achieve an R^2 comparable to that of the linewidth model, improvements in angle measurement accuracy are expected.

The 3D coordinate measurement is further validated by scanning the spheres on the standard block as shown in the Fig. 5.18. The coordinates of the center of the balls are the points of interests. There are 10 spheres in total, and they are labeled from 1 to 10 as shown.

doi:10.6342/NTU202400740

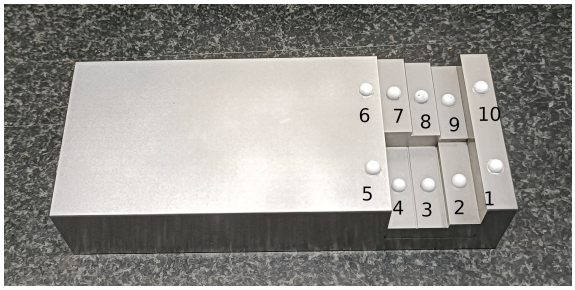

Figure 5.18 The standard block with balls attached on the surface.

The standard block is placed on the rotation stage and scanned by the system. Scanned profiles are obtained when the zenith tilting angle are 0 degree and 20 degree. The point cloud of the scanning results are shown in Fig. 5.20. As can be seen, the surface of each step of the standard block are shown in different color, indicating that the proposed system can distinguish the height difference between the surfaces. Moreover, the balls on the surface can also be identified.

The center coordinate and the radius of the balls are obtained through random sampling consensus which is robust to outliers, in comparison with least square methods. To find the center coordinates and the radius, the point clouds are manually extracted from the original point cloud and the random sampling operation is performed. The remaining point cloud is shown in Fig. 5.21 and Fig. 5.22. The color of the points represents the z_c value of the coordinates. The final results are compared with the measurement results of CMM.

The standard block is placed onto the platform of CMM for measurement as shown in Fig. 5.23. CMM takes 5 sample points for each sphere. All 10 spheres are measured 10 times. The user interface in Fig. 5.24 illustrates the relative positions of each ball on the standard block. CMM takes 5 sample points for each sphere. The coordinates of the center and the radius are obtained through least square circle. The measurement data obtained through CMM is taken as ground truth. The bias of the proposed system are calculated by

doi:10.6342/NTU202400740

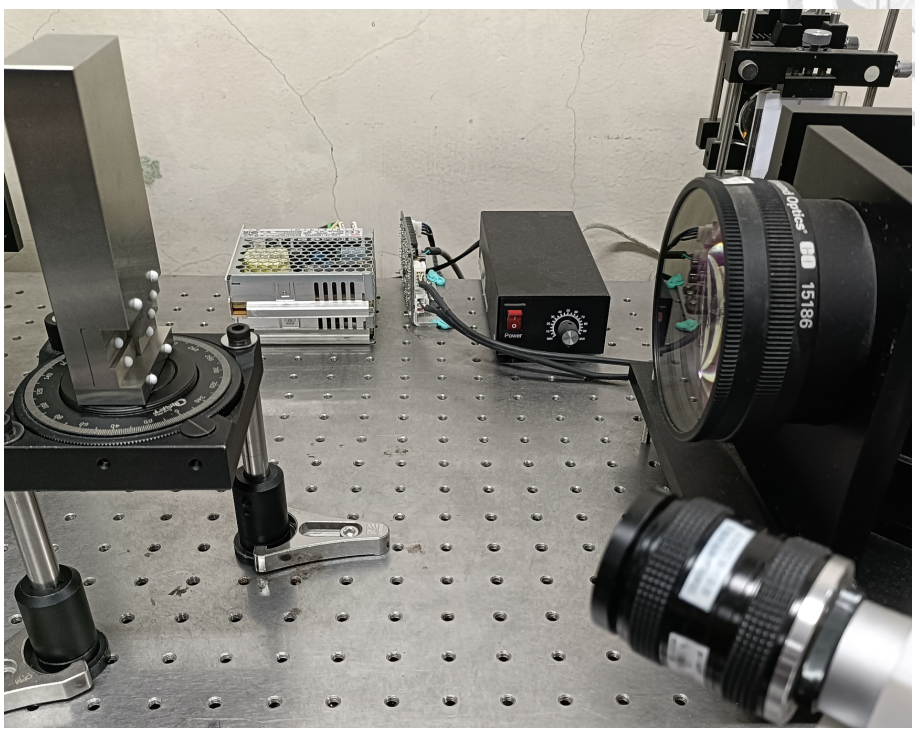

Figure 5.19 The standard block is placed on a rotation stage to control the zenith tilting angle.

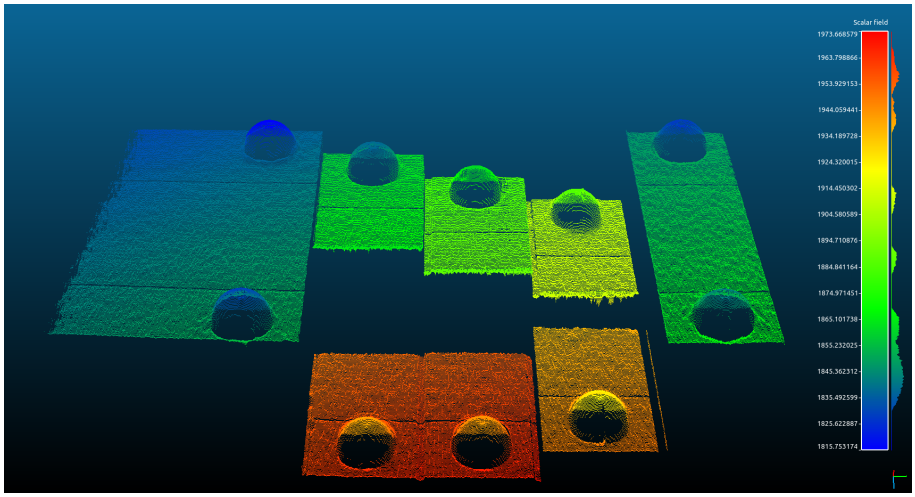

Figure 5.20 Scanned profile of the standard block.

doi:10.6342/NTU202400740

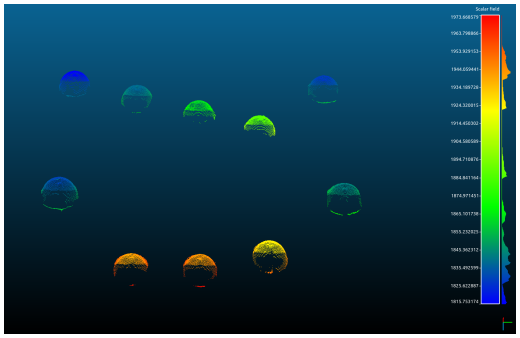

Figure 5.21 Extracted point cloud of the balls at $\phi = 0°$.

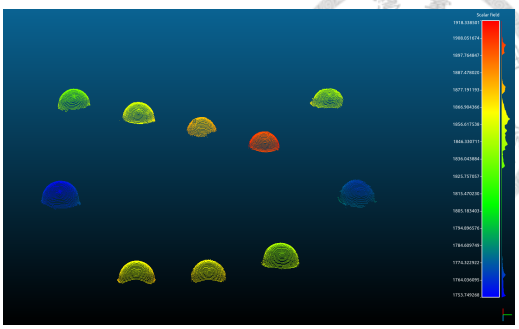

Figure 5.22 Extracted point cloud of the balls at $\phi = 20°$.

comparing with ground truth. Since the CMM defines the coordinate system differently, the critical dimension of the standard block must be considered. The critical dimensions are defined by the distance between each ball and the angle formed by 3 consecutive balls. Only relative positions of the centers are considered. The angle between formed by 3 consecutive ball centers is also invariant under rotation. The angles are also measured and compared with the ground truth obtained by CMM.

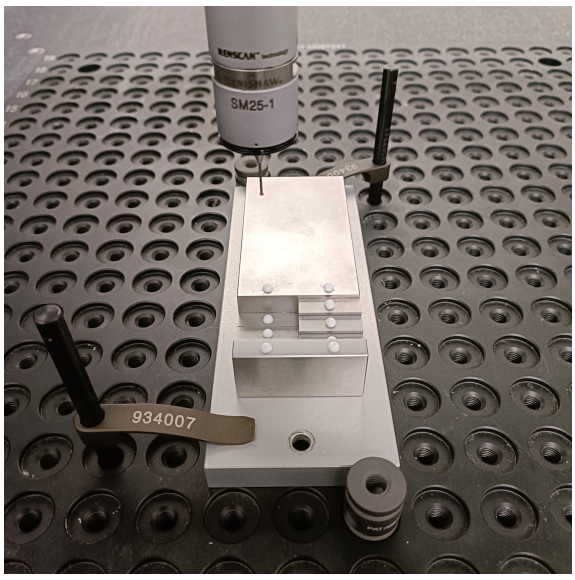

Figure 5.23 Actual image of the standard block on the CMM.

doi:10.6342/NTU202400740

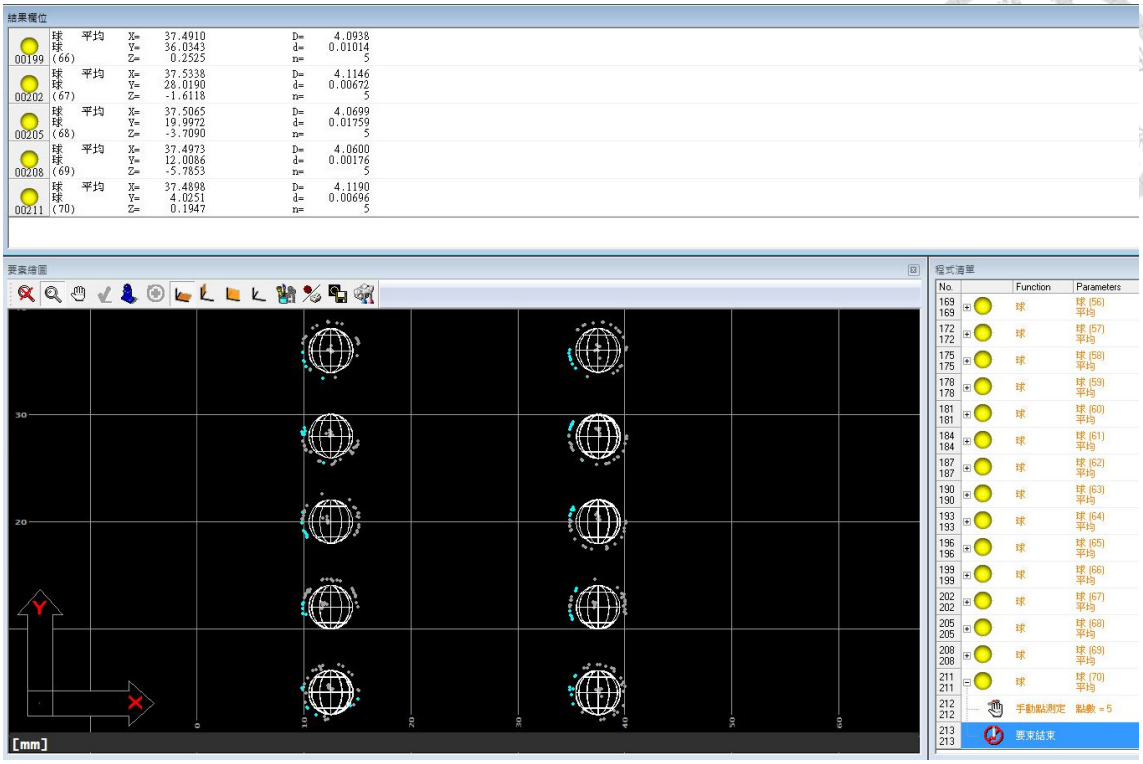

Figure 5.24 User interface of the Mitutoyo CMM.

The bias between the measurement from our system and measurement from CMM is shown in Table 5.4. For precision metrology, this amount of bias is abnormal. One of causes to this phenomenon is the erroneous 3D coordinates of reconstructed point cloud of the spheres (Fig. 5.25, and Fig. 5.26). As can be seen, the reconstructed surface appears to be dented while the actual ball does not have this property. Also, the point cloud near the bottom of the sphere is also distorted, the points flare outwards. Further discussion on this will be provided later.

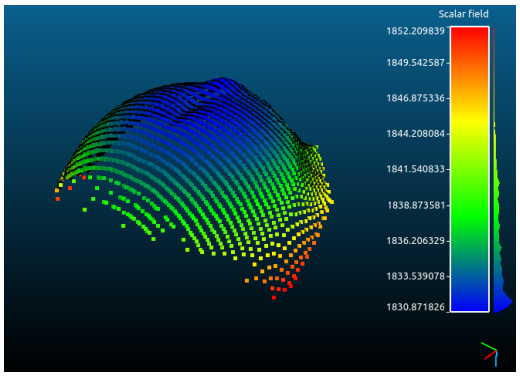

Figure 5.25 Close-up surface profile of ball 6 at $\phi = 20°$.

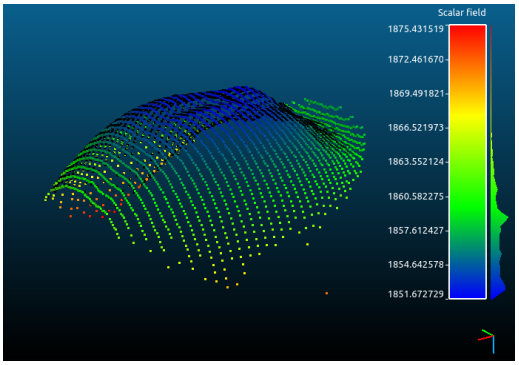

Figure 5.26 Close-up surface profile of ball 7 at $\phi = 20°$.

doi:10.6342/NTU202400740

Table 5.4 Diameter of the balls (unit: mm)

		Proposed system		Bias	
Index	CMM	$\phi = 0°$	$\phi = 20°$	$\phi = 0°$	$\phi = 20°$
Ball 1	4.11702	3.85142	4.03654	-0.26560	-0.08048
Ball 2	4.06867	3.99988	3.88054	-0.06879	-0.18813
Ball 3	4.06757	3.89474	3.94118	-0.17283	-0.12639
Ball 4	4.07665	3.83500	3.96388	-0.24165	-0.11277
Ball 5	4.11645	3.93296	3.98374	-0.18349	-0.13271
Ball 6	4.10049	3.93310	4.65872	-0.16739	0.55823
Ball 7	4.05760	3.93164	5.31860	-0.12596	1.26100
Ball 8	4.10278	3.8629	3.93122	-0.23988	-0.17156
Ball 9	4.06148	4.51498	3.98330	0.45350	-0.07818
Ball 10	4.12159	3.97236	4.24750	-0.14923	0.12591

The measurement results of critical dimensions of the standard block are provided below. The distance between 2 consecutive balls are calculated by computing the differences of the coordinates in CCS. This value is compared with the ground truth measured from CMM. The results are shown in Table 5.6.

The angular critical dimension is computed by considering 3 consecutive balls and computing the vectors between the centers, i.e. the coordinate differences. The vectors are listed in Table 5.5. They are directly calculated from the fitted coordinates of the center. The cosine angle between 2 vectors can be computed as dividing the inner product by the product of the vector lengths.

Table 5.5 Coordinate differences between consecutive balls (unit: mm)

	$\phi = 0°$			$\phi = 20°$		
Vector index	Δx_c	Δy_c	Δz_c	Δx_c	Δy_c	Δz_c
Ball 1 to Ball 2	0.39237	-8.24680	8.08201	-2.33754	-8.15230	7.44418
Ball 2 to Ball 3	-0.12439	-8.05813	1.81446	-0.79569	-8.07763	1.79597
Ball 3 to Ball 4	-0.16642	-8.06607	-0.25126	-0.264580	-8.03949	-0.23180
Ball 4 to Ball 5	-0.95914	-7.75186	-10.84132	2.62056	-7.7667	-10.23818
Ball 6 to Ball 7	0.31024	7.98721	2.1534	-0.41680	8.00715	2.45329
Ball 7 to Ball 8	0.29131	7.96409	2.35641	-0.20391	7.92605	1.61162
Ball 8 to Ball 9	0.26439	7.95119	2.72730	-0.71337	7.99195	2.28675
Ball 9 to Ball 10	0.12429	8.22343	-6.02839	2.21915	8.10937	-5.28185

doi:10.6342/NTU202400740

Table 5.6 Critical dimensions between consecutive balls (unit: mm)

		Proposed system		Bias	
Dimension	CMM	$\phi = 0°$	$\phi = 20°$	$\phi = 0°$	$\phi = 20°$
Ball 1 to Ball 2	11.14189	11.55346	11.28450	0.41158	0.14261
Ball 2 to Ball 3	8.24881	8.26082	8.31305	0.01202	0.06424
Ball 3 to Ball 4	7.99317	8.07170	8.04718	0.07853	0.05401
Ball 4 to Ball 5	12.82434	13.36209	13.11523	0.53776	0.29089
Ball 6 to Ball 7	8.26571	8.27822	8.38491	0.01251	0.11920
Ball 7 to Ball 8	8.24693	8.31049	8.09081	0.06357	-0.15612
Ball 8 to Ball 9	8.25294	8.41008	8.34322	0.15714	0.09028
Ball 9 to Ball 10	9.98384	10.19714	9.92897	0.21331	-0.05487

Table 5.7 The angles formed by the centers of the balls (unit: deg)

		Proposed system		Bias	
Angle index	CMM	$\phi = 0°$	$\phi = 20°$	$\phi = 0°$	$\phi = 20°$
1-2-3	30.00813	31.85152	30.19469	1.84339	0.18656
2-3-4	13.63815	14.47510	14.60748	0.83695	0.96933
3-4-5	52.05317	52.66532	52.58816	0.61215	0.53499
6-7-8	2.27829	1.39986	5.71247	-0.87843	3.43418
7-8-9	0.67265	2.45724	5.65042	1.78459	4.97777
8-9-10	51.24396	55.17236	51.87071	3.92840	0.62676

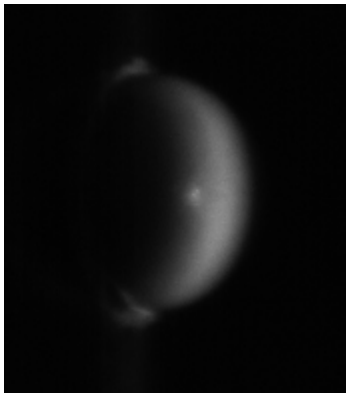

Figure 5.27 A bright light spot on the spherical surface of ball 6 can be observed.

As mentioned earlier the radius of the balls have large bias. Also, the critical dimensions have large error, too. The possible cause for these is bad reconstruction of 3D coordinate points. These anomalies likely stem from the algorithm used to extract centerlines from reflected line patterns. The original image (Fig. 5.27) reveals that the reflected light on the top of the sphere exhibits abnormal shapes in specific regions. This inconsistency contradicts with the assumption that ”row-wise grayscale values follow a Gaussian

doi:10.6342/NTU202400740

distribution.”

Furthermore, the point cloud flaring outwards is probably due to the geometrical constraint of the system. The figures below (Fig. 5.28 and Fig. 5.29) illustrate the fact that the light pattern can be obstructed by the geometry of the surface. The actual center line of the light pattern does not exist on the visible side of the ball. In fact, the center line is occluded by the topography of the object itself. The center line extraction algorithm cannot detect the line pattern lying on the other side of the ball. Still, the algorithm reconstructs the center line from the visible light pattern. Therefore, false coordinates of the points are reconstructed, causing large measuring bias of the ball radius and critical dimension.

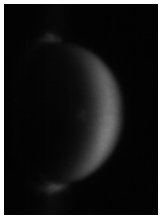

Figure 5.28 235-th image of the scanning sequence of ball 7.

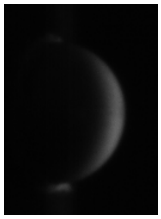

Figure 5.29 239-th image of the scanning sequence of ball 7.

doi:10.6342/NTU202400740

Chapter 6 Conclusions and Future Works

6.1 Conclusions

Surface tilting is an issue in reconstructing the profile of an object. Conventionally, people use neighboring points to estimate the tilting angle at that local area. However, this method would make tilting angle measurement dependent on coordinate measurement. This implies that the measurement error can propagate to tilting angle from coordinate error. Therefore, a novel method is proposed in this research to decouple the relationship between surface tilting and surface profile.

The methodology separates the measurement of tilting angle from measurement of 3D coordinates by designing a new mathematical model explaining the relationship between tilting angle and other physical quantities. The model is derived through rigorous theoretical deduction, and validated through experiments. There are two forward models to be specific. The first one is the linewidth as a function of tilting angles and the second is the intensity as a function of tilting angles.

These two models are combined together and further analyzed. It is found that every

doi:10.6342/NTU202400740

tilting angles corresponds to a specific pair of linewidth and intensity. Therefore, given the linewidth and intensity of the light patterns, one can find its corresponding tilting angles, and the inverse problem arises. The solutions to the inverse problem are the tilting angles corresponding to the given linewidth and intensity. The inverse problem is reformulated as constrained optimization problem (COP). By performing optimization algorithm with observed linewidth and intensity values as constraints, the underlying tilting angles can be deduced. Although the intensity forward model still needs some modification in the future, the overall performance of this inverse model reaches 0.533 cosine similarity with the ground truth for angular measurement. This methodology can be applied to similar hardware. As long as the system consists of a line light projector and an imaging system, this method can utilized.

After validating through experiments, it has been found out that there is still room for improvements for this methodology. Scanned point cloud of a standard block is analyzed and the critical dimensions are extracted. The results are compared with the ground truth measured from CMM. The bias is as large as 0.5 mm in length measurement. The cause to this bias is discussed. It is concluded that the algorithm of center line extraction is incapable of reconstructing true position of the center line. Also, the light patterns on the measured object do not always follow the presumed condition, i.e. Gaussian distribution, thereby inducing bad reconstructed results.

6.2 Future works

In the future, there are some points that can be tackled with to enhance the performance of the tilting angle measurement. First, consider more parameters in the imaging

doi:10.6342/NTU202400740

system. The lack of fitness in intensity forward model is highly likely caused by the gamma value of the camera, since gamma can affect the grayscale response of the image. Second, the calibration results should not be taken as parameters for forward models. As can be seen in the R^2 statistics, the models using calibrated parameters does not fit well. On the other hand, one can try use the forward model as a training model, and take the 937 images as training dataset. This way the best fitted model can be obtained, thereby raise the R^2 statistics. Hardware-wise, improvements can be made by consider following points. Although these are minor issues, they still worth mentioning. First, consider telecentric error in f-θ lens and the aberration in objective lens. Small deviation in these physical object can affect alot in theory. If the telecentric error is not negligible, the light sheets can not be considered as parallel in each image. If the distortion of the objective lens is not negligible, the light sheet in each image cannot be seen as a flat plane. Last but not least, the linewidth of the line projector can be shrunken by implementing Powell lens. This way, the accuracy of the profile reconstruction can be improved.

doi:10.6342/NTU202400740

References

[1] K. B. Smith and Y. F. Zheng. Accuracy Analysis of Point Laser Triangulation Probes Using Simulation. Journal of Manufacturing Science and Engineering, 120(4):736–745, 11 1998. ISSN 1087-1357. doi: 10.1115/1.2830214. URL https://doi.org/10.1115/1.2830214.

[2] F. Xi, Y. Liu, and H. Y. Feng. Error compensation for three-dimensional line laser scanning data. The International Journal of Advanced Manufacturing Technology, 18, 2001. ISSN 1433-3015. doi: https://doi.org/10.1007/s001700170076.

[3] S. V. Mikhlyaev. Influence of a tilt of mirror surface on the measurement accuracy of laser triangulation rangefinder. Journal of Physics: Conference Series, 48(1):739, oct 2006. doi: 10.1088/1742-6596/48/1/140. URL https://dx.doi.org/10.1088/1742-6596/48/1/140.

[4] N. Vukašinović, M. Korošec, and J. Duhovnik. The influence of surface topology on the accuracy of laser triangulation scanning results. Strojniški vestnik - Journal of Mechanical Engineering, 56(1):23–30, 2010. ISSN 0039-2480.

[5] S. Li, Y. Yang, X. Jia, and M. Chen. The impact and compensation of tilt factors upon the surface measurement error. Optik, 127(18):7367–7373, 2016. ISSN

doi:10.6342/NTU202400740

0030-4026. doi: https://doi.org/10.1016/j.ijleo.2016.05.004. URL https://www.sciencedirect.com/science/article/pii/S0030402616304326.

[6] Mitutoyo Corporation. CMM CRYSTA-Apex V. https://www.mitutoyo.com.tw/uploads/product/tw/cmm.png, 2023. Accessed: 2023-10-15.

[7] S. Van der Jeught and J. Dirckx. Real-time structured light profilometry: a review. Optics and Lasers in Engineering, 87:18–31, 2016. ISSN 0143-8166. doi: https://doi.org/10.1016/j.optlaseng.2016.01.011. Digital optical and Imaging methods in structural mechanics.

[8] C. Zuo, L. Huang, M. Zhang, Q. Chen, and A. Asundi. Temporal phase unwrapping algorithms for fringe projection profilometry: A comparative review. Optics and Lasers in Engineering, 85:84–103, 2016. ISSN 0143-8166. doi: https://doi.org/10.1016/j.optlaseng.2016.04.022. URL https://www.sciencedirect.com/science/article/pii/S0143816616300653.

[9] C. E. Towers, D. P. Towers, and J. D. C. Jones. Optimum frequency selection in multifrequency interferometry. Opt. Lett., 28(11):887–889, Jun 2003. doi: 10.1364/OL.28.000887. URL https://opg.optica.org/ol/abstract.cfm?URI=ol-28-11-887.

[10] P. Jia, J. Kofman, and C. English. Comparison of linear and nonlinear calibration methods for phase-measuring profilometry. Optical Engineering - OPT ENG, 46, 04 2007. doi: 10.1117/1.2721025.

[11] M. Takeda and K. Mutoh. Fourier transform profilometry for the automatic measurement of 3-d object shapes. Appl. Opt., 22(24):3977–3982, Dec 1983. doi:

doi:10.6342/NTU202400740

10.1364/AO.22.003977. URL https://opg.optica.org/ao/abstract.cfm?URI=ao-22-24-3977.

[12] G. E. Spoorthi, S. Gorthi, and R. K. Gorthi. Phasenet: A deep convolutional neural network for two-dimensional phase unwrapping. IEEE Signal Processing Letters, 26(1):54–58, 2019. doi: 10.1109/LSP.2018.2879184.

[13] W. Yin, Q. Chen, S. Feng, T. Tao, L. Huang, M. Trusiak, A.Asundi, and C. Zuo. Temporal phase unwrapping using deep learning, 2019.

[14] Z. Zhang, J. Qian, Y. Wang, and X. Yang. Phase unwrapping via deep learning based region segmentation. In IGARSS 2020 - 2020 IEEE International Geoscience and Remote Sensing Symposium, pages 397–400, 2020. doi: 10.1109/IGARSS39084.2020.9323569.

[15] C. A. Wiley. Synthetic aperture radars. IEEE Transactions on Aerospace and Electronic Systems, AES-21(3):440–443, 1985. doi: 10.1109/TAES.1985.310578.

[16] 邱亮學. 多頻率相移法絕對形貌量測術之不確定度分析與優化研究. Master's thesis, 國立臺灣大學, 01 2020.

[17] A. Donges and R. Noll. Laser Triangulation, pages 247–278. Springer Berlin Heidelberg, Berlin, Heidelberg, 2015. ISBN 978-3-662-43634-9. doi: 10.1007/978-3-662-43634-9_10. URL https://doi.org/10.1007/978-3-662-43634-9_10.

[18] W. H. Stevenson. Use of laser triangulation probes in coordinate measuring machines for part tolerance inspection and reverse engineering. In Other Conferences, 1993. URL https://api.semanticscholar.org/CorpusID:109338911.

doi:10.6342/NTU202400740

[19] T. Giesko, A. Zbrowski, and P. Czajka. Laser profilometers for surface inspection and profile measurement. Problemy Eksploatacji/Maintenance Problems, 1, 01 2007.

[20] Teledyne e2v CMOS Image Sensors. Laser Triangulation - How Does Laser Triangulation Work? https://imaging.teledyne-e2v.com/content/uploads/2021/05/3D-Sensor-illustrations-02-scaled.jpg, 2023. Accessed: 2023-10-17.

[21] R. Woodham. Photometric method for determining surface orientation from multiple images. Optical Engineering, 19, 01 1992. doi: 10.1117/12.7972479.

[22] Meekohi. Explanatory diagram of photometric stereo. Multiple images of an object under different lighting are analyzed to produce an estimated normal direction at each pixel. https://upload.wikimedia.org/wikipedia/commons/b/b5/Photometric_stereo.png, 2015. Accessed: 2023-10-15.

[23] X. Wang, D. F. Fouhey, and A. Gupta. Designing deep networks for surface normal estimation. CoRR, abs/1411.4958, 2014. URL http://arxiv.org/abs/1411.4958.

[24] J. E. Lenssen, C. Osendorfer, and J. Masci. Differentiable iterative surface normal estimation. CoRR, abs/1904.07172, 2019. URL http://arxiv.org/abs/1904.07172.

[25] M. W. van Veen. Normal map prediction from light field data through deep learning, February 2020. URL http://essay.utwente.nl/81519/.

[26] L. da Vinci. First published picture of camera obscura in Gemma Frisius' 1545 book De Radio Astronomica et Geometrica. http://blog.staedelmuseum.de/wp-content/uploads/2012/07/camera-obscura-sonnenfinsternis_1545-650x337.jpg, 1545. Accessed: 2023-10-22.

doi:10.6342/NTU202400740

[27] DF Malan. Euler Angles x-convention. https://en.wikipedia.org/wiki/File:EulerX.png, 2004. Accessed: 2023-10-15.

[28] DF Malan. Euler Angles, general convention. https://en.wikipedia.org/wiki/File:EulerG.png, 2004. Accessed: 2023-10-15.

[29] L. Brits. Euler angles, vector of File:Euler.png. https://commons.wikimedia.org/wiki/File:Eulerangles.svg, 2008. Accessed: 2023-10-15.

[30] B. H. Huang, Y. F. Tsao, F. S. Yang, and L. C. Chen. High-speed multi-line structured-light 3-d scanning system for accurate surface profilometry. In 9th International Conference of Asian Society for Precision Engineering and Nanotechnology (ASPEN2022), pages 738–742, 2022. doi: 10.3850/978-981-18-6021-8_OR-15-0111.

[31] X. Chen, Y. Chen, B. Chen, Z. He, Y. Ma, D. Zhang, and H. Najjaran. A camera intrinsic matrix-free calibration method for laser triangulation sensor. Sensors, 21 (2), 2021. ISSN 1424-8220. doi: 10.3390/s21020559. URL https://www.mdpi.com/1424-8220/21/2/559.

[32] Z. Zhang. A flexible new technique for camera calibration. IEEE Transactions on Pattern Analysis and Machine Intelligence, 22(11):1330–1334, 2000. doi: 10.1109/34.888718.

[33] A. Nordmann. Definition of full width at half maximum bandwidth for a resonance curve. https://commons.wikimedia.org/wiki/File:FWHM.svg, 2007. Accessed: 2024-1-4.

[34] C. Boucher. The Bivariate Normal Distribution. http://demonstrations.

doi:10.6342/NTU202400740

wolfram.com/TheBivariateNormalDistribution/, 2011. Accessed: 2024-1-16.

[35] Nexcis. Visualizazion of the method of Lagrange multipliers in 2D. https://commons.wikimedia.org/wiki/File:LagrangeMultipliers2D.svg, 2008. Accessed: 2024-1-14.

[36] Rotation Stages. https://www.onset-eo.com/drawing/CR04D.pdf, 2024. Accessed: 2024-1-22.

[37] PING LINKIN Factory P300+. https://en.ping3dp.com/single-material-desktop-3d-printer-p300, 2024. Accessed: 2024-1-22.

[38] Thomas G. Beckwith. Mechanincal Measurements, chapter 3. Pearson, 2008.

[39] Karl Strubecker. VORLESUNGEN ÜBER DARSTELLENDE GEOMETRIE, chapter II. Vandenhoeck and Ruprecht, Göttingen, 1967.

[40] Rossmann K. Point spread-function, line spread-function, and modulation transfer function. tools for the study of imaging systems. Radiology, 93(2):257–272, 1969. doi: 10.1148/93.2.257.

[41] Jack Hogan. 2D PSF solid and its projected intensity profile in 1D, the LSF. https://www.dpreview.com/forums/post/58273826?image=0, 2016. Accessed: 2024-1-14.

doi:10.6342/NTU202400740

Appendix A — Detailed Derivation of Model for Lateral Spot Size as a Function of Surface Tilting Angles

A.1 Preface and assumptions

The lateral spot size is just one of the information a light pattern entails about the surface tilting angle. As the surface tilting angle changes, the lateral spot size also changes. In this section, a step-by-step derivation for the lateral spot size is carried out. The lateral spot size at any surface tilting angle under a certain camera specification and viewing angle can be established. Before deriving the numerical relationship between surface tilting angle and the spot size, there are some crucial assumptions to be made for the ease of mathematical derivation as well as the generalizability of the final model.

First, the light source is assumed to be a point, creating a collimated light beam. The light beam can be seen as an infinite long cylinder with diameter d, and the center of the cylinder is aligning with z_w axis (Fig. A.2). Second, the local surface is placed at the origin of WCS. Thus, the intersection of the light beam and the local surface would create an elliptical light pattern. The tilting angle of the local area is at (θ, ϕ).

doi:10.6342/NTU202400740

Last but not least, the camera is assumed to be placed in the WCS at (l_x, l_y, l_z). Without loss of generality, the optical axis of CCS, i.e. positive z_c direction, is pointing towards the origin of WCS. This means that the object is placed right in the middle of the FOV of the camera. Next, the explanation starts with the mathematical description of a light spot on a tilted surface.

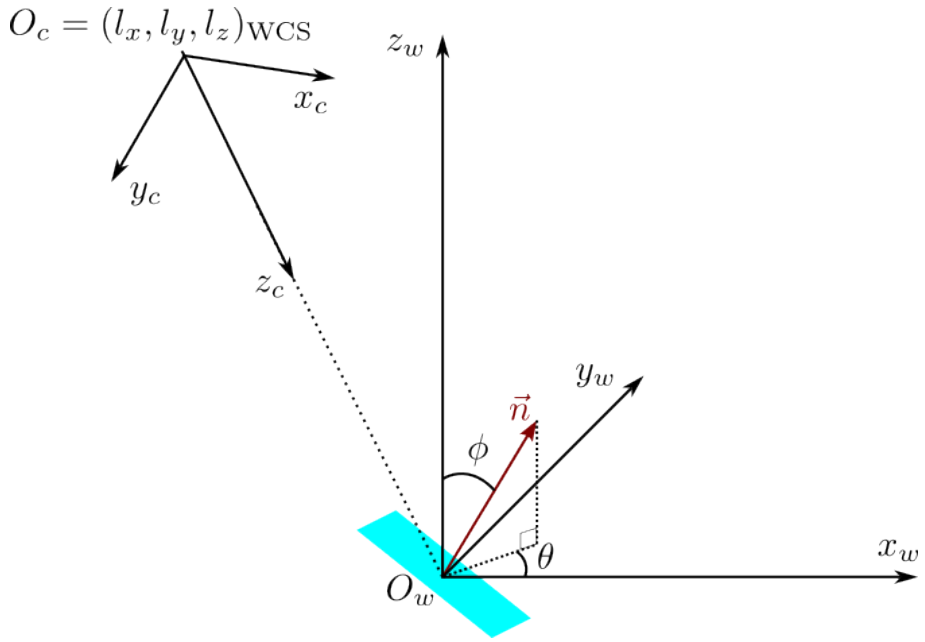

Figure A.1 Illustration of WCS, CCS and tilted local surface at origin of WCS

A.2 De La Hire's ellipse

The light beam is assumed to be a cylinder lying on z_w-axis. Let the beam diameter to be d. Thus, the radius of the cylinder is $d/2$. When a tilted surface is placed under the light beam, a cross-section is formed. The shape of the cross-section is the true shape of the light pattern. The shape of the cross-section is determined by the tilting angle of the normal vector with respect to z_w-axis. The shape would be a circle if there's no tilting, i.e. the tilting angle equals to zero, otherwise the shape would be an ellipse. Beam diameter

doi:10.6342/NTU202400740

controls the radius of the circle pattern, r, as well as the semi-minor axis of the ellipse, b.

$$b = d/2 \tag{A.1}$$

The semi-major axis, a, is determined by the tilting angle w.r.t. z_w-axis. Assume the angle between z_w-axis and the normal vector of the local surface is ϕ. Using trigonometry, we can calculate that

$$a = \frac{d}{2} \sec \phi \tag{A.2}$$

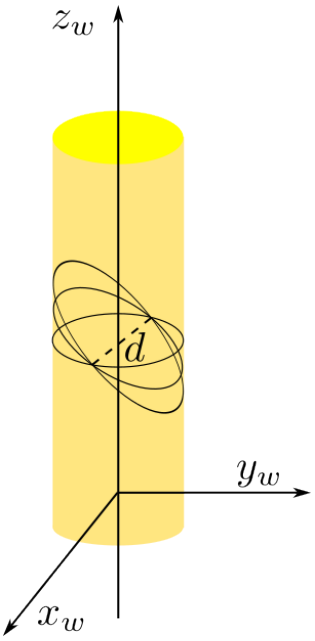

Figure A.2 The length of minor axis of every ellipses in the cylinder are all identical to the beam diameter d

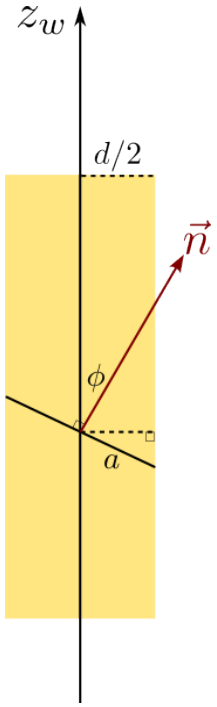

Figure A.3 The length of the semi-major axis can be written as a function of zenith angle and beam diameter

When the angle ϕ is 0, i.e. no tilting, semi-major axis and the semi-minor axis are the same length. The ellipse become a circle.

$$a = b = \frac{d}{2} \tag{A.3}$$

doi:10.6342/NTU202400740

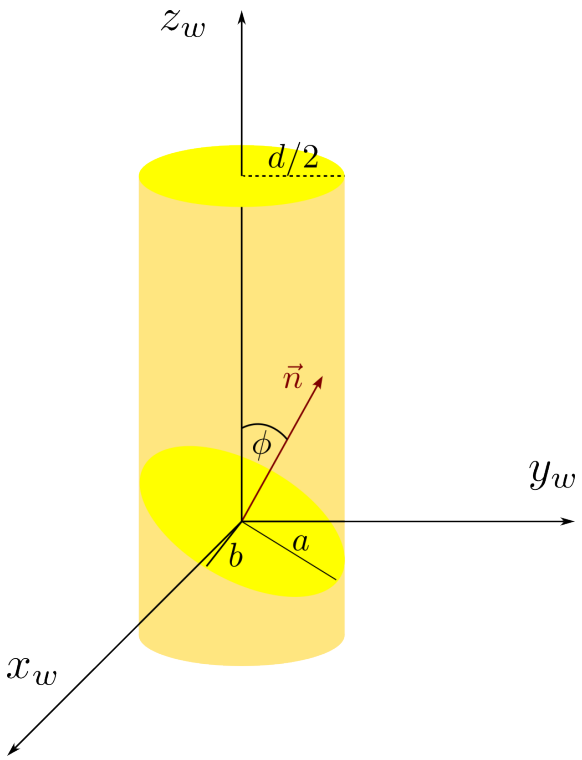

Figure A.4 The geometry of a light spot is determined by the cross-section of the local surface and the light beam

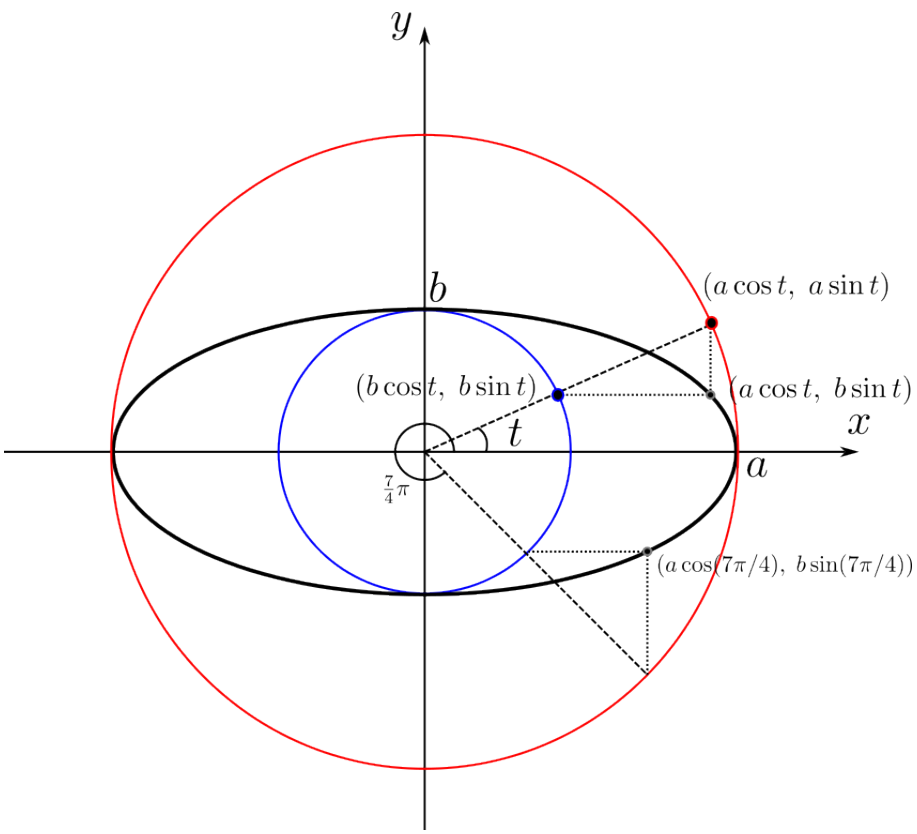

Figure A.5 Construction of de La Hire's ellipse is based on 2 concentric circles. The red circle has radius of length a, and the blue circle has radius of length b.

doi:10.6342/NTU202400740

To describe every point on the border of the ellipse, one can use de La Hire's construction of ellipse [39]. Coordinates of each point on the border of the light spot can be described using a parameter t, semi-major axis, a, and semi-minor axis, b. The de La Hire's ellipse on 2D space (plotted on $x_w y_w$ plane) is expressed as

$$\begin{bmatrix} x \\ y \end{bmatrix} = \begin{bmatrix} a\cos(t) \\ b\sin(t) \end{bmatrix} \tag{A.4}$$

In 3D WCS, extra coordinate is extended, so the expression becomes

$$\begin{bmatrix} x \\ y \\ z \end{bmatrix} = \begin{bmatrix} a\cos(t) \\ b\sin(t) \\ 0 \end{bmatrix} \tag{A.5}$$

Let there be a surface tilting on the local area. The azimuth angle is θ, and the zenith angle is ϕ. Therefore, the semi-major and semi-minor axes can be determined. To describe the actual curve that traces the border of the light spot in WCS, the curve is laid flat on the $x_w y_w$ plane initially. Next, the curve is rotated in 3D space as a rigid body according to surface tilting angle. To match the surface tilting angle (azimuth angle), the major-axis of the ellipse coincides with the x_w-axis. The center of the ellipse lies on the origin of the WCS. The coordinate of each point on the border becomes

$$\begin{bmatrix} x \\ y \\ z \end{bmatrix} = \begin{bmatrix} a\cos(t) \\ b\sin(t) \\ 0 \end{bmatrix} = \begin{bmatrix} \frac{d}{2}\sec(\phi)\cos(t) \\ \frac{d}{2}\sin(t) \\ 0 \end{bmatrix}, \ t \in [0, 2\pi) \tag{A.6}$$

The parameter t is a value between 0 and 2π. Each value of t corresponds to a distinct point on the border of the light spot. The shape of the light spot is now explicitly described, and each point on the border is clearly defined. However, the orientation of this ellipse in the 3 dimensional Cartesian space (WCS) is still not aligned with the actual light spot. In order to match the curve to the light spot on the tilted surface, rotating operator must be

doi:10.6342/NTU202400740

applied. For simplicity, extrinsic rotation with respect to Cartesian axes is adopted during the process of model derivation.

The ellipse is rotated w.r.t. y_w-axis at ϕ angle, which is also the zenith angle. This operation is denoted by $R_y(\phi)$. Next, the rotated shape is further rotated w.r.t. z_w-axis at θ angle, which is also the azimuth angle. This operation is denoted by $R_z(\theta)$. Therefore, the actual position of the perimeter of the light spot induced by the tilted surface can be calculated as below.

$$\begin{aligned}
\begin{bmatrix} x \\ y \\ z \end{bmatrix} &= R_z(\theta)R_y(\phi)\begin{bmatrix} \frac{d}{2}\sec(\phi)\cos(t) \\ \frac{d}{2}\sin(t) \\ 0 \end{bmatrix} \\
&= \begin{bmatrix} \cos(\theta) & -\sin(\theta) & 0 \\ \sin(\theta) & \cos(\theta) & 0 \\ 0 & 0 & 1 \end{bmatrix}\begin{bmatrix} \cos(\phi) & 0 & \sin(\phi) \\ 0 & 1 & 0 \\ -\sin(\phi) & 0 & \cos(\phi) \end{bmatrix}\begin{bmatrix} \frac{d}{2}\sec(\phi)\cos(t) \\ \frac{d}{2}\sin(t) \\ 0 \end{bmatrix} \\
&= \begin{bmatrix} \frac{d}{2}\cos(t)\cos(\theta) - \frac{d}{2}\sin(t)\sin(\theta) \\ \frac{d}{2}\cos(t)\sin(\theta) + \frac{d}{2}\sin(t)\cos(\theta) \\ -\frac{d}{2}\tan(\phi)\cos(t) \end{bmatrix} = \frac{d}{2}\begin{bmatrix} \cos(t)\cos(\theta) - \sin(t)\sin(\theta) \\ \cos(t)\sin(\theta) + \sin(t)\cos(\theta) \\ -\tan(\phi)\cos(t) \end{bmatrix}
\end{aligned} \tag{A.7}$$

Again, the parameter t is a value between 0 and 2π. Eq. (A.7) describes the true shape of the light spot through its perimeter in three-dimensional Cartesian space, i.e. in the WCS.

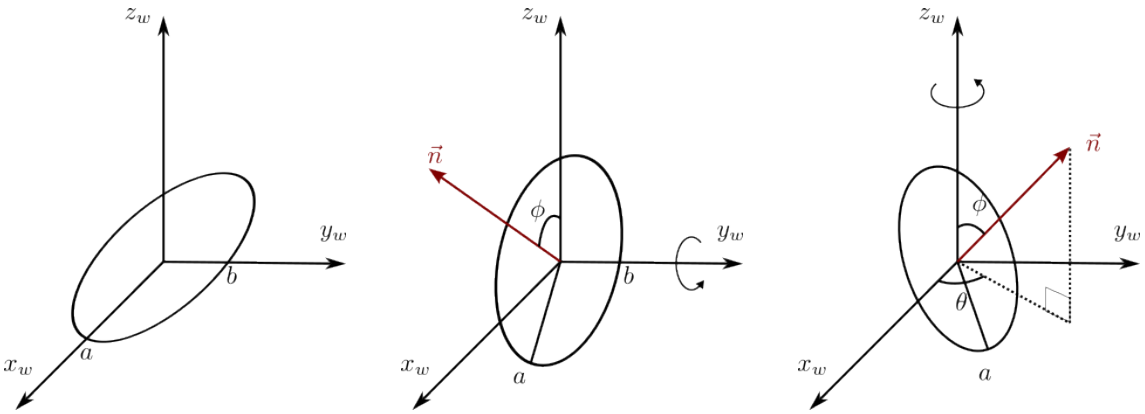

Figure A.6 Steps to rotate the ellipse to correct orientation (Order: left to right)

doi:10.6342/NTU202400740

A.3 Extreme points of the ellipse

Actual shape and actual size of the light spot are determined by the tilting angles of local surface. However, from different observing angle, perceived shape and size can still be different. Thus, the coordinate of the border of the light spot should be projected onto image plane for explicit relationship between perceived size of light spot and the tilting angles. Projection of the light spot to image plane involves 2 coordinate transformations:

1. **Transform the coordinates from WCS to CCS**

2. **Transform camera coordinate to image coordinate**

The projection of the light spot to image plane is actually done by camera matrix, which is introduced in Chapter 3. The first step is to perform a translation and rotation of the coordinate system, and the second step is to project 3D object in CCS to 2D plane. Without loss of generality, the translational vector $\vec{\mathbf{T}}$ is set to be

$$\vec{\mathbf{T}} = [l_x, l_y, l_z]^\intercal \tag{A.8}$$

and the rotation matrix **R** is set to be

$$\mathbf{R} = \begin{bmatrix} R_{11} & R_{12} & R_{13} \\ R_{21} & R_{22} & R_{23} \\ R_{31} & R_{32} & R_{33} \end{bmatrix} \tag{A.9}$$

$$\begin{aligned} \begin{bmatrix} u \\ v \\ 1 \end{bmatrix} &= \mathbf{KR} \begin{bmatrix} \mathbf{I} & -\vec{\mathbf{T}} \end{bmatrix} \begin{bmatrix} x \\ y \\ z \\ 1 \end{bmatrix} = \mathbf{KR} \begin{bmatrix} 1 & 0 & 0 & -l_x \\ 0 & 1 & 0 & -l_y \\ 0 & 0 & 1 & -l_z \end{bmatrix} \begin{bmatrix} x \\ y \\ z \\ 1 \end{bmatrix} \\ &= \mathbf{K} \begin{bmatrix} R_{11} & R_{12} & R_{13} \\ R_{21} & R_{22} & R_{23} \\ R_{31} & R_{32} & R_{33} \end{bmatrix} \begin{bmatrix} x - l_x \\ y - l_y \\ z - l_z \end{bmatrix} \end{aligned} \tag{A.10}$$

doi:10.6342/NTU202400740

Let

$$\begin{cases} x' = x - l_x \\ y' = y - l_y \\ z' = z - l_z \end{cases} \tag{A.11}$$

The skew factor, s in the camera intrinsic matrix is assumed to be 0, then Eq. (A.10) becomes

$$\begin{bmatrix} u \\ v \\ 1 \end{bmatrix} = \begin{bmatrix} f_x & 0 & o_x \\ 0 & f_y & o_y \\ 0 & 0 & 1 \end{bmatrix} \begin{bmatrix} R_{11}x' + R_{12}y' + R_{13}z' \\ R_{21}x' + R_{22}y' + R_{23}z' \\ R_{31}x' + R_{32}y' + R_{33}z' \end{bmatrix} \tag{A.12}$$

$$= \begin{bmatrix} f_x\big(R_{11}x' + R_{12}y' + R_{13}z'\big) + o_x\big(R_{31}x' + R_{32}y' + R_{33}z'\big) \\ f_y\big(R_{21}x' + R_{22}y' + R_{23}z'\big) + o_y\big(R_{31}x' + R_{32}y' + R_{33}z'\big) \\ R_{31}x' + R_{32}y' + R_{33}z' \end{bmatrix} \tag{A.13}$$

$$= \begin{bmatrix} f_x \dfrac{R_{11}x' + R_{12}y' + R_{13}z'}{R_{31}x' + R_{32}y' + R_{33}z'} + o_x \\ f_y \dfrac{R_{21}x' + R_{22}y' + R_{23}z'}{R_{31}x' + R_{32}y' + R_{33}z'} + o_y \\ 1 \end{bmatrix} \tag{A.14}$$

Now, it is important to identify what object in the CCS needs to be analyzed. The object of interest in this case is the elliptic light spot, which is constructed by de La Hire's method as mentioned in Eq. (A.7). The ellipse defined this way can be parameterized by a single parameter, t. This property is useful for locating the analytic position of the extreme point of the ellipse.

To put it more precisely, the lateral size of the ellipse is defined by the horizontal distance between the leftmost and the rightmost point of the ellipse. Therefore, the points of interests correspond to the points where $\dfrac{\mathrm{d}}{\mathrm{d}t}u = 0$.

doi:10.6342/NTU202400740

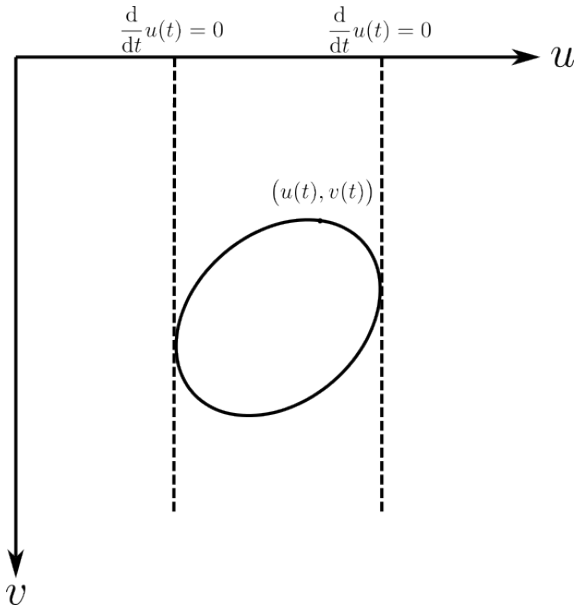

Figure A.7 The spot size is defined as the distance from the left extreme point to right extreme point on u axis, i.e. the horizontal axis of an image.

Plug u given in Eq. (A.14) into $\dfrac{\mathrm{d}}{\mathrm{d}t}u=0$, we get

$$\begin{aligned}0=\frac{\mathrm{d}}{\mathrm{d}t}u&=\frac{\mathrm{d}}{\mathrm{d}t}\Big(f_x\frac{R_{11}x'+R_{12}y'+R_{13}z'}{R_{31}x'+R_{32}y'+R_{33}z'}+o_x\Big)\\&=\frac{\mathrm{d}}{\mathrm{d}t}f_x\frac{R_{11}x'+R_{12}y'+R_{13}z'}{R_{31}x'+R_{32}y'+R_{33}z'}+\frac{\mathrm{d}}{\mathrm{d}t}o_x\\&=f_x\frac{\mathrm{d}}{\mathrm{d}t}\frac{R_{11}x'+R_{12}y'+R_{13}z'}{R_{31}x'+R_{32}y'+R_{33}z'}\quad\because o_x\text{ is a constant}\end{aligned}\tag{A.15}$$

Since $x'=x-l_x$, it is also a function of parameter t, so are y' and z'. The numerator and denominator in Eq. (A.15) can be simplified as $f(t)$ and $g(t)$. Then

$$f(t)=R_{11}x'+R_{12}y'+R_{13}z'\tag{A.16}$$

$$g(t)=R_{31}x'+R_{32}y'+R_{33}z'\tag{A.17}$$

$$\begin{aligned}\therefore\quad 0&=f_x\frac{\mathrm{d}}{\mathrm{d}t}\frac{R_{11}x'+R_{12}y'+R_{13}z'}{R_{31}x'+R_{32}y'+R_{33}z'}=f_x\frac{\mathrm{d}}{\mathrm{d}t}\frac{f(t)}{g(t)}\\&=f_x\frac{f'(t)g(t)-f(t)g'(t)}{\big(g(t)\big)^2}\end{aligned}\tag{A.18}$$

doi:10.6342/NTU202400740

For Eq. (A.18) to be true, the numerator has to be 0 under the constraint of

$$\big(g(t)\big)^2 \neq 0 \tag{A.19}$$

This constraint can be proven to be valid in CCS since that $g(t)$ is originally $z' = z - l_z$, the z-coordinate in CCS according to (A.13) and (A.17). The objects being captured must be placed in front of the camera, that is the positive z region in CCS. Objects cannot be placed on the origin of CCS, which is the position of the camera center. Thus, (A.19) holds.

Given that the numerator of (A.18) has to be 0, it can be deduced that

$$f'(t)g(t) = g'(t)f(t) \tag{A.20}$$

$$\begin{aligned}
f'(t)g(t) &= \left(\frac{\mathrm{d}}{\mathrm{d}t}\big(x'R_{11} + y'R_{12} + z'R_{13}\big)\right)g(t) \\
&= \left(\frac{\mathrm{d}}{\mathrm{d}t}\big(x'R_{11}\big) + \frac{\mathrm{d}}{\mathrm{d}t}\big(y'R_{12}\big) + \frac{\mathrm{d}}{\mathrm{d}t}\big(z'R_{13}\big)\right)g(t) \\
&= \left(R_{11}\frac{\mathrm{d}}{\mathrm{d}t}\big(\frac{d}{2}\cos(t+\theta) - l_x\big) + R_{12}\frac{\mathrm{d}}{\mathrm{d}t}\big(\frac{d}{2}\sin(t+\theta) - l_y\big)\right. \\
&\quad \left. + R_{13}\frac{\mathrm{d}}{\mathrm{d}t}\big(\frac{-d}{2}\tan\phi\cos(t) - l_z\big)\right)g(t) \quad \text{using (A.7)} \\
&= \left(R_{11}\frac{d}{2}\big(-\sin(t+\theta)\big) + R_{12}\frac{d}{2}\cos(t+\theta) + R_{13}\frac{d}{2}\tan\phi\sin t\right)g(t) \\
&= \frac{d}{2}\Big(-R_{11}\sin(t+\theta) + R_{12}\cos(t+\theta) + R_{13}\tan\phi\sin t\Big) \\
&\quad \times (x'R_{31} + y'R_{32} + z'R_{33}) \\
&= \frac{d}{2}(\mathbf{1}^* + \mathbf{2}^* + \mathbf{3}^*)
\end{aligned} \tag{A.21}$$

doi:10.6342/NTU202400740

$$\mathbf{1}^* = -R_{11}\sin(t+\theta)x'R_{31} + R_{12}\cos(t+\theta)x'R_{31} + R_{13}\tan\phi\sin(t)x'R_{31} \quad \text{(A.22)}$$

$$\mathbf{2}^* = -R_{11}\sin(t+\theta)y'R_{32} + R_{12}\cos(t+\theta)y'R_{32} + R_{13}\tan\phi\sin(t)y'R_{32} \quad \text{(A.23)}$$

$$\mathbf{3}^* = -R_{11}\sin(t+\theta)z'R_{33} + R_{12}\cos(t+\theta)z'R_{33} + R_{13}\tan\phi\sin(t)z'R_{33} \quad \text{(A.24)}$$

$$\begin{aligned}
g'(t)f(t) &= \left(\frac{\mathrm{d}}{\mathrm{d}t}\big(x'R_{31} + y'R_{32} + z'R_{33}\big)\right)f(t) \\
&= \left(\frac{\mathrm{d}}{\mathrm{d}t}\big(x'R_{31}\big) + \frac{\mathrm{d}}{\mathrm{d}t}\big(y'R_{32}\big) + \frac{\mathrm{d}}{\mathrm{d}t}\big(z'R_{33}\big)\right)f(t) \\
&= \left(R_{31}\frac{\mathrm{d}}{\mathrm{d}t}\big(\frac{d}{2}\cos(t+\theta) - l_x\big) + R_{32}\frac{\mathrm{d}}{\mathrm{d}t}\big(\frac{d}{2}\sin(t+\theta) - l_y\big)\right. \\
&\quad \left. + R_{33}\frac{\mathrm{d}}{\mathrm{d}t}\big(\frac{-d}{2}\tan\phi\cos(t) - l_z\big)\right)f(t) \quad \text{using (A.7)} \\
&= \left(R_{31}\frac{d}{2}\big(-\sin(t+\theta)\big) + R_{32}\frac{d}{2}\cos(t+\theta) + R_{33}\frac{d}{2}\tan\phi\sin t\right)f(t) \\
&= \frac{d}{2}\Big(-R_{31}\sin(t+\theta) + R_{32}\cos(t+\theta) + R_{33}\tan\phi\sin t\Big) \\
&\quad \times (x'R_{11} + y'R_{12} + z'R_{13}) \\
&= \frac{d}{2}(\mathbf{4}^* + \mathbf{5}^* + \mathbf{6}^*)
\end{aligned} \quad \text{(A.25)}$$

$$\mathbf{4}^* = -R_{31}\sin(t+\theta)x'R_{11} + R_{32}\cos(t+\theta)x'R_{11} + R_{33}\tan\phi\sin(t)x'R_{11} \quad \text{(A.26)}$$

$$\mathbf{5}^* = -R_{31}\sin(t+\theta)y'R_{12} + R_{32}\cos(t+\theta)y'R_{12} + R_{33}\tan\phi\sin(t)y'R_{12} \quad \text{(A.27)}$$

$$\mathbf{6}^* = -R_{31}\sin(t+\theta)z'R_{13} + R_{32}\cos(t+\theta)z'R_{13} + R_{33}\tan\phi\sin(t)z'R_{13} \quad \text{(A.28)}$$

doi:10.6342/NTU202400740

$$
\begin{aligned}
0 = f'(t)g(t) - g'(t)f(t) &= \frac{d}{2}(\mathbf{1}^* + \mathbf{2}^* + \mathbf{3}^* - \mathbf{4}^* - \mathbf{5}^* - \mathbf{6}^*) \\
&= \frac{d}{2}\big((\mathbf{1}^* - \mathbf{4}^*) + (\mathbf{2}^* - \mathbf{5}^*) + (\mathbf{3}^* - \mathbf{6}^*)\big) \\
&= \frac{d}{2}\Big(\big(R_{12}\cos(t+\theta)x'R_{31} + R_{13}\tan\phi\sin(t)x'R_{31} - R_{32}\cos(t+\theta)x'R_{11} - R_{33}\tan\phi\sin(t)x'R_{11}\big) \\
&\quad + \big(- R_{11}\sin(t+\theta)y'R_{32} + R_{13}\tan\phi\sin(t)y'R_{32} + R_{31}\sin(t+\theta)y'R_{12} - R_{33}\tan\phi\sin(t)y'R_{12}\big) \\
&\quad + \big(- R_{11}\sin(t+\theta)z'R_{33} + R_{12}\cos(t+\theta)z'R_{33} + R_{31}\sin(t+\theta)z'R_{13} - R_{32}\cos(t+\theta)z'R_{13}\big)\Big)
\end{aligned}
\tag{A.29}
$$

After some rearrangement and substitution of x', y' and z', (A.29) can be expressed as below

$$
\begin{aligned}
0 = f'(t)g(t) - g'(t)f(t) &= A\cos(t+\theta) + B\sin(t+\theta) + C\sin(t) + D \\
&= E\cos(t-\delta) + D \quad \text{(using trigonometric identities)}
\end{aligned}
\tag{A.30}
$$

where

$$A = (-R_{12}R_{31} + R_{32}R_{11})l_x + (-R_{12}R_{33} + R_{32}R_{13})l_z \tag{A.31}$$

$$B = (R_{11}R_{32} - R_{31}R_{12})l_y + (R_{11}R_{33} - R_{31}R_{13})l_z \tag{A.32}$$

$$C = \big((-R_{13}R_{31} + R_{33}R_{11})l_x + (-R_{13}R_{32} + R_{33}R_{12})l_y\big)\tan(\phi) \tag{A.33}$$

$$
\begin{aligned}
D = {} & R_{12}\frac{d}{2}R_{31} - R_{11}\frac{d}{2}R_{32} - R_{13}\tan(\phi)\frac{d}{2}R_{31}\sin(\theta) + R_{13}\tan(\phi)\frac{d}{2}R_{32}\cos(\theta) \\
& + R_{11}\frac{d}{2}\tan(\phi)R_{33}\sin(\theta) - R_{12}\frac{d}{2}\tan(\phi)R_{33}\cos(\theta)
\end{aligned}
\tag{A.34}
$$

$$E = \sqrt{\big(A\cos(\theta) + B\sin(\theta)\big)^2 + \big(- A\sin(\theta) + B\cos(\theta) + C\big)^2} \tag{A.35}$$

$$\delta = \arctan\frac{-A\sin(\theta) + B\cos(\theta) + C}{A\cos(\theta) + B\sin(\theta)} \tag{A.36}$$

doi:10.6342/NTU202400740

Also, consider the other case

$$0 = g'(t)f(t) - f'(t)g(t) = -A\cos(t+\theta) - B\sin(t+\theta) - C\sin(t) - D$$
$$= E'\cos(t-\delta') - D \tag{A.37}$$

where

$$E' = \sqrt{\big(-A\cos(\theta) - B\sin(\theta)\big)^2 + \big(A\sin(\theta) - B\cos(\theta) - C\big)^2} = E \tag{A.38}$$

$$\delta' = \arctan\frac{A\sin(\theta) - B\cos(\theta) - C}{-A\cos(\theta) - B\sin(\theta)} = \arctan\frac{-A\sin(\theta) + B\cos(\theta) + C}{A\cos(\theta) + B\sin(\theta)} = \delta \tag{A.39}$$

Thus, Eq. (A.37) becomes

$$0 = E\cos(t-\delta) - D \tag{A.40}$$

Therefore,

$$\frac{\mathrm{d}u}{\mathrm{d}t} = 0 \implies t \in \Big\{\, t \;\Big|\; E\cos(t-\delta) + D = 0 \vee E\cos(t-\delta) - D = 0\Big\} \tag{A.41}$$

$\frac{\mathrm{d}u}{\mathrm{d}t} = 0$ implies that the solution of t satisfy (A.30) or (A.40). Notice that there are 2 possible solutions for Eq. (A.30) as well as Eq. (A.40) for $t \in [0, 2\pi)$. Thus, there are 4 possible solutions in total. However, there are only 2 extreme points on any perceived ellipse. To

doi:10.6342/NTU202400740

obtain correct solutions, Eq. (A.30) and Eq. (A.40) are considered simultaneously.

$$
\begin{aligned}
&\big(E\cos(t-\delta)+D\big)\big(E\cos(t-\delta)-D\big)=0\\
&E^2\cos^2(t-\delta)-D^2=0\\
&\cos^2(t-\delta)=\frac{D^2}{E^2}=\frac{\cos\big(2(t-\delta)\big)+1}{2}\\
&\cos\big(2(t-\delta)\big)=\frac{2D^2}{E^2}-1\\
&2(t-\delta)=\pm\arccos(\frac{2D^2}{E^2}-1)+2n\pi,\quad \text{where } n\in\mathbb{Z}\\
&t-\delta=\pm\,0.5\arccos(\frac{2D^2}{E^2}-1)+n\pi,\quad \text{where } n\in\mathbb{Z}\\
\therefore\quad &t=\delta\pm\,0.5\arccos(\frac{2D^2}{E^2}-1)+n\pi,\quad \text{where } n\in\mathbb{Z}
\end{aligned}
\tag{A.42}
$$

Under the constraint of $t\in[0,2\pi)$, $n=1$ and n can only be 1. If $n\geq 2$, then t can be greater than 2π. If $n\leq 0$, then t can be lesser than 0, $t\notin[0,2\pi)$. It suffices to show $-\pi\leq\delta\pm\,0.5\arccos(\frac{2D^2}{E^2}-1)<\pi$, so that $t\in[0,2\pi)$ for n equals to 1.

According to (A.36), δ is a function of arctan, so its range is $(-\pi/2,\pi/2)$. arccos has a range of $[0,\pi]$. Thus, the lower and upper limit of

$$\arctan(\cdot)\pm 0.5\arccos(\cdot)$$

are $-\pi/2-0.5\pi=-\pi$, and $\pi/2+0.5\pi=\pi$. Thus, $-\pi\leq\delta\pm\,0.5\arccos(\frac{2D^2}{E^2}-1)<\pi$ Therefore,

$$t=\delta\pm\,0.5\arccos(\frac{2D^2}{E^2}-1)+\pi \tag{A.43}$$

As a result, under a fixed circumstance (fixed camera specs, position, object tilting angle) the distance between the leftmost edge and the rightmost edge of the ellipse appears on

doi:10.6342/NTU202400740

the image is calculated by

$$|u(t_1) - u(t_2)| \tag{A.44}$$

where u is calculated as shown in (A.10) and

$$t_1 = \delta + 0.5 \arccos(\frac{2D^2}{E^2} - 1) + \pi \tag{A.45}$$

$$t_2 = \delta - 0.5 \arccos(\frac{2D^2}{E^2} - 1) + \pi \tag{A.46}$$

Notice that the system parameters (camera specs, position, viewing angle) and the object tilting angles (θ and ϕ) are contained in the terms δ, D and E.

It is crucial to acknowledge the difference between real light spots and the spots in this model. The light spot in this model has a clearly defined boundary, its shape can be seen as an ellipse in a 3D Cartesian space, while the light spot in reality is blurred. There is no clear boundary for a real light spot. In practice, the boundary of a real light spot can be extracted from image processing, since the light intensity of same value from the same light spot forms a shape approximately like an ellipse. Therefore, this model still holds for practical use.

Further details regarding the validity of applicability in real scenario are provided in Appendix B.

doi:10.6342/NTU202400740

Appendix B — Theoretical Rationale for Leveraging the Characteristics of Light Spots in Line Patterns

B.1 Preface

Most of the time, clear boundaries of light spots are not present in actual images. In this research, a virtual boundary is generated by fitting a bivariate Gaussian distribution to the light spot. The contour lines of the Gaussian distribution can be considered as the boundary of the light spot.

As defined in chapter 4, the boundary line of the light spot is the contour line corresponding to half the maximum. A natural question arises: can the lateral spot size model be extended to this contour? If the answer is positive, another problem arises. How can the usage of this model on line patterns be justified when the model is built upon light spots?

As a result, the following two sections attempt to answer these questions respectively, and eventually affirm the validity of usage.

doi:10.6342/NTU202400740

B.2 Relationship between lateral spot size and the contour of half maximum

This section offers a comprehensive rationale for employing the spot size model on light spots with blurred boundaries. The challenge lies in applying a spot size model, originally designed for sharp boundaries, to actual images where light spot boundaries are defined by the contour of a fixed intensity. This creates a counter-intuitive scenario. Therefore, an explicit formula for the lateral spot size of blurred light spots must be established.

Proposition 1: *Let $f(x,y)$ be a Gaussian distribution with parameters μ_x , μ_y , σ_x , σ_y , ρ and C_{HM} the contour line at half maximum of $f(x,y)$. The distance between the maximum and minimum value of x on C_{HM}, i.e. lateral spot size, is*

$$x_{max} - x_{min} = 2\sqrt{2\ln 2}\sigma_x$$

while $\rho \neq \pm 1$ and $\sigma_y \neq 0$

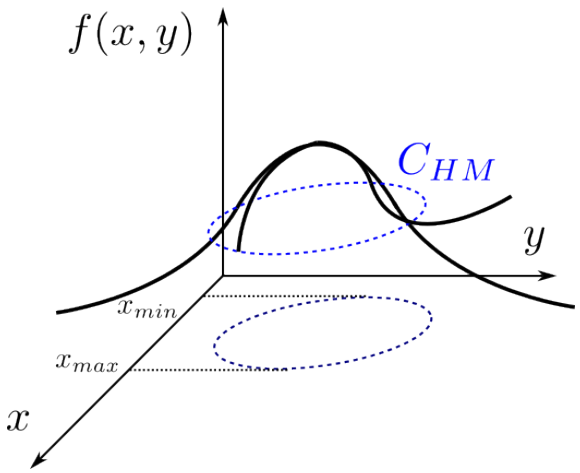

Figure B.8 An illustration of a bivariate Gaussian distribution and the contour of half maximum

doi:10.6342/NTU202400740

Proposition 1 asserts that the lateral spot size for a light spot with blurred boundaries can be expressed solely as a function of the standard deviation along the x-axis. It is independent of the shape of the light spot along the y-axis. Notably, the formula closely resembles the Full Width at Half Maximum (FWHM) for a 1D Gaussian distribution, differing only in the term for standard deviation. In the case of the FWHM in a 1D Gaussian, the standard deviation is denoted as σ, whereas in this formula, it is denoted as σ_x.

$f(x, y)$ is a bivariate Gaussian distribution, and it is expressed as

$$f(x,y) = \frac{1}{2\pi\sigma_x\sigma_y\sqrt{1-\rho^2}} \exp\left(-\frac{1}{2(1-\rho^2)}\left(\left(\frac{x-\mu_x}{\sigma_x}\right)^2 - \frac{2\rho(x-\mu_x)(y-\mu_y)}{\sigma_x\sigma_y} + \left(\frac{y-\mu_y}{\sigma_y}\right)^2\right)\right)$$

Maximum occurs when $x = \mu_x$ and $y = \mu_y$, that is

$$f(x,y) = \frac{1}{2\pi\sigma_x\sigma_y\sqrt{1-\rho^2}} \tag{B.47}$$

Half maximum occurs when

$$f(x,y) = \frac{0.5}{2\pi\sigma_x\sigma_y\sqrt{1-\rho^2}} \tag{B.48}$$

Every point lying on C_{HM} yield this value.

$$\exp\left(-\frac{1}{2(1-\rho^2)}\left(\left(\frac{x-\mu_x}{\sigma_x}\right)^2 - \frac{2\rho(x-\mu_x)(y-\mu_y)}{\sigma_x\sigma_y} + \left(\frac{y-\mu_y}{\sigma_y}\right)^2\right)\right) = 0.5 = 2^{-1}$$

$$-\frac{1}{2(1-\rho^2)}\left(\left(\frac{x-\mu_x}{\sigma_x}\right)^2 - \frac{2\rho(x-\mu_x)(y-\mu_y)}{\sigma_x\sigma_y} + \left(\frac{y-\mu_y}{\sigma_y}\right)^2\right) = -\ln 2$$

$$\left(\frac{x-\mu_x}{\sigma_x}\right)^2 - \frac{2\rho(x-\mu_x)(y-\mu_y)}{\sigma_x\sigma_y} + \left(\frac{y-\mu_y}{\sigma_y}\right)^2 = 2(1-\rho^2)\ln 2 \tag{B.49}$$

doi:10.6342/NTU202400740

Multiply both sides of the Eq. (B.49) by $\sigma_x^2\sigma_y^2$,

$$(x-\mu_x)^2\sigma_y^2 - 2\rho(x-\mu_x)(y-\mu_y)\sigma_x\sigma_y + (y-\mu_y)^2\sigma_x^2 = 2(1-\rho^2)\sigma_x^2\sigma_y^2\ln 2 \quad \text{(B.50)}$$

Eq. (B.50) is in fact an elliptical equation of x and y. This exactly describes the contour, C_{HM}.

To find the extreme points on x-direction, i.e. x_{min} and x_{max} of this contour, one can utilize implicit differentiation to find the differential form of the contour. Take derivative of y on both sides of Eq. (B.50)

$$\frac{\mathrm{d}}{\mathrm{d}y}\left((x-\mu_x)^2\sigma_y^2 - 2\rho(x-\mu_x)(y-\mu_y)\sigma_x\sigma_y + (y-\mu_y)^2\sigma_x^2\right) = \frac{\mathrm{d}}{\mathrm{d}y}\left(2(1-\rho^2)\sigma_x^2\sigma_y^2\ln 2\right) = 0$$

$$2(x-\mu_x)\sigma_y^2\frac{\mathrm{d}x}{\mathrm{d}y} - 2\rho\sigma_x\sigma_y\left((y-\mu_y)\frac{\mathrm{d}x}{\mathrm{d}y} + (x-\mu_x)\right) + 2(y-\mu_y)\sigma_x^2 = 0 \quad \text{(B.51)}$$

$$\left((x-\mu_x)\sigma_y^2 - \rho\sigma_x\sigma_y((y-\mu_y)\right)\frac{\mathrm{d}x}{\mathrm{d}y} = \rho\sigma_x\sigma_y(x-\mu_x) - (y-\mu_y)\sigma_x^2 \quad \text{(B.52)}$$

$$\therefore \frac{\mathrm{d}x}{\mathrm{d}y} = \frac{\rho\sigma_x\sigma_y(x-\mu_x) - (y-\mu_y)\sigma_x^2}{-\rho\sigma_x\sigma_y(y-\mu_y) + (x-\mu_x)\sigma_y^2} \quad \text{(B.53)}$$

Extreme points occur at $\dfrac{\mathrm{d}x}{\mathrm{d}y} = 0$, i.e.

$$\frac{\rho\sigma_x\sigma_y(x-\mu_x) - (y-\mu_y)\sigma_x^2}{-\rho\sigma_x\sigma_y(y-\mu_y) + (x-\mu_x)\sigma_y^2} = 0 \quad \text{(B.54)}$$

$$\therefore \rho\sigma_x\sigma_y(x-\mu_x) = (y-\mu_y)\sigma_x^2$$

$$\rho\sigma_y(x-\mu_x) = (y-\mu_y)\sigma_x \quad \text{(B.55)}$$

Also, the denominator cannot be 0.

$$-\rho\sigma_x\sigma_y(y-\mu_y) + (x-\mu_x)\sigma_y^2 \neq 0 \quad \text{(B.56)}$$

doi:10.6342/NTU202400740

Verifying the solution given by Eq. (B.55),

$$-\rho^2\sigma_y^2(x-\mu_x)+(x-\mu_x)\sigma_y^2\neq 0 \tag{B.57}$$

$$(1-\rho^2)(x-\mu_x)\sigma_y^2\neq 0 \tag{B.58}$$

$$\rho\neq 1\vee -1,\ x\neq\mu_x,\ \text{and}\ \sigma_y\neq 0$$

$\rho\neq\pm 1$ means that Eq. (B.55) holds when x and y are not linearly correlated. Geometrically speaking, when elliptical contour collapses to a line, extreme point do not exists.

$x\neq\mu_x$ is valid since the extreme point of C_{HM} is obviously not located on $x=\mu_x$

$\sigma_y\neq 0$ also means the elliptical contour collapses to a line, the line only has a fixed y-value. If the shape looks like a horizontal line, then Eq. (B.55) does not hold.

Plugging Eq. (B.55) back to the elliptical equation (B.50), the solution to the maximum and minimum x value can be obtained.

$$(x-\mu_x)^2\sigma_y^2-2\rho^2(x-\mu_x)^2\sigma_y^2+\rho^2\sigma_y^2(x-\mu_x)^2=2(1-\rho^2)\sigma_x^2\sigma_y^2\ln 2 \tag{B.59}$$

$$(x-\mu_x)^2-2\rho^2(x-\mu_x)^2+\rho^2(x-\mu_x)^2=2(1-\rho^2)\sigma_x^2\ln 2 \tag{B.60}$$

$$(1-\rho^2)(x-\mu_x)^2=2(1-\rho^2)\sigma_x^2\ln 2 \tag{B.61}$$

$$\therefore (x-\mu_x)^2=2\sigma_x^2\ln 2,\quad x-\mu_x=\pm\sqrt{2\ln 2}\sigma_x \tag{B.62}$$

$$x_{max}-x_{min}=(\mu_x+\sqrt{2\ln 2}\sigma_x)-(\mu_x-\sqrt{2\ln 2}\sigma_x)=2\sqrt{2\ln 2}\sigma_x\quad\square \tag{B.63}$$

Equating this and the lateral spot size formula (A.44) in appendix A,

$$x_{max}-x_{min}=|u(t_1)-u(t_2)|=2\sqrt{2\ln 2}\sigma_x \tag{B.64}$$

doi:10.6342/NTU202400740

it is apparent that the spot size formula is related to the standard deviation of the light spot when the boundary is blurred.

This concludes Proposition 1. Moreover, the proposed lateral spot size model in Appendix A is applicable to light spots with blurred boundaries. The subsequent section will demonstrate the extension of the lateral spot size model to line patterns, with the key insight derived from the formula presented in Proposition 1.

B.3 Extension from light spots to line patterns

The line patterns exhibit an entirely different appearance from a light spot. Some may argue that a line can be considered as an infinite combination of closely packed spots. However, this argument lacks rigor and does not provide a sufficient explanation for applying the lateral spot size model to line patterns.

This section aims to provide a theoretical rationale for the validity of applying the lateral spot size model to line patterns. The intended outcome is to show that certain properties remain unchanged when extending a spot to a line. These properties can then be utilized to infer the lateral spot size when only line patterns are observable.

The images of a light spot are often referred to as point spread functions (PSF), where the function has 2 inputs, the coordinates x and y, and 1 output, the intensity at that coordinate. The cross-sectional intensity of a line pattern are often referred to as line spread functions (LSF), where the function has 1 input, the coordinate x, and 1 output, the intensity at that position. It is known that LSF is in fact the integration of PSF in one direction [40]. From the perspective of probability theory, a PSF can be viewed as a joint density function of 2 random variables, and LSF is the marginal density function. This

doi:10.6342/NTU202400740

can be expressed as

$$LSF(x) = \int_{-\infty}^{\infty} PSF(x, y)\mathrm{d}y \tag{B.65}$$

This relation can be obtained from convolution of PSF with 2D linear delta function (infinity on y-axis, 0 everywhere else). The illustration of the concept behind this formula is plotted below.

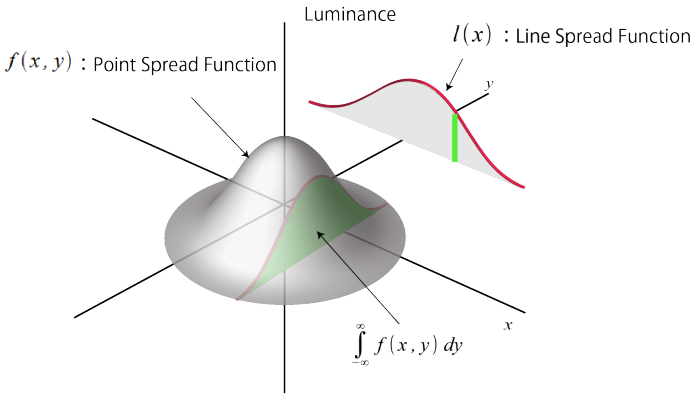

Fig.18 Point Spread Function and Line Spread Function

Figure B.9 The value of $LSF(x)$ is the accumulation of the luminance on y-axis [41]

Proposition 2: *The cross-sectional intensity profile of the line pattern (i.e. LSF) follows Gaussian distribution, $\mathcal{N}(\mu_1, \sigma_1)$, with mean μ_1 and standard deviation σ_1 if the point light pattern (i.e. PSF) follows a bivariate Gaussian distribution, $\mathcal{N}(\mu_1, \mu_2, \sigma_1, \sigma_2, \rho)$*

A bivariate Gaussian distribution with parameters $\mu_1, \mu_2, \sigma_1, \sigma_2, \rho$ is expressed as

$$f_{X_1X_2}(x_1, x_2) = \frac{1}{2\pi\sigma_1\sigma_2\sqrt{1-\rho^2}} e^{-\frac{1}{2(1-\rho^2)}\left((\frac{x_1-\mu_1}{\sigma_1})^2 - \frac{2\rho(x_1-\mu_1)(x_2-\mu_2)}{\sigma_1\sigma_2}) + (\frac{x_2-\mu_2}{\sigma_2})^2\right)} \tag{B.66}$$

Consider the exponential term, the form can be simplified using change of variables. Let

doi:10.6342/NTU202400740

$\frac{x_1-\mu_1}{\sigma_1}=x_1'$ and $\frac{x_2-\mu_2}{\sigma_2}=x_2'$, then

$$
\begin{aligned}
&-\frac{1}{2(1-\rho^2)}\big((\frac{x_1-\mu_1}{\sigma_1})^2-\frac{2\rho(x_1-\mu_1)(x_2-\mu_2)}{\sigma_1\sigma_2})+(\frac{x_2-\mu_2}{\sigma_2})^2\big)\\
&=-\frac{1}{2(1-\rho^2)}\big(x_1'^2-2\rho x_1'x_2'+x_2'^2\big)\\
&=-\frac{1}{2(1-\rho^2)}(x_1'^2-\rho^2x_1'^2+\rho^2x_1'^2-2\rho x_1'x_2'+x_2'^2)\\
&=-\frac{1}{2(1-\rho^2)}\big(x_1'^2(1-\rho^2)+(x_2'-\rho x_1')^2\big) \qquad \text{(B.67)}
\end{aligned}
$$

Thus, Eq. (B.66) becomes

$$
\frac{1}{2\pi\sigma_1\sigma_2\sqrt{1-\rho^2}}\exp\big(-\frac{x_1'^2(1-\rho^2)}{2(1-\rho^2)}\big)\exp\bigg(-\frac{1}{2(1-\rho^2)}\big(x_2'-\rho x_1'\big)^2\bigg) \qquad \text{(B.68)}
$$

Therefore,

$$
\begin{aligned}
LSF(x_1)&=\int_{-\infty}^{\infty}f_{X_1X_2}(x_1,x_2)\mathrm{d}x_2\\
&=\int_{-\infty}^{\infty}\frac{\exp\big(-\frac{x_1'^2(1-\rho^2)}{2(1-\rho^2)}\big)}{2\pi\sigma_1\sigma_2\sqrt{1-\rho^2}}\exp\bigg(-\frac{1}{2(1-\rho^2)}\big(x_2'-\rho x_1'\big)^2\bigg)\mathrm{d}x_2\\
&=\frac{\exp\big(-\frac{x_1'^2}{2}\big)}{2\pi\sigma_1\sigma_2\sqrt{1-\rho^2}}\int_{-\infty}^{\infty}\exp\bigg(-\frac{1}{2(1-\rho^2)}\big(\frac{x_2-\mu_2}{\sigma_2}-\rho\frac{x_1-\mu_1}{\sigma_1}\big)^2\bigg)\mathrm{d}x_2\\
&=\frac{\exp\big(-x_1'^2/2\big)}{2\pi\sigma_1\sigma_2\sqrt{1-\rho^2}}\int_{-\infty}^{\infty}\exp\bigg(-\frac{1}{2}\big(\frac{\frac{x_2-\mu_2}{\sigma_2}-\rho\frac{x_1-\mu_1}{\sigma_1}}{\sqrt{1-\rho^2}}\big)^2\bigg)\mathrm{d}x_2 \qquad \text{(B.69)}
\end{aligned}
$$

doi:10.6342/NTU202400740

Let $x_2'' = \dfrac{\dfrac{x_2-\mu_2}{\sigma_2} - \rho\dfrac{x_1-\mu_1}{\sigma_1}}{\sqrt{1-\rho^2}}$, then

$$\frac{\mathrm{d}x_2''}{\mathrm{d}x_2} = \frac{1}{\sigma_2\sqrt{1-\rho^2}}$$

$$\therefore \mathrm{d}x_2'' = \frac{1}{\sigma_2\sqrt{1-\rho^2}}\mathrm{d}x_2$$

$$\begin{aligned}\therefore LSF(x_1) &= \frac{\exp\big(-x_1'^2/2\big)}{2\pi\sigma_1\sigma_2\sqrt{1-\rho^2}}\int_{-\infty}^{\infty}\exp\bigg(-\frac{1}{2}x_2''^2\bigg)\mathrm{d}x_2 \\ &= \frac{\exp\big(-x_1'^2/2\big)}{2\pi\sigma_1\sigma_2\sqrt{1-\rho^2}}\int_{-\infty}^{\infty}\exp\bigg(-\frac{1}{2}x_2''^2\bigg)\sigma_2\sqrt{1-\rho^2}\mathrm{d}x_2'' \\ &= \frac{\exp\big(-x_1'^2/2\big)}{2\pi\sigma_1}\int_{-\infty}^{\infty}\exp\big(-x_2''^2/2\big)\mathrm{d}x_2'' \end{aligned} \tag{B.70}$$

Using the result of Guassian integral, $\int_{-\infty}^{\infty} e^{-x^2/2}\mathrm{d}x = \sqrt{2\pi}$, then the line spread function becomes

$$\begin{aligned} LSF(x_1) &= \frac{\exp\left(-x_1'^2/2\right)}{2\pi\sigma_1}\sqrt{2\pi} \\ &= \frac{\exp\big(-\frac{1}{2}(\frac{x_1-\mu_1}{\sigma_1})^2\big)}{\sqrt{2\pi}\sigma_1} \\ &= \frac{1}{\sqrt{2\pi}\sigma_1}\exp\big(-\frac{(x_1-\mu_1)^2}{2\sigma_1^2}\big) \\ &\sim \mathcal{N}(\mu_1,\sigma_1) \end{aligned}$$ □

This implies that the LSF, which is a 1D Gaussian distribution, has the same standard deviation as its underlying PSF.

Notice, Eq. (B.64) in proposition 1 concluded that lateral spot size can be written as

$$2\sqrt{2\ln 2}\sigma_x \tag{B.71}$$

where σ_x is the x-directional standard deviation of the light spot, which is fitted by a

doi:10.6342/NTU202400740

bivariate Gaussian distribution. By applying proposition 2, the lateral spot size is identical to the FWHM of the Gaussian-fitted cross-sectional profile

$$2\sqrt{2\ln 2}\sigma_x = 2\sqrt{2\ln 2}\sigma \tag{B.72}$$

where σ is the standard deviation of the cross-sectional intensity. Hence, the formula

$$\text{FWHM} = 2\sqrt{2\ln 2}\sigma = |u(t_1) - u(t_2)| \tag{B.73}$$

where $u(t_1)$ and $u(t_2)$ are the extreme points of the de La Hire's ellipse as described in Appendix A.

Proposition 2 demonstrated that Gaussian-distributed light spot has some good properties. The light spot has the same standard deviation on x-axis as the line pattern does. This invariant can be useful since by calculating the standard deviation of cross-sectional intensity, the lateral spot size can be obtained.

In practical scenarios, this proposition may face challenges when dealing with irregular local surface, where the light spot spans multiple curvatures simultaneously. It's essential to note that the assumption here is that the local surface, covered by the light spot, maintains a uniform tilting angle.

doi:10.6342/NTU202400740